FINITE ELEMENT STRESS ANALYSIS OF IDEALIZED COMPOSITE DAMAGE ZONES

by

David A. O'Brien

Thesis submitted to the Graduate Faculty of the

Virginia Polytechnic Institute and State University

in partial fulfillment of the requirements for the degree of

MASTER OF SCIENCE

in

Engineering Mechanics

APPROVED:

C. T. Herakovich, Chairman

J. W. Deaton

E. G. Henneke, II

M. P. Kamat

December, 1977

Blacksburg, Virginia

ACKNOWLEDGMENTS

This document represents work accomplished under NASA Grant NGR-47-004-129 during the period September, 1976 through December, 1977. Mr. Jerry Deaton was the grant technical monitor and his interest and support is appreciated. Thanks are due to Professor C. T. Herakovich, Committee Chairman, for his long hours of patient assistance. Thanks are also in order to Professors M. P. Kamat and E. G. Henneke, II and Messrs. E. A. Humphreys, G. L. Farley and H. W. Bergner for their aid and to Ms. Frances Carter for typing the manuscript.

TABLE OF CONTENTS

LIST OF FIGURES

LIST OF TABLES

Chapter 1

INTRODUCTION

The expanding use of laminated fibrous composites in such structures as aircraft ailerons and turbine blades has prompted many studies into impact damage. The American Society for Testing and Materials has held a symposium on Foreign Object Damage (FOD) and a recent survey at the NASA/Langley Technical Library lists 272 separate articles on impact in composites. Thus, impact damage has become a major concern to the design engineer.

The major emphasis, though, has been on failure mechanisms, impact response and residual strength. Further, most studies have been concerned with damaged composites where the damage extends through the total thickness, such as holes. Little attention has been given to surface damage which "peels" off only a layer or two of the laminated composite. Further, few studies have been made into the stress distribution around the damaged region or the effect of the free edge at the damaged region on the three-dimensional stress distribution.

This study examines an idealized damaged region: a centered rectangular groove or cutout, extending one or two layers in depth and running the entire length of a long thin symmetric composite laminate. For symmetry reasons, the cutout is on both the top and bottom surfaces (see Fig. 1). This idealized damaged region, which simulates several layers "peeled" off, was chosen as a tractable problem providing insight into the more general problem of the stress distribution near an irregularly shaped damage zone.

The idealized damage zone is studied by the finite element method. The finite element programs NONCOM, developed by Renieri and Herakovich [1], and Herakovich, Renieri and Brinson [2], and a modified version, NONCOM1, developed by Humphreys and Herakovich [3], are both a quasi-three dimensional analysis. Hygrothermal and nonlinear capabilities are included in the programs, though this study will not examine hygrothermal effects. Some modifications have been made to NONCOM1 to improve efficiency and running time and the modified version is called NONCOM2. In addition, a Tsai-Wu failure criteria has been included and used to predict failure.

Due to the increased concern over the compressive behavior of laminated composites, all loadings are compressive. A number of laminates are studied, with and without cutouts, including cross-ply, angle-ply, and quasi-isotropic laminates. The material system examined is Thornel 300/Narmco 5208 graphite-epoxy for which a large body of data exists in the literature.

Chapter 2

LITERATURE REVIEW

Idealized damage zones have a long history of investigation. Timoshenko and Woinowsky-Krieger [4] developed analytic expressions for the stress distribution near a circular hole in a uniformly loaded infinite plate. Timoshenko and Goodier [5] extended the analysis to plates with elliptical holes and fillets. Both references used a plane strain, linear elastic, isotropic approach and neglected σ_z, τ_{yz} and τ_{xz} stresses. Both presented stress concentration values for the cases examined.

Roark and Young [6], as well as Peterson [7], give stress concentration factors for various material discontinuities such as holes, grooves and notches. The stress concentration factors are merely compiled in references [6] and [7], having been experimentally determined by other authors. The data presented were for linear elastic, isotropic materials only. None of the discontinuities presented had the same configuration as the cutout examined in this study.

Theoretical stress distributions around holes in anisotropic plates have been given by Savin [8]. Circular, elliptical and filleted rectangular holes are studied using a complex mapping approach. Again, a plane strain, linear elastic approach is utilized and σ_z, τ_{yz} and τ_{xz} stresses are neglected.

Experimental studies into the stress state near cutouts in composite plates have been conducted by Rowlands, Daniel and Whiteside [9]. Cir-

cular, elliptical and square cutouts in boron epoxy composite plates were investigated. Two laminate configurations and a number of hole diameter-to-width ratios and hole diameter-to-thickness ratios were studied. Another study by Ashton, Burdorf and Olson [10] gave experimentally determined stress concentration values for cutouts in graphite-epoxy coupons. Both of these studies were concerned with the hole's effect on the strength of the laminate and neither investigated interlaminar stresses around the hole.

A three dimensional finite element program developed by Barker, Dana and Pryor [11] was used to analyze cutouts in finite width laminates subjected to uniform axial strain. Interlaminar stresses (σ_z, τ_{yz} and τ_{xz}) near the cutouts were investigated and stress concentration values for circular, square and diamond-shaped holes were given. Nonlinear effects were not considered, nor was failure of the laminate studied.

The idealized damage zone examined in this study has apparently not been investigated before. A major reason for this may be the lack of analytic tools to handle this problem. The development of the finite element program NONCOM in references [1,2] has provided the necessary analytical tools for such an analysis.

Chapter 3

THEORETICAL BACKGROUND

The problem under consideration is the stress analysis of a long, finite width, symmetric composite laminate with a centered strip removed along the entire length of the laminate (Fig. 1). The laminates may be subjected to uniform thermal, moisture, and axial mechanical loading and all stresses and strains are assumed to be independent of the axial (x) coordinate. The resulting differential equations were presented by Hsu and Herakovich [12] while the theory behind the finite element program NONCOM2, which obtains a solution to the problem defined by those differential equations, was presented in references [1,2]. This report will present only the main points of the theoretical development.

3.1 Problem Formulation

The laminate consists of layers of an orthotropic material whose principal material axis makes an arbitrary angle θ with the x axis (Fig. 1). The constitutive equation (in condensed notation) can be written as

$$\{\sigma\}^k = [\bar{C}]^k(\{\varepsilon^*\}^k - \{\alpha\}^k \Delta T - \{\beta\}^k \Delta M) \qquad (3.1)$$

where:

$[\bar{C}]^k$ is the transformed 6x6 stiffness matrix

$\{\sigma\}^k$ is a 6x1 stress vector

$\{\varepsilon^*\}^k$ is a 6x1 total strain vector

$\{\alpha\}^k$ is a 6x1 vector of thermal coefficients

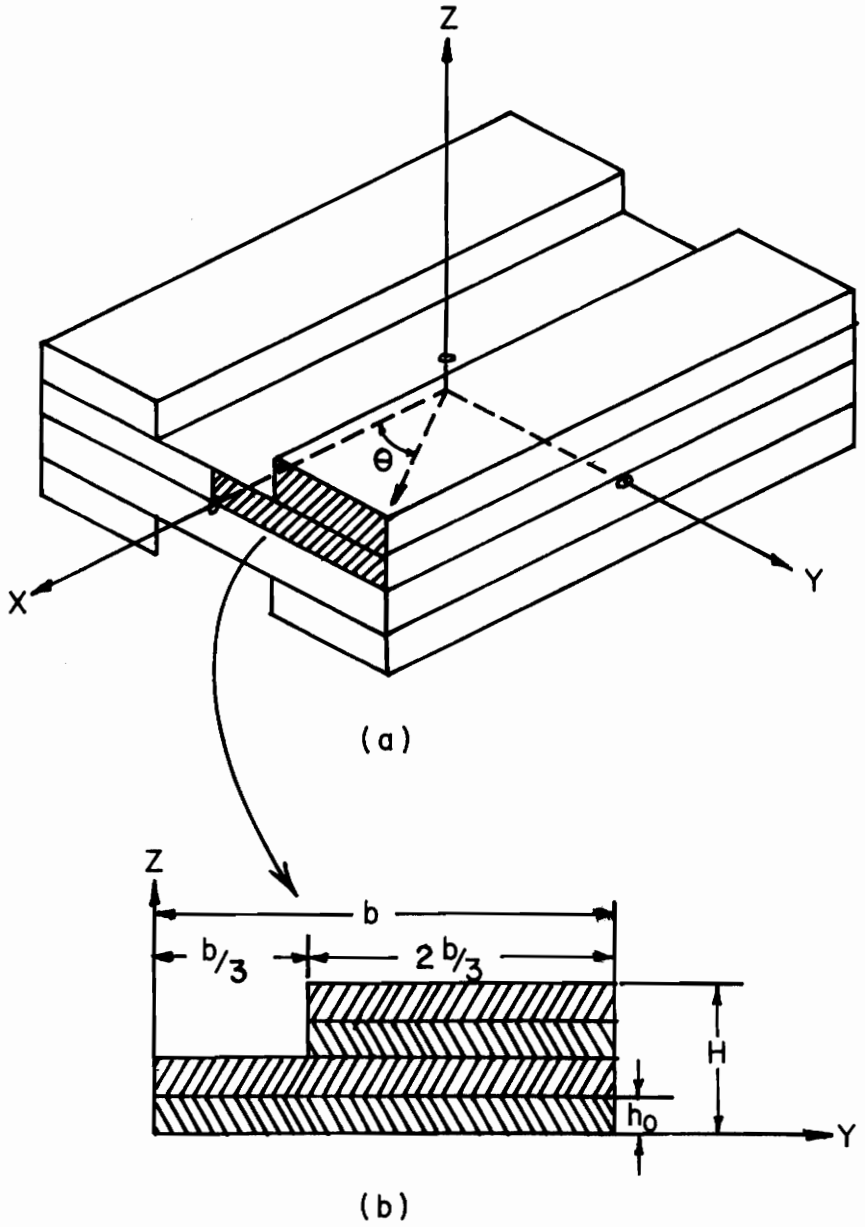

Figure 1. Geometry of Laminate with Idealized Damage Zone

$\{\beta\}^k$ is a 6x1 vector of moisture coefficients

ΔT is temperature change (from stress-free temperature)

ΔM is moisture concentration change (from 0%)

and k refers to the kth layer. Explicit expressions for these quantities can be found in Appendix A.

Noting that strains (and stresses) are functions of y and z only, it can be shown that suitable integration of the strain-displacement relations

$$\varepsilon_x = u_{,x}; \quad \varepsilon_y = v_{,y}; \quad \varepsilon_z = w_{,z} \tag{3.2}$$

$$\gamma_{yz} = v_{,z} + w_{,y}; \quad \gamma_{xz} = u_{,z} + w_{,x}; \quad \gamma_{xy} = u_{,y} + v_{,x}$$

yields the following displacement field

$$\begin{aligned} u &= (C_1 y + C_2 z + C_3)x + U(y,z) \\ v &= (C_4 z + C_5)x - C_1 \frac{x^2}{2} + V(y,z) \\ w &= -C_4 xy + C_6 x - C_2 \frac{x^2}{2} + W(y,z) \end{aligned} \tag{3.3}$$

The imposition of the proper symmetry conditions for axial loading

$$\begin{aligned} u(x,y,z) &= u(x,y,-z) \\ v(x,y,z) &= v(x,y,-z) \\ w(x,y,z) &= -w(x,y,-z) \\ v(x,y,z) &= -v(x,-y,z) \\ w(x,y,z) &= w(x,-y,z) \end{aligned} \tag{3.4a}$$

as well as the experimentally determined condition (Pipes and Daniels [13])

$$u(0,y,z) = -u(0,-y,z) \tag{3.4b}$$

results in the following displacement field:

$$\begin{aligned} u &= \varepsilon_x x + U(y,z) \\ v &= V(y,z) \\ w &= W(y,z) \end{aligned} \tag{3.5}$$

where $C_3 = u,_x = \varepsilon_x$, the uniform axial strain. In addition, the displacement boundary conditions on the midplane and centerline are

$$\begin{aligned} U,_z(y,0) &= 0 \qquad U(0,z) = 0 \\ V,_z(y,0) &= 0 \qquad V(0,z) = 0 \\ W(y,0) &= 0 \qquad W,_y(0,z) = 0 \end{aligned} \tag{3.6}$$

This displacement field and the boundary conditions were first presented by Pipes and Pagano [14].

For completeness, the simplified equilibrium equations, with stresses independent of x and neglecting body forces, are shown below.

$$\begin{aligned} \frac{\partial \tau_{xy}}{\partial y} + \frac{\partial \tau_{xz}}{\partial z} &= 0 \\ \frac{\partial \sigma_y}{\partial y} + \frac{\partial \tau_{yz}}{\partial z} &= 0 \\ \frac{\partial \tau_{yz}}{\partial y} + \frac{\partial \sigma_z}{\partial z} &= 0 \end{aligned} \tag{3.7}$$

In addition, the full governing differential equations for the kth layer, as developed in reference [12], are presented below.

$$\{C_{66}U_{,yy} + C_{55}U_{,zz} + C_{26}V_{,yy} + C_{45}V_{,zz} + (C_{36} + C_{45})W_{,yz}\}^k = 0$$

$$\{C_{26}U_{,yy} + C_{45}U_{,zz} + C_{22}V_{,yy} + C_{44}V_{,zz} + (C_{23} + C_{44})W_{,yz}\}^k = 0 \quad (3.8)$$

$$\{(C_{45} + C_{36})U_{,yz} + (C_{44} + C_{23})V_{,yz} + C_{44}W_{,yy} + C_{33}W_{,zz}\}^k = 0$$

3.2 Finite Element Formulation

As in the previous section, only the main points of the formulation will be presented here. A complete presentation can be found in references [1,2].

The finite element solution involves the subdivision (or discretization) of the structure into a finite number of elements (Fig. 2). For each element, a set of interpolation polynomials is chosen to represent the displacement field within that element as functions of the element's nodal displacements. Using the strain-displacement relations (3.2) and the constitutive relationship (3.1), the stresses and strains in each element can be found as functions of the nodal displacements. Applying a variational principle, such as minimum potential energy, a set of equations relating nodal displacements to nodal forces can be obtained for each element in the form

$$[K]^{(\ell)}\{u\}^{(\ell)} = \{F\}^{(\ell)} \quad (3.9)$$

where

$[K]^{(\ell)}$ is the elemental stiffness matrix

$\{u\}^{(\ell)}$ are the elemental nodal displacements

$\{F\}^{(\ell)}$ are the elemental nodal forces

These elemental relationships are then assembled into a global set

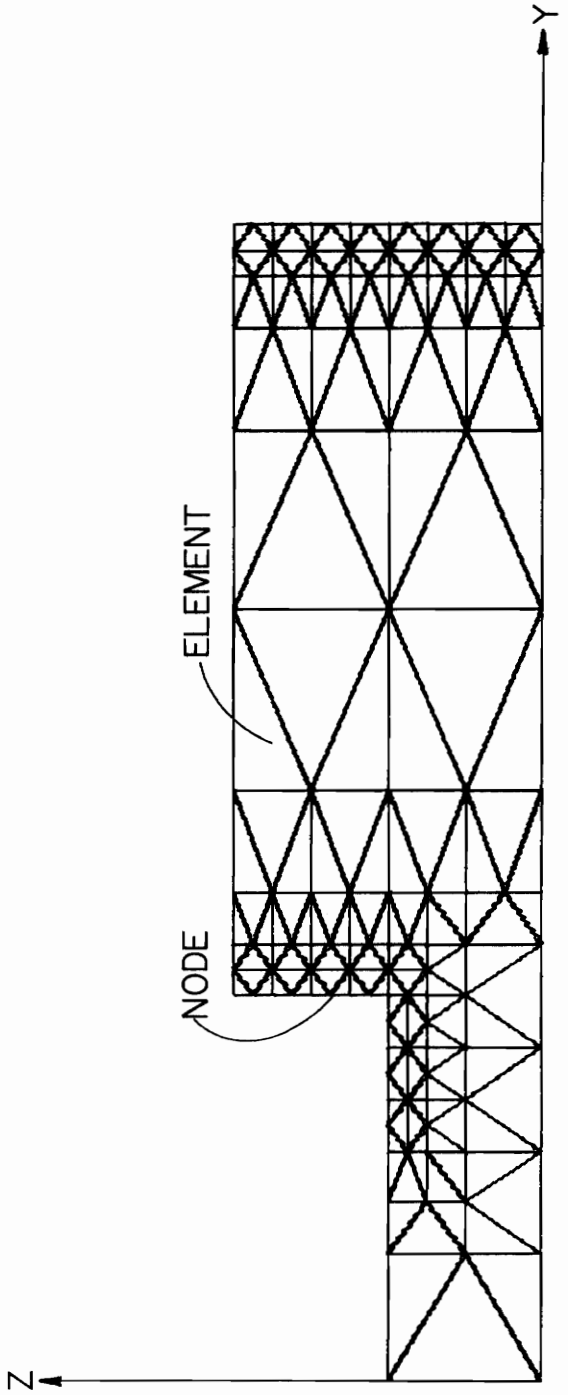

Figure 2. Discretization of Quarter Cross-Section of Damaged Four Layer Symmetric Laminate.

of equations relating all nodal displacements to all nodal forces. The application of boundary conditions and solution of these equations gives the displacements and thus the stresses and strains over the entire structure.

Constant strain, constant stress triangular elements are utilized by NONCOM2. The interpolation polynomials have the form

$$\begin{aligned} u &= a_1 + a_2 y + a_3 z + \xi_x x \\ v &= a_4 + a_5 y + a_6 z \\ w &= a_7 + a_8 y + a_9 z \end{aligned} \tag{3.10}$$

When substituted into the strain-displacement relations (3.2), these interpolation polynomials yield constant strains over each element. The uniform normal strain is ξ_x and the constants a_1 through a_9 are functions of the element's nodal displacements and nodal spatial coordinates.

Substitution of (3.10) into (3.2) yields the following strain-displacement relationship

$$\begin{Bmatrix} \varepsilon_x \\ \varepsilon_y \\ \varepsilon_z \\ \gamma_{yz} \\ \gamma_{xz} \\ \gamma_{xy} \end{Bmatrix} = \frac{1}{A} \begin{Bmatrix} \xi_x A \\ af_1+cv_2+ev_3 \\ bw_1+dw_2+gw_3 \\ bv_1+dv_2+gv_3+aw_1+cw_2+ew_3 \\ bu_1+du_2+gu_3 \\ au_1+cu_1+eu_1 \end{Bmatrix} \tag{3.11}$$

where

A = area of element

u_1, u_2, u_3 = x-displacement at nodes 1,2,3 respectively

v_1, v_2, v_3 = y-displacement at nodes 1,2,3 respectively

w_1, w_2, w_3 = z-displacement at nodes 1,2,3 respectively

and a,b,c,d,e,g are known constants involving nodal spatial coordinates.

For the case of uniform thermal load the strains are

$$\{\varepsilon\} = \{\varepsilon^*\} - \{\alpha\}\Delta T \tag{3.12}$$

where $\{\varepsilon\}$ is the mechanical strain vector and $\{\varepsilon^*\}$, $\{\alpha\}$, and ΔT are as defined in (3.1).

Noting equ's. (3.11), the mechanical strains can be written as

$$\begin{Bmatrix} \varepsilon_x \\ \varepsilon_y \\ \varepsilon_z \\ \gamma_{yz} \\ \gamma_{xz} \\ \gamma_{xy} \end{Bmatrix} = \begin{Bmatrix} \xi_x - \alpha_x \Delta T \\ (av_1 + cv_2 + ev_3)/A - \alpha_y \Delta T \\ (bw_1 + dw_2 + gw_3)/A - \alpha_z \Delta T \\ (bv_1 + dv_2 + gv_3 + aw_1 + cw_2 + ew_3)/A \\ (bu_1 + du_2 + gu_3)/A \\ (au_1 + cu_2 + eu_3)/A - \alpha_{xy} \Delta T \end{Bmatrix} \tag{3.13}$$

The formulation for hygroscopic loading is analogous to that for thermal loading, except β's replace α's and ΔM replaces ΔT.

The principle of minimum potential energy states that the body is in equilibrium when the total potential energy ψ is minimum where

$$\psi = U_e + W_e, \tag{3.14}$$

U_e = internal strain energy

and

W_e = potential energy of the applied loads.

The internal strain energy for an element is

$$U_e = \frac{1}{2}\int \{\varepsilon\}^T[\bar{C}]\{\varepsilon\}dVol \tag{3.15}$$

where $[\bar{C}]$ is as defined in (3.1) and $\{\varepsilon\}$ is as defined in (3.11) or (3.13), depending on whether it is mechanical or thermal (hygroscopic) loading, respectively. For a unit thickness element with constant strains, U_e reduces to

$$U_e = \frac{A}{2}\{\varepsilon\}^T[\bar{C}]\{\varepsilon\} \tag{3.16}$$

and W_e becomes

$$W_e = -\{F\}^{T(\ell)}\{u\}^{(\ell)} \tag{3.17}$$

where $\{F\}^{(\ell)}$ and $\{u\}^{(\ell)}$ are as defined in (3.9).

Minimization of equ. (3.14) with respect to nodal displacements yields the elemental stiffness matrix plus strain, thermal and hygroscopic related vectors. Exact forms for these can be found in reference [3]. The finite element meshes used for this report were generated by a program developed by Bergner, Davis and Herakovich [15] and can be found in Appendix B.

3.3 Failure Analysis

3.3.1 Tsai-Wu Failure Criterion

The three dimensional stresses from NONCOM2 provide a unique opportunity to study a three dimensional failure criterion. Tsai and Wu [16] proposed such a criterion, postulating a failure surface of the form

$$F_i\sigma_i + F_{ij}\sigma_i\sigma_j = 1 \tag{3.18}$$

where the contracted notation is used and i,j=1,2,...6. The strength tensors, F_i and F_{ij}, are of the second and fourth rank, respectively, and F_{ij} is assumed to be symmetric.

To determine F_i and F_{ij} in terms of uniaxial strengths, a series of "thought" experiments are conducted. Assuming only a longitudinal stress on a unidirectional laminate, the tensile (X_t) and compressive (X_c) strengths are substituted into equ. (3.18), resulting in the following

$$\begin{aligned} F_1X_t + F_{11}X_t^2 &= 1 \\ F_1X_c + F_{11}X_c^2 &= 1 \end{aligned} \tag{3.19}$$

Solving these two simultaneous equations F_1 and F_{11} are found to be

$$\begin{aligned} F_1 &= \frac{1}{X_t} + \frac{1}{X_c} \\ F_{11} &= \frac{-1}{X_tX_c} \end{aligned} \tag{3.20}$$

In a similar fashion, the following are found

$$F_2 = \frac{1}{Y_t} + \frac{1}{Y_c}$$

$$F_{22} = \frac{-1}{Y_tY_c}$$

(3.21)

$$F_3 = \frac{1}{Z_t} + \frac{1}{Z_c}$$

$$F_{33} = \frac{-1}{Z_t Z_c}$$

For the shear terms, it is noted that shear strengths are independent of direction (and thus of sign) in orthotropic materials. Thus all terms involving shear to the first power are dropped. The only non-zero terms involving shear are then F_{44}, F_{55}, and F_{66}. With thought experiments similar to those used previously, the non-zero shear terms are found to be

$$F_{44} = \frac{1}{(S_{23})^2}$$

$$F_{55} = \frac{1}{(S_{13})^2} \qquad (3.22)$$

$$F_{66} = \frac{1}{(S_{12})^2}$$

where S_{ij} refers to the shear strength in the i-j plane.

The only terms left to be determined are F_{12}, F_{13} and F_{23}. However, no simple uniaxial test will determine these interaction terms. They must be experimentally found by some biaxial test of strength. Wu [17] describes how to obtain optimum ratios of biaxial stress. Pipes and Cole [18] found, however, that variations of 400 percent in the value of the interaction term results in very little difference in the strength envelope.

For an orthotropic material, then, the Tsai-Wu criterion takes the

form:

$$F_1\sigma_1 + F_2\sigma_2 + F_3\sigma_3 + F_{11}\sigma_1^2 + F_{22}\sigma_2^2 + F_{33}\sigma_3^2 + F_{44}\tau_{23}^2 + F_{55}\tau_{13}^2 + F_{66}\tau_{12}^2 + 2F_{12}\sigma_1\sigma_2 + 2F_{13}\sigma_1\sigma_3 + 2F_{23}\sigma_2\sigma_3 = 1 \quad (3.23)$$

Since the Tsai-Wu criterion has a tensorial form, it is valid in all coordinate systems and the transformation has a simple tensorial form. For a θ rotation about the 3 (z) axis, the Tsai-Wu criterion takes the form:

$$F'_1\sigma_x + F'_2\sigma_y + F'_3\sigma_z + F'_6\sigma_{xy} + F'_{11}\sigma_x^2 + F'_{22}\sigma_y^2 + F'_{33}\sigma_z^2 + F'_{44}\tau_{yz}^2 + F'_{55}\tau_{xz}^2 + F'_{66}\tau_{xy}^2 + 2F'_{16}\sigma_x\tau_{xy} + 2F'_{26}\sigma_y\tau_{xy} + 2F'_{36}\sigma_z\tau_{xy} + 2F'_{45}\tau_{yz}\tau_{xz} + 2F'_{12}\sigma_x\sigma_y + 2F'_{13}\sigma_x\sigma_y + 2F'_{23}\sigma_y\sigma_z = 1 \quad (3.24)$$

The exact form of the F' terms can be found in Appendix C.

3.3.2 Failure Model

Using the Tsai-Wu criterion, the stresses on an element are used as input into equ's. (3.24). If the function has a value greater than or equal to one, the element has failed. However, a failed element is difficult to handle in a finite element solution.

Sandhu [19] proposed that when failure occurs, the moduli of the

material should be set to large negative numbers. This essentially "unloads" the failed material. The major drawback with this procedure is the creation of negative diagonals in the global stiffness matrix, causing an unstable matrix. The method used in references [1-3] is to reduce the moduli by the percent of overstrain in the failed direction, a complicated procedure and one that still allows a failed element to carry load.

A simpler approach, and the one adopted in this study, is to reduce all the moduli in a failed element to some small value. In addition, the stresses on this element are set equal to zero. By reducing the moduli and setting the stresses equal to zero, the failed element carries no load and does not contribute to the overall stiffness of the laminate during subsequent loading. However, even this approach can cause an unstable stiffness matrix, as will be shown later (see Section 5.4.2).

Chapter 4

THE FINITE ELEMENT PROGRAM (NONCOM2)

The program NONCOM1, a modified version of NONCOM, was modified further for this study and called NONCOM2. Changes made for this version include a more efficient equation solver, a failure criterion based on the Tsai-Wu function (Chap. 3) and an improved handling of hygrothermal effects.

4.1 Equation Solver

The program NONCOM1 used an equation solver called SEESOL [20], which stored the stiffness matrix in blocks on tape. However, I/O charges on VPI&SU's IBM 370 make this an expensive method of solving simultaneous equations. Since the VPI&SU system has an extremely large core and can thus store large matrices, a more economical method is an in-core solution.

An equation solver, COLSOL, presented by Bathe and Wilson [21], is an entirely in-core solution. The upper triangular half of the symmetric stiffness matrix is stored, column by column, in a row vector, A. For a banded matrix, terms above the "top" of the bandwidth are zero. In order to minimize storage requirements, terms above the "top" of a column are not stored. This is an extremely efficient method of storage for symmetric, highly banded matrices similar to the type shown below.

$$[K] = \begin{bmatrix} A_1 & A_3 & A_6 & 0 & 0 & \cdots\cdots & 0 \\ & A_2 & A_5 & A_9 & 0 & \cdots\cdots & 0 \\ & & A_4 & A_8 & A_{12} & \cdots\cdots & 0 \\ & & & A_7 & A_{11} & \cdots\cdots & 0 \\ & & & & A_{10} & \cdots\cdots & 0 \\ & & & & & \ddots & 0 \\ & & & & & & A_n \\ & & & & & & A_{n-1} \\ & & & & & & A_{n-2} \\ & & & & & & A_{n-3} \end{bmatrix} \qquad (4.1)$$

After the global stiffness matrix is stored, Cholesky decomposition is used to solve the equations and provide the nodal displacements.

4.2 Material Considerations

The program NONCOM1 had several restrictions on the temperature and moisture dependence of material properties. Only elastic and shear moduli, and thermal and moisture coefficients were assumed temperature and moisture dependent; all other material properties were assumed constant. Also, it was assumed that tensile and compressive moduli varied in the same manner. The modified version, NONCOM2, used in this study allows all material properties to vary as functions of temperature and moisture. Further, tension and compression values are allowed to vary as independent functions.

Hygrothermal data is presently found in the literature in the form shown in Fig. 3. In the program, each of the curves is modeled as a series of linear segmented lines. Values of percent retention of a material property are found by linear interpolation between the end-points of the segments.

The material system used in this study was T300/5208 graphite-epoxy. Complete mechanical and thermal data were found in a report by Hofer, Larsen and Humphreys [22]. Hygroscopic data for this material can be found in reference [22] and a report by Kiebler [23], but the data are neither complete nor consistent. Since the loadings for this study were all mechanical only, the results were not affected by the incomplete hygroscopic data.

Material property values can be found in Appendix D. In addition, a user's guide for the input of hygrothermal properties into NONCOM2 can be found in Appendix E.

4.3 Nonlinear Analysis

The finite element analysis of Chapter 3 requires linear elastic properties. Since composites often have nonlinear mechanical properties, an incremental procedure is utilized to account for material nonlinearities within the framework of a linear elastic analysis.

4.3.1 Incremental Procedure

Using the incremental procedure, the mechanical properties are linearized for each increment and the load, either thermal, hygroscopic or uniform axial strain, is applied as a series of increments. Sum-

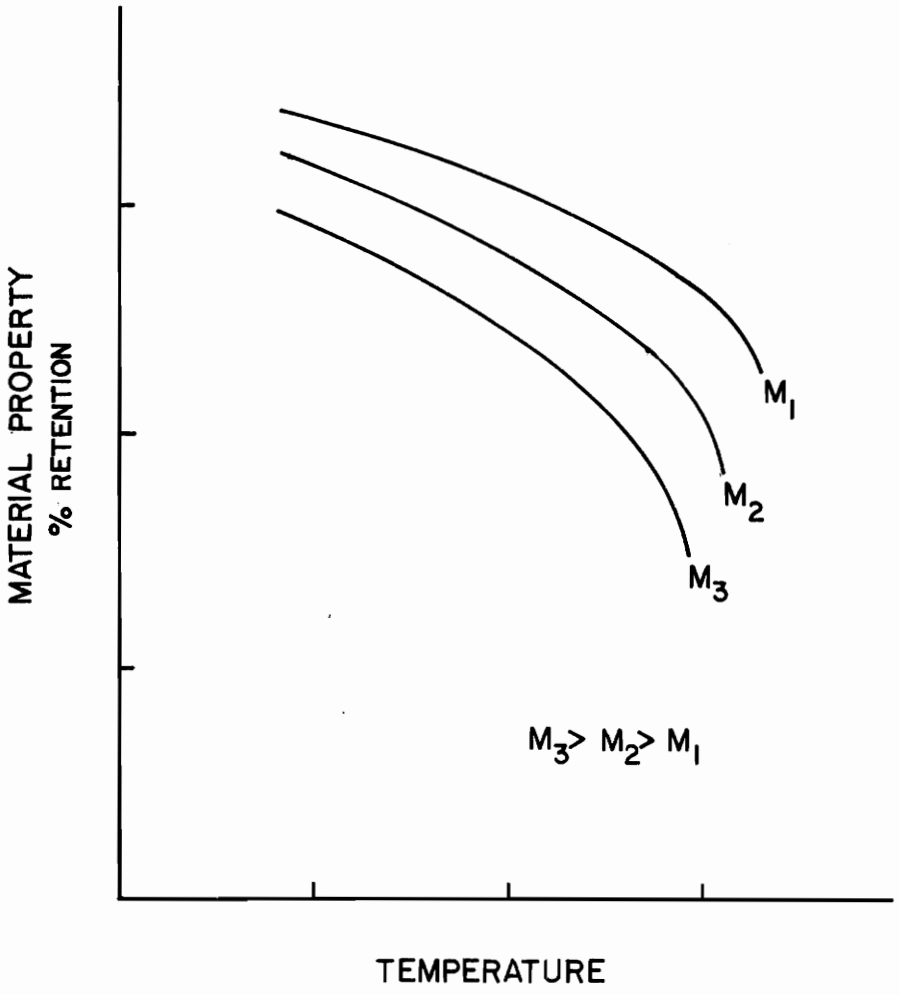

Figure 3. Typical Percent Retention Curves as a Function of Temperature and Moisture

mation of the linear solutions of stresses, strains and displacements for each increment yields the total solution. At each step of the procedure, the mechanical properties of each element are altered depending on the temperature, moisture and/or strain level. This procedure allows the properties of an element to vary independently of all other elements.

4.3.2 Determination of Tangent Modulus

Nonlinear stress-strain curves were represented by Ramberg-Osgood [24] approximations of the form

$$\varepsilon = \frac{\sigma}{E} + K_i \sigma^{n_i} \qquad i = 1 \text{ or } 2 \tag{4.2}$$

where E is the elastic modulus and K_i and n_i are Ramberg-Osgood coefficients. The procedure to calculate the four constants K_i and n_i can be found in reference [1]. The tangent modulus can be defined as

$$\bar{E} = \frac{d\sigma}{d\varepsilon} = \frac{E}{K_i E n_i \sigma^{n_i - 1} + 1} \qquad i = 1 \text{ or } 2 \tag{4.3}$$

Noting Fig. 4 the corresponding stress, σ^P, at the end of load increment P is

$$\sigma^P = \sum_{j=1}^{P} \Delta\varepsilon^j \bar{E}^j \tag{4.4}$$

where $\Delta\varepsilon^j$ is the increment of strain and $\bar{E}^j$ the tangent modulus during the jth load increment. For the P+1th increment, the tangent modulus becomes

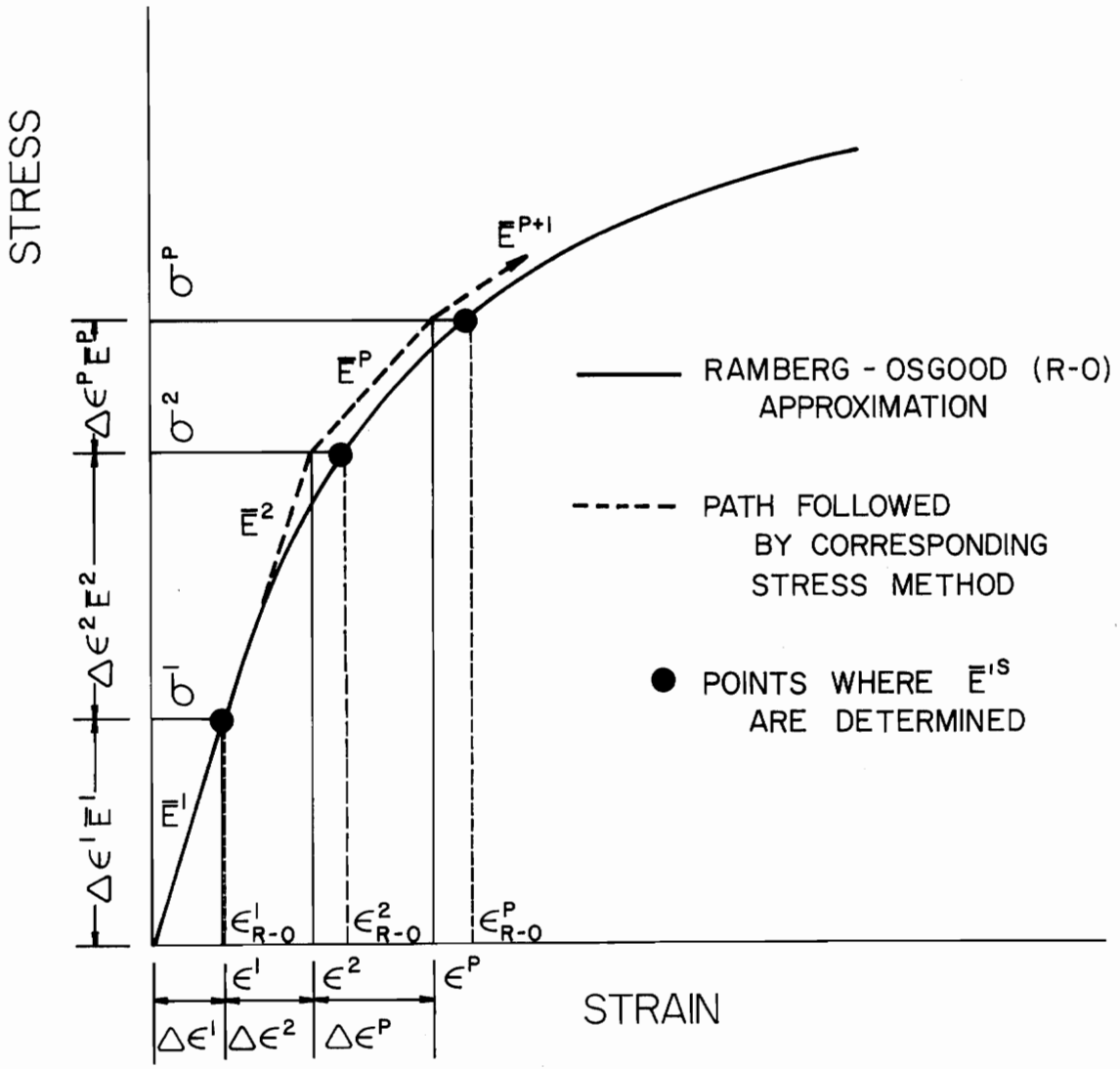

Figure 4. Determination of Tangent Modulus with Ramberg-Osgood Approximations

$$E^{P+1} = \frac{E}{K_i E n_i \left[\sum_{j=1}^{P} \Delta\varepsilon^j \bar{E}^j \right]^{n_i - 1} + 1} \qquad i = 1 \text{ or } 2 \qquad (4.5)$$

Using equation (4.5) and principal material strains, the tangent modulus for the next increment is calculated at the end of each increment. From Fig. 4, it can be seen that ε^P_{R-0}, the strain at which the tangent modulus, $\bar{E}^{P+1}$, is calculated, differs from the strain ε^P actually applied. This difference can be made arbitrarily small by choosing a sufficiently small increment. For the computer analysis, equations of the form (4.5) were used to determine the tangent moduli $\bar{E}_{11}$, $\bar{E}_{22}$, $\bar{E}_{33}$, $\bar{G}_{23}$, $\bar{G}_{13}$, and $\bar{G}_{12}$ for each finite element. It is assumed that shear response is independent of sign while extensional behavior can be different in tension and compression.

4.4 General Notes

In Appendix D, the values of the F_{12}, G_{13} and F_{23} Tsai-Wu interaction terms are given as $-0.58 \times 10^{-10}/(\text{PSI})^2$, a value taken from reference [18]. Wu [17] suggests a value of $2.0 \times 10^{-10}/(\text{PSI})^2$ as more appropriate for graphite-epoxy. Several computer runs showed, however, that the differences in the two values did not affect the overall trends. Since reference [17] was found after all the computer runs had been made the cases presented in Chapter 5 were not rerun with Wu's value.

The initial tangent modulus for all three versions of NONCOM is chosen as the tensile elastic modulus where, for compressive loading,

compressive moduli would be more appropriate. However, this factor did not significantly alter the overall results or conclusions.

Chapter 5

RESULTS AND DISCUSSION

The analysis presented in Chapters 3 and 4 was used to study various laminates of differing ply orientations. Four and eight layer laminates with or without cutouts were analyzed. Because of symmetry only a quarter of the laminate cross-section, shown in Fig. 1b, was examined. Both linear elastic and non-linear results are presented.

5.1 Averaging of Finite Element Results

The finite element analysis of Chapter 3 is based on a displacement formulation with linear interpolation functions over each element. This formulation results in stresses and strains which are constant over each element. Constant stresses for an individual element give a distribution of stresses which appear discontinuous over a series of elements. In order to produce smooth distributions, stresses are averaged over several elements.

Noting Fig. 5a, stresses for a through-the-thickness distribution are averaged along the line A-A. The stresses presented at point E correspond to an average of the stresses in elements 1 and 2. This method of averaging was used in all through-thickness plots.

For interfacial distributions, the σ_z, τ_{yz} and τ_{xz} stresses are averaged along the interface between the two layers, shown as line C-C in Fig. 5b. Since these three stress components must be continuous across the interface, the results are an average of elements above and below the interface. Thus, for point H the stresses are an average of

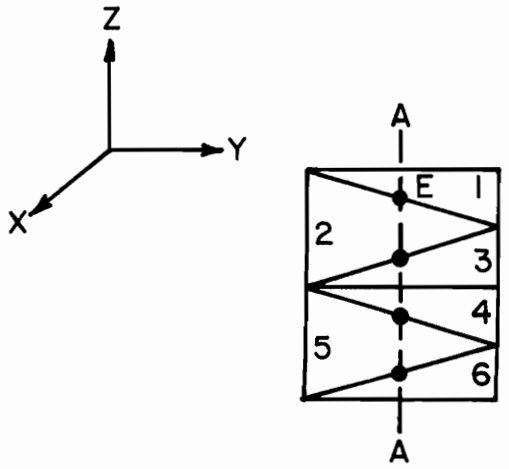

(a) THROUGH - THICKNESS

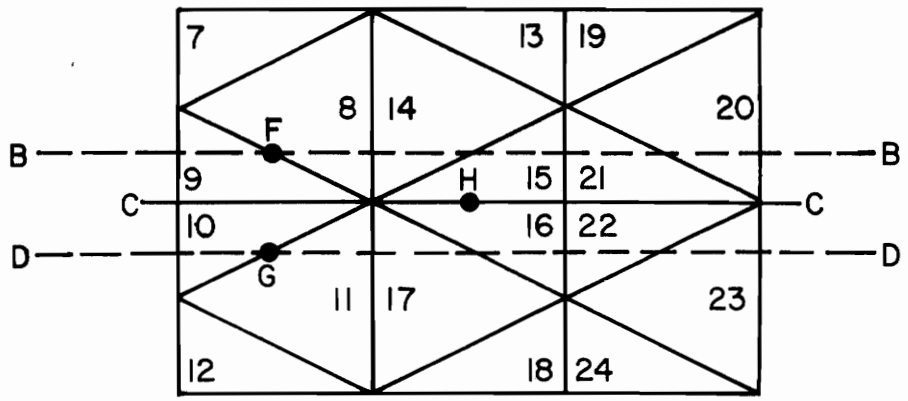

(b) INTERFACE

Figure 5. Averaging of Finite Element Results

elements 14, 15, 16 and 17. The stress components σ_x, σ_y and τ_{xy}, which are not necessarily continuous across an interface, are averaged along line B-B and line D-D. At point F, stresses are averaged over elements 8 and 9 while at point G stresses are averaged over elements 10 and 11.

5.2 Convergence of Finite Element Results

The finite element analysis, as mentioned previously, is based on a displacement formulation. However, the boundary conditions at the cutout and free edge are stress-free boundary conditions. Due to the approximation introduced by the displacement formulation, as well as the use of constant stress, constant strain elements, the stress-free boundary conditions will not, in general, be satisfied. However, Herakovich [25] has shown that the free edge conditions tend to be met as smaller and smaller elements are used near the free edge. Thus, convergence of the finite element solution at a particular point is a function of mesh size and displacement gradient.

Satisfaction of the equilibrium conditions for sections of the laminate (Fig. 6) is also a function of mesh size and displacement gradients. Similar to the stress boundary conditions at a point, equilibrium conditions for sections will tend to be met as the size of the elements is reduced. Equilibrium for the body as a whole, though, is automatically satisfied due to the formulation.

Thus, no finite element mesh based on a displacement formulation will satisfy stress boundary conditions or equilibrium conditions exactly. However, by using meshes with similar sized elements at cutout

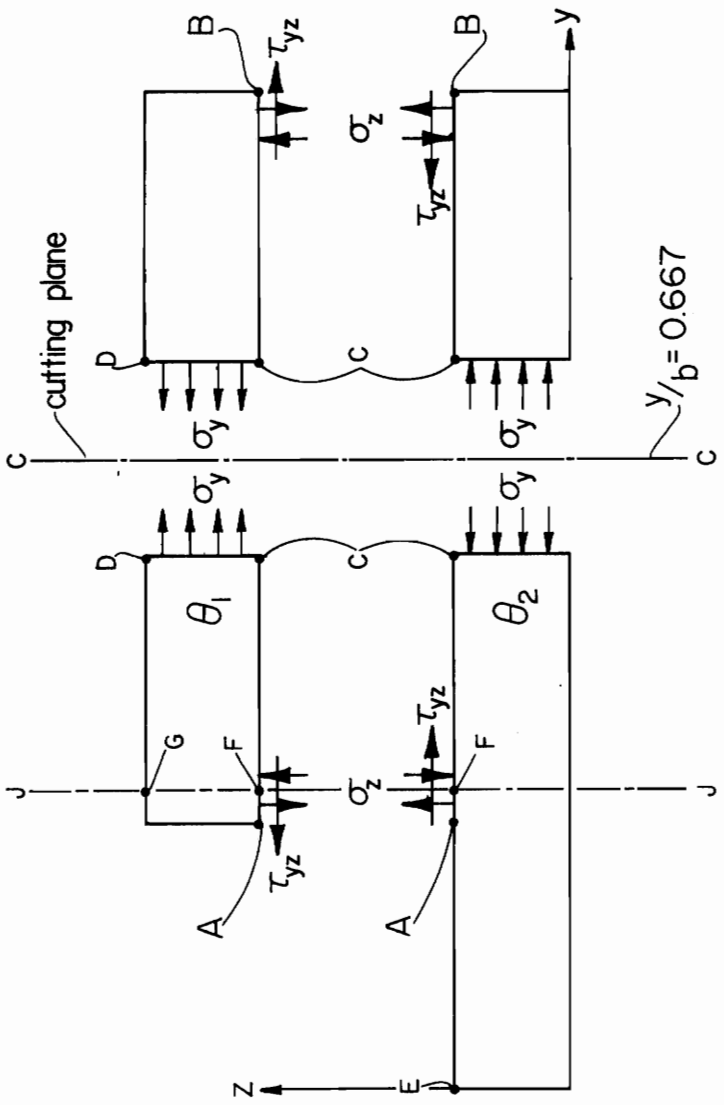

Figure 6. Partial Free Body Diagram of Quarter Cross-Section of Damaged Four Layer Symmetric Laminate

and free edges (areas of high displacement gradients) a sufficiently adequate stress distribution for relative comparisons and general conclusions is obtained.

5.3 Linear Elastic Results

This section contains linear elastic results for laminates with aspect ratios b/H = 68.2 (four layer laminate) and b/H = 34.1 (eight layer laminate) (Fig. 1) and applied uniform axial strain ε_x = -0.1 percent. The curves in this section were drawn by the VPI&SU CALCOMP plotter.

5.3.1 Unidirectional Laminates

The stress state in unidirectional laminates with all fibers oriented at an angle θ is a uniform uniaxial stress, σ_x, with or without a cutout. The value of σ_x is equal to the laminate value while the other stress components are approximately zero. Thus, for unidirectional laminates, the cutout does not alter the uniform stress state and produces no stress concentrations.

5.3.2 Four Layer Laminates

5.3.2.1 The $[0/90]_s$ Laminate

The σ_y stresses for the $[0/90]_s$ laminate with one layer removed as the idealized damage zone are shown in Fig. 7. These stresses are shown along the interface from the cutout edge (point A) to the free edge (point B). The σ_y stresses for the same layup with no layer removed are shown by the dashed lines. Near the free edge, the variation of σ_y, as

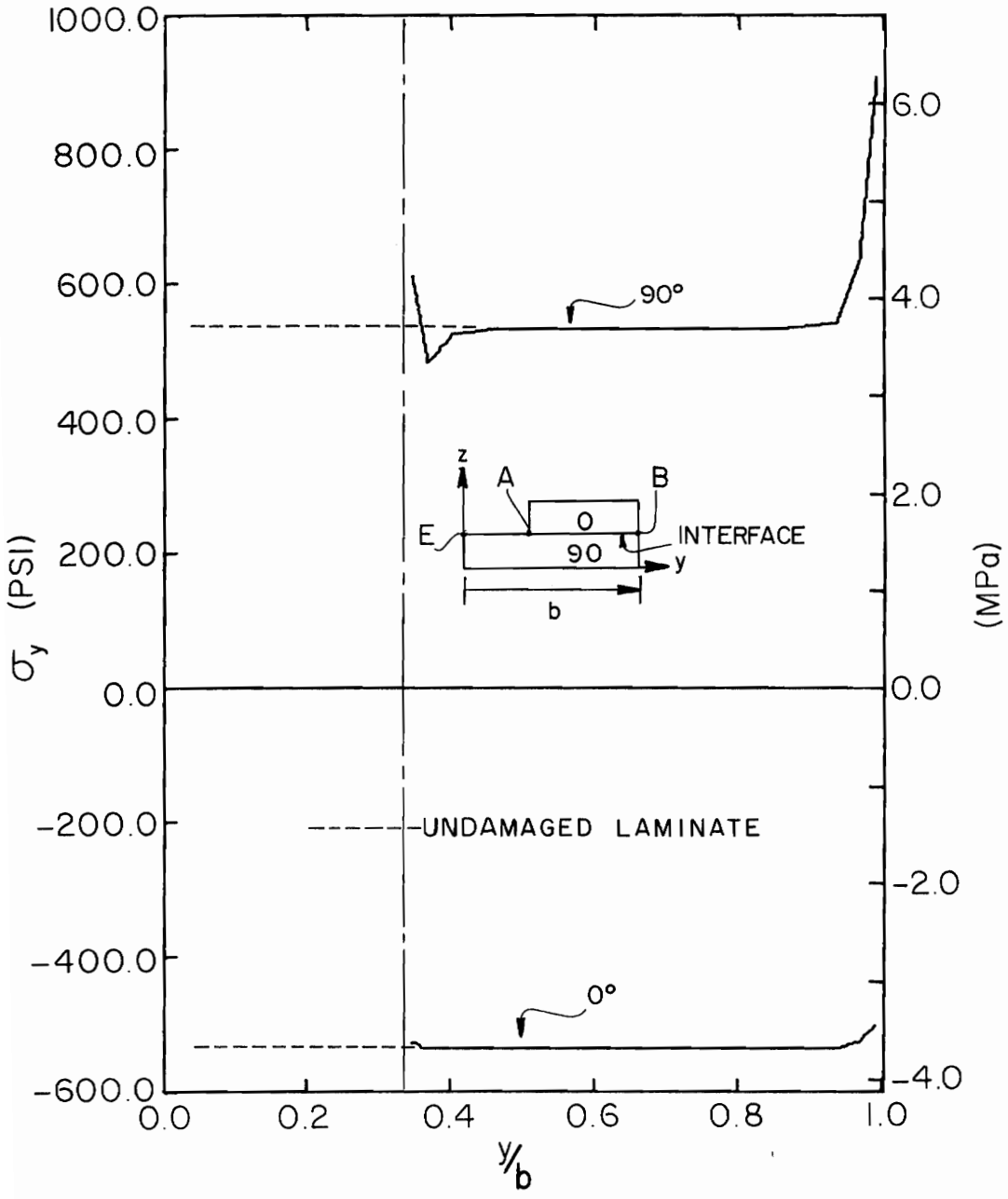

Figure 7. σ_y along Interface of $[0/90]_s$ Laminate (ε_x=-0.1%)

well as all other stress components, is exactly the same with or without a cutout. Also, because of the dimensions of the specimen, the σ_y (and σ_x and τ_{xy}) stresses in the interior region (away from the edges, between the cutout and free edges) are constant and equal to the theoretical laminate values for a $[0/90]_s$ laminate (Table 1).

The σ_z and τ_{yz} stresses, along the interface, shown in Fig. 8 and 9, respectively must satisfy several equlibrium conditions. The partial free-body diagram (Fig. 6) shows the 0° (θ_1=0°) layer of a [0/90] laminate with a section removed and a cutting plane, C-C, passing through the interior region. In order to satisfy force equilibrium, the following must be true.

$$\begin{aligned}
\int_A^B \sigma_z dy &= 0 \\
\int_A^B \tau_{yz} dy &= 0 \\
\int_A^C \sigma_z dy &= 0 \\
\int_A^C \tau_{yz} dy &= \sigma_y^L(h_o) \\
\int_C^B \sigma_z dy &= 0 \\
\int_C^B \tau_{yz} dy &= -\sigma_y^L(h_o)
\end{aligned} \tag{5.1}$$

TABLE 1

Comparison of Lamination Theory and Finite Element Results in Interior Regions (y/b=0.67) for $[\theta_1/\theta_2]_s$ Laminate

$[\theta_1/\theta_2]_s$		σ_x (psi)		σ_x (psi)		τ_{xy} (psi)	
		θ_1	θ_2	θ_1	θ_2	θ_1	θ_2
$[0/90]_s$	Lamination	-27790	-1552	-535	535	0	0
	NONCOM2	-27760	-1551	-535	535	0	0
$[\pm 45]_s$	Lamination	-3703	-3703	0	0	-1588	1588
	NONCOM2	-3703	-3703	0	0	-1588	1588

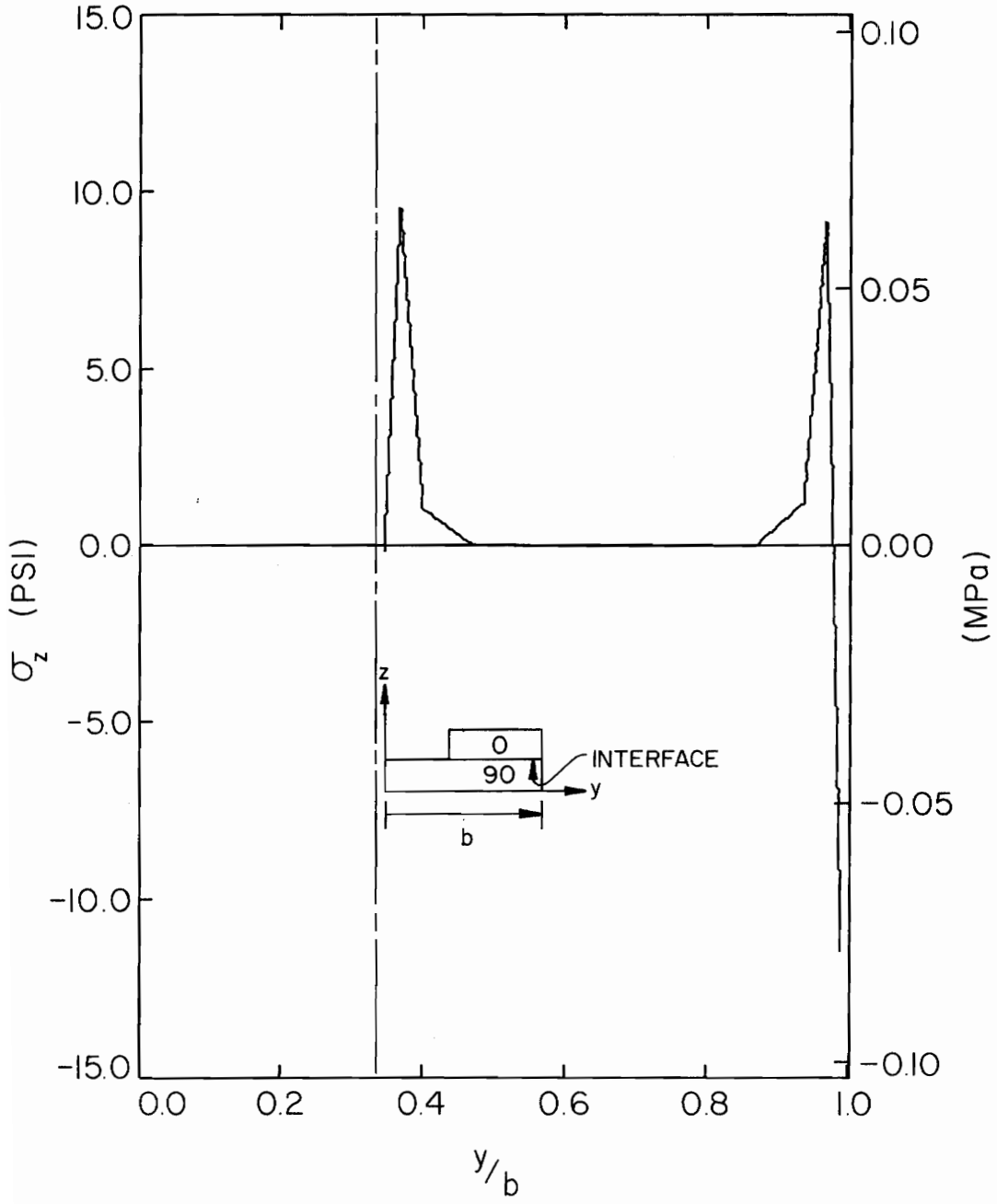

Figure 8. σ_z along Interface of $[0/90]_s$ Laminate (ε_x=-0.1%)

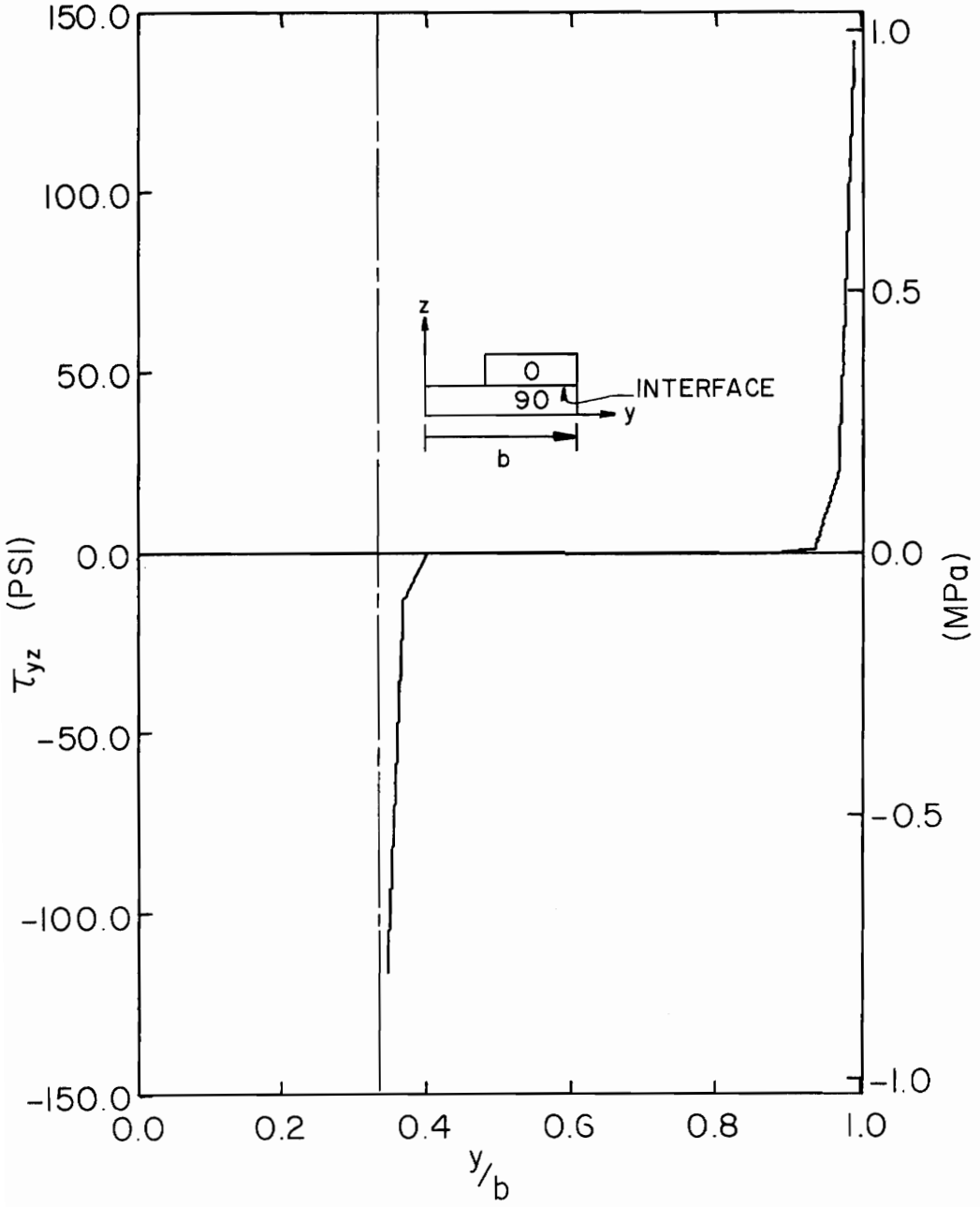

Figure 9. τ_{yz} along Interface of $[0/90]_s$ Laminate (ε_x=-0.1%)

σ_y^L is the theoretical laminate value. To satisfy moment equilibrium, the following must also be true.

$$\int_A^C \sigma_z y dy = \sigma^L{}_y (h_o^2/2)$$
$$\int_C^B \sigma_z y dy = -\sigma_y^L (h_o^2/2) \qquad (5.2)$$

For the reasons cited in Section 5.2 and because the stresses are not known at the exact edge, these conditions are not well satisfied. However, by assuming a linear stress distribution from the last point given by the finite element method to the edge of the laminate, the equilibrium conditions 5.1 and 5.2 can be satisfied within two percent. A larger number of elements at the edges would also tend to satisfy the conditions more accurately.

Each of the Figs. 7, 8 and 9 show the free and cutout edge effects extending approximately 14 h_o into the interior of the laminate. The free edge stresses are slightly larger than the stress values at the cutout edge. Thus, for this laminate, the free edge is more critical than the cutout edge.

The value of the Tsai-Wu function is largest at the free edge, again showing that the free edge is most critical. The through-the-thickness variation of the Tsai-Wu function near the free edge, Fig. 10, indicates that the largest value occurs near the top ($z/h_o = 2.0$) of the laminate. (The values of the Tsai-Wu function in Fig. 10 have been scaled to be between 0 and 1.) Examining the terms of the Tsai-Wu function for a 0° layer (Equ. 3.23), the critical term was determined to

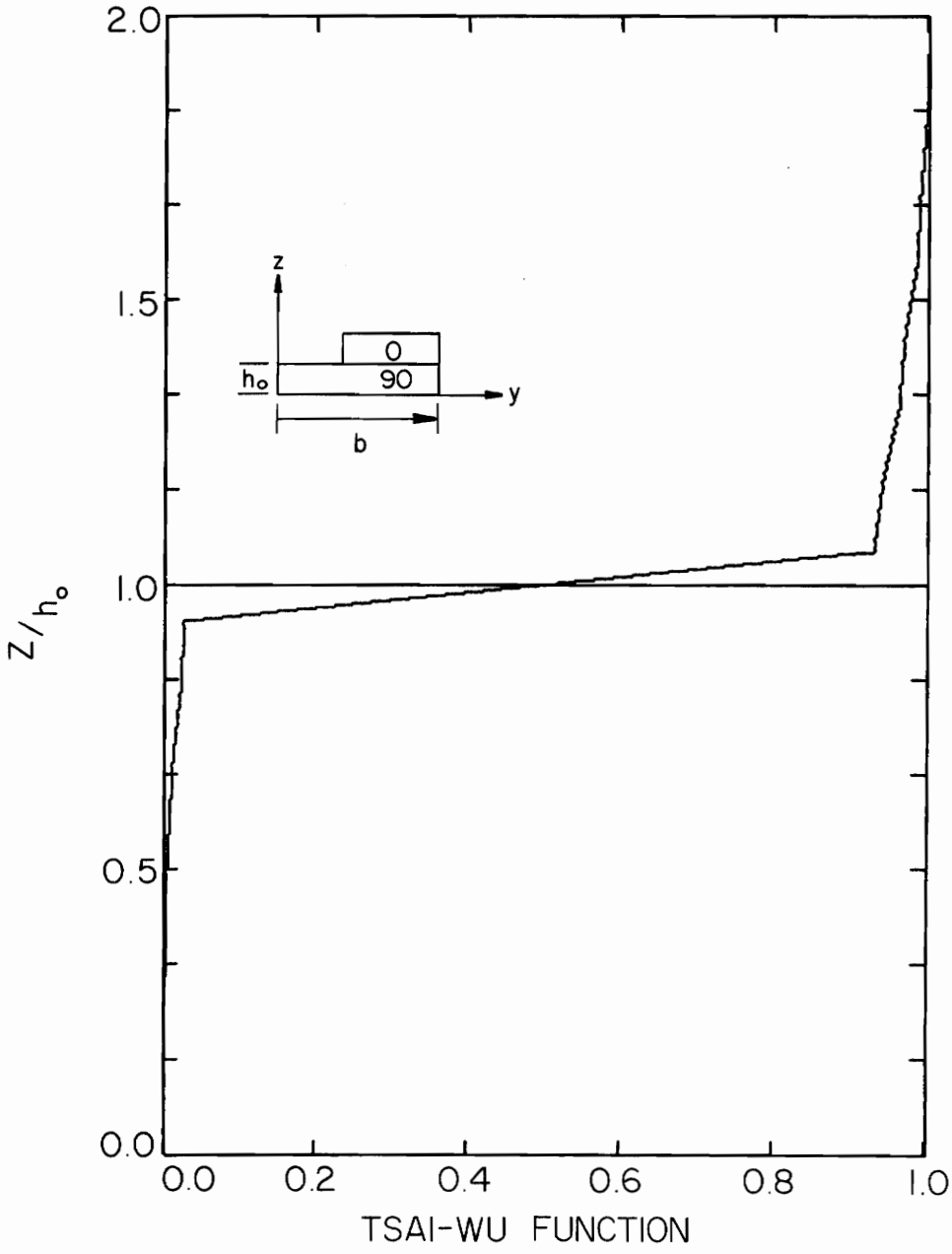

Figure 10. Through-Thickness Distribution of Tsai-Wu Function for $[0/90]_s$ Laminate (ε_x=-0.1%, y/b=0.99)

be $F_2\sigma_y(\sigma_y=\sigma_2)$. Noting Fig. 11, which shows the through-the-thickness variation of σ_y, the critical term will have the largest absolute value near the interface. Since σ_y in the 0° layer is negative, $F_2\sigma_y$ is less at the interface than near the top. This indicates failure may begin near the free edge and near the top of the $[0/90]_s$ laminate.

5.3.2.2 The $[\pm45]_s$ Laminate

A cutout in the $[\pm45]_s$ laminate produces a number of important effects, particularly near the cutout. Figure 12 shows σ_x in the +45° layer rising to a value 124 percent above the stress in the interior region. From a value of zero in the interior, the σ_y stress (Fig. 13) attains a value of approximately -1000 psi near the cutout. The dashed line in Fig. 13 indicates the variation of σ_y in the -45° layer from point E to point A. The τ_{xy} stress (Fig. 14) in the +45° layer near the cutout rises to a value 160 percent above the lamination value in the interior. The interior region values for the σ_x, σ_y and τ_{xy} stresses, which are the same as the theoretical lamination values, are given in Table 1. Again, as in the $[0/90]_s$ laminate, free edge distributions for all stresses are the same with or without a cutout.

The σ_z stress, Fig. 15, shows an extremely important effect of the cutout. Moment equilibrium (Equ's. 5.2) requires that

$$\int_A^C \sigma_z y dy = 0$$

$$\int_C^B \sigma_z y dy = 0 \qquad (5.3)$$

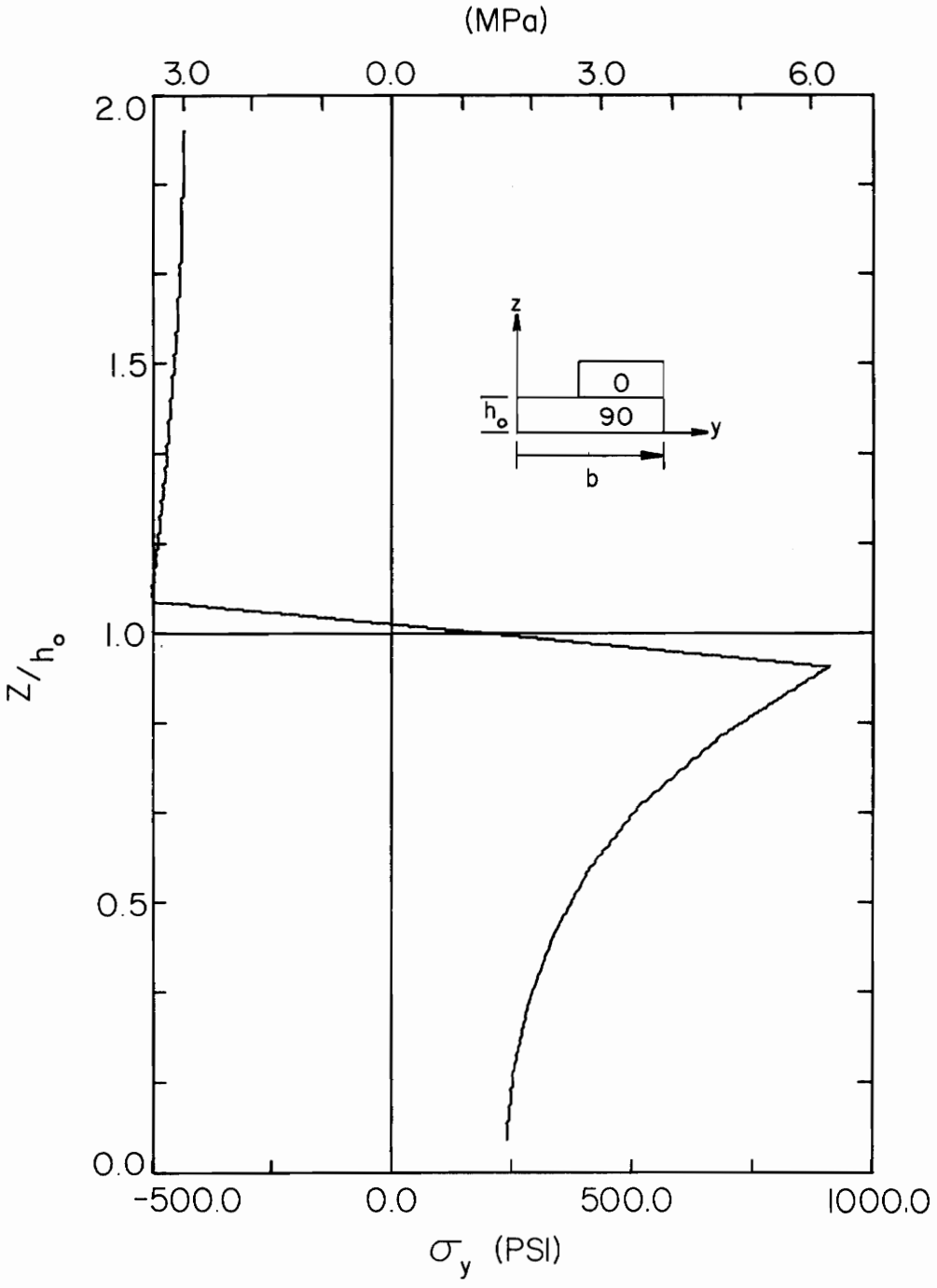

Figure 11. Through-Thickness Distribution of σ_y for $[0/90]_s$ Laminate (ε_x=-0.1%, y/b=0.99)

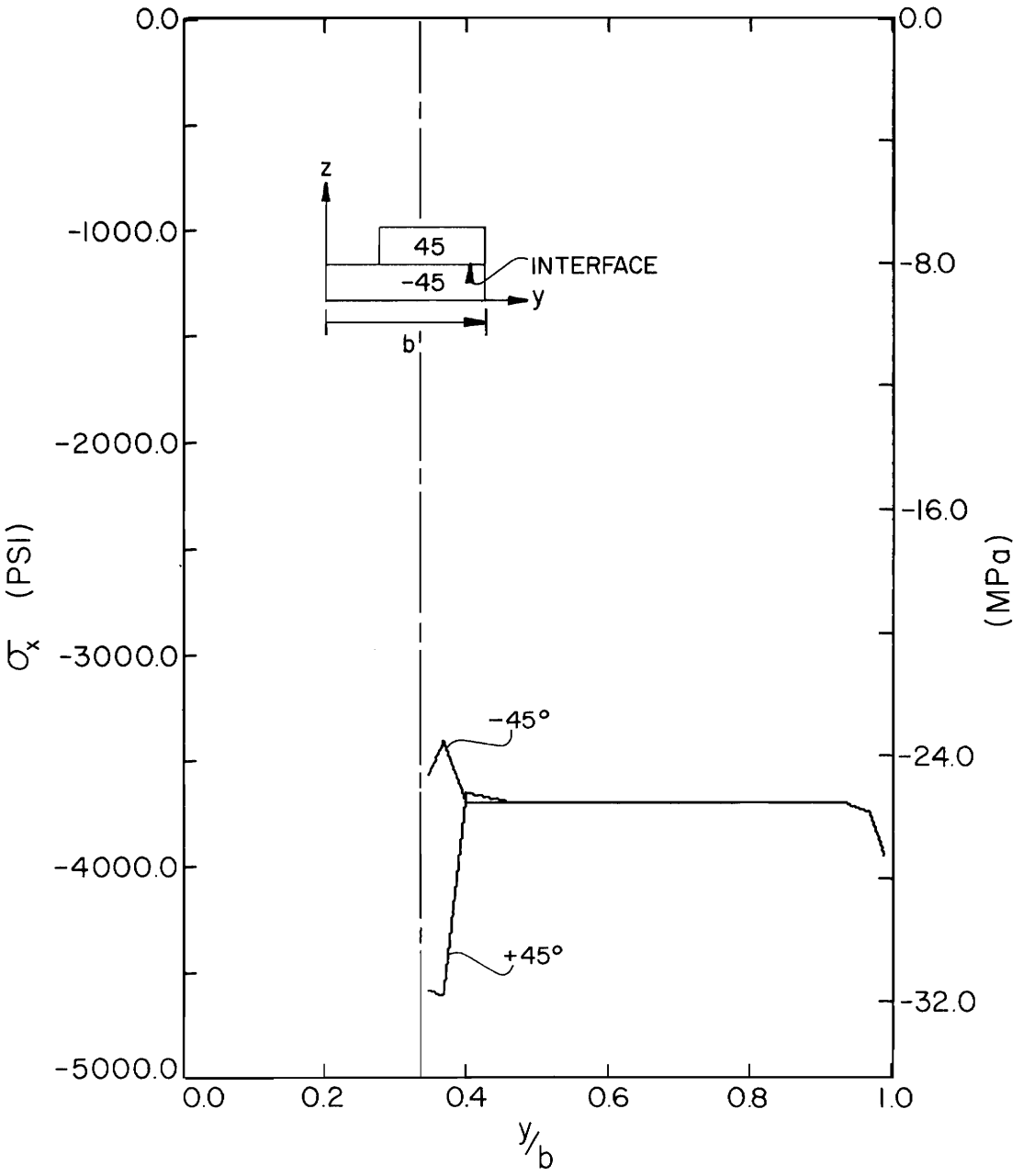

Figure 12. σ_x along Interface of $[\pm 45]_s$ Laminate (ε_x=-0.1%)

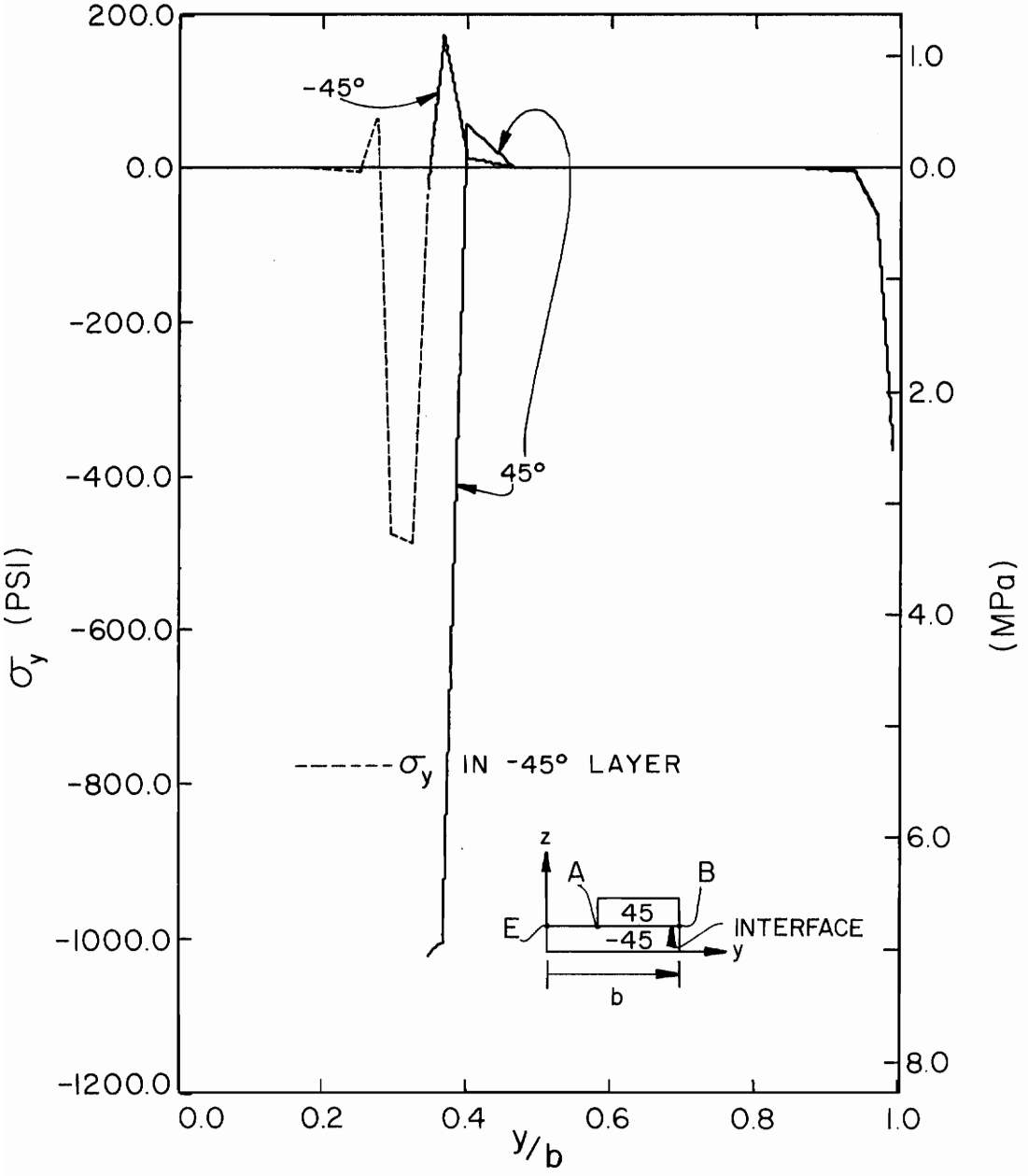

Figure 13. σ_y along Interface of $[\pm 45]_s$ Laminate (ε_x=-0.1%)

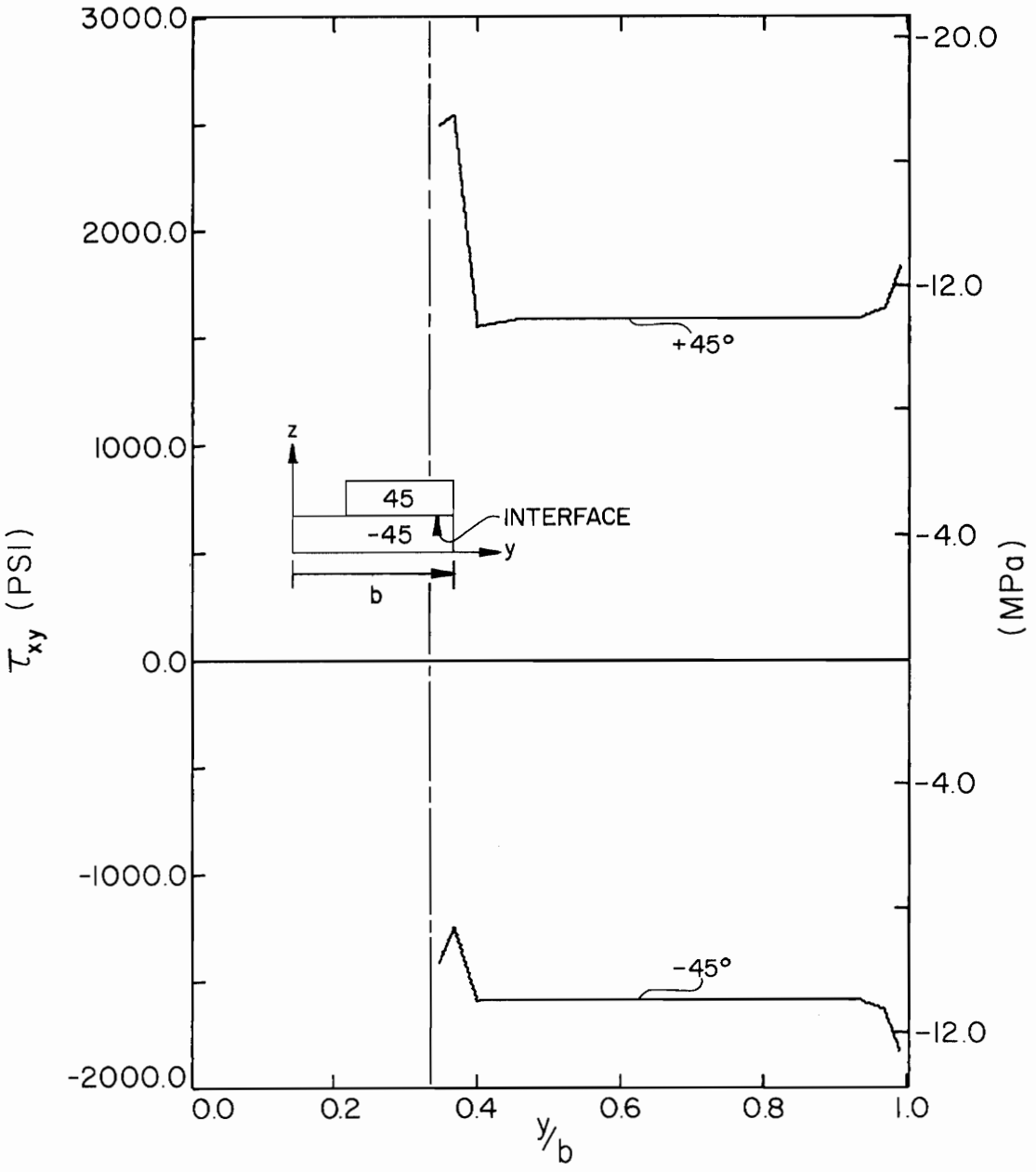

Figure 14. τ_{xy} along Interface of $[\pm 45]_s$ Laminate (ε_x=-0.1%)

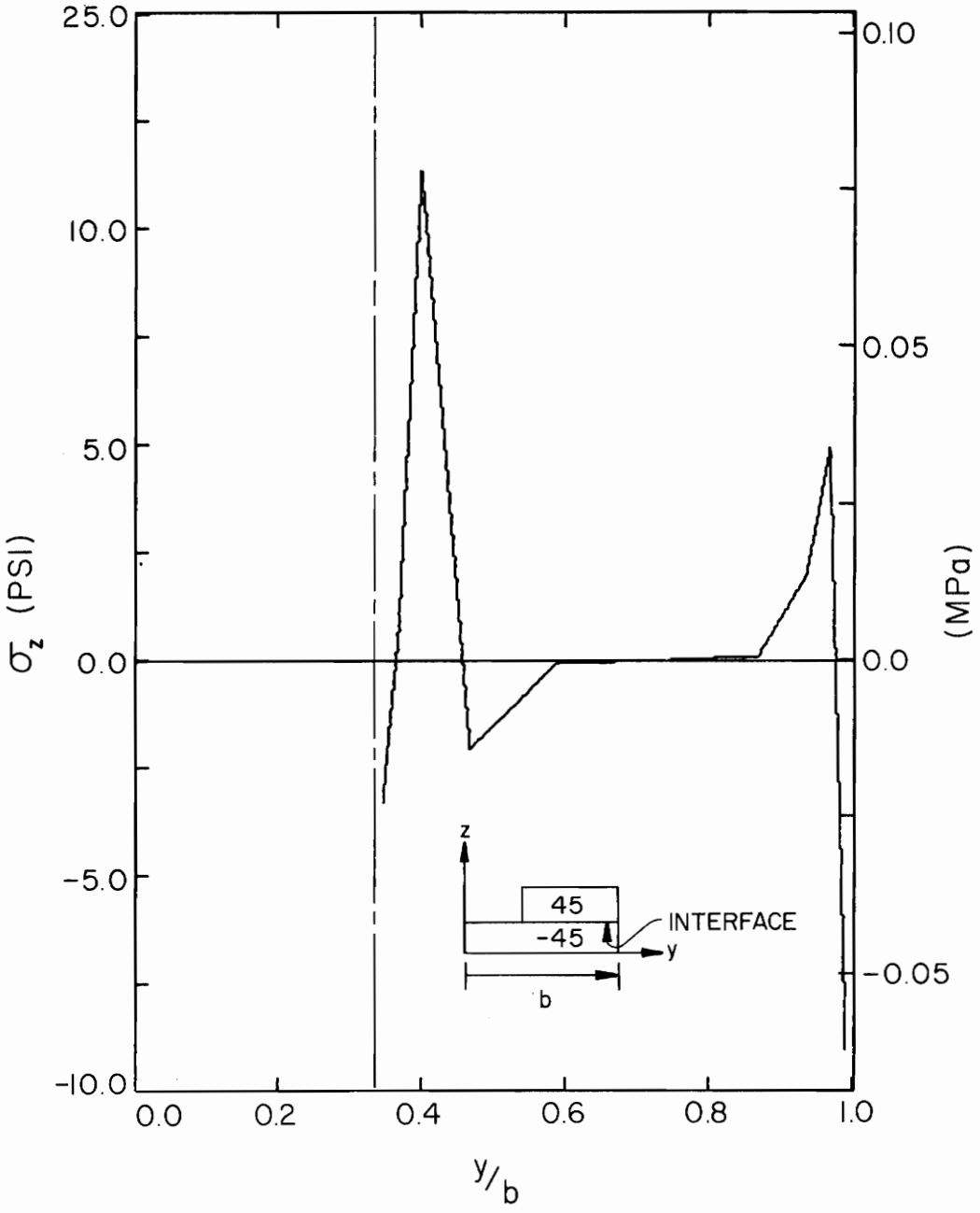

Figure 15. σ_z along Interface of $[\pm 45]_s$ Laminate (ε_x=-0.1%)

since σ_y^L is zero in the interior region. The σ_z variation near the cutout shows the correct trend, having three envelopes to produce a zero moment. The σ_z variation near the free edge, however, does not show the correct trend due to a steeper displacement gradient in this area. In addition, the σ_z variation shows the effect of the cutout edge extending twice as far into the interior region as the free edge effect.

The τ_{yz} and τ_{xz} shear stresses, shown in Figs. 16 and 17, respectively, also exhibit the influence of the cutout edge. The τ_{yz} stress near the cutout is very large in comparison to the same stress near the free edge while the τ_{xz} stress near the cutout is only slightly larger than the free edge value. In addition, the τ_{xz} distribution has two envelopes near the cutout whereas the single envelope at the free edge is the distribution expected. However, force equilibrium of the left top section of Fig. 6 between cutting planes JJ and CC requires that

$$\int_F^G \tau_{xy} dZ + \int_C^D \tau_{xy} dZ + \int_F^C \tau_{xz} dY = 0 \qquad (5.4)$$

Since τ_{xy} is greater along line JJ than CC (Fig. 14) and by convention in the opposite direction, the integral of τ_{xz} must be negative (and thus, by convention, in the positive direction). As the cutting plane JJ is moved closer to the cutout edge, τ_{xy} goes to zero and the integral of τ_{xz} becomes positive to balance the τ_{xy} on plane CC (a similar τ_{xz} stress distribution should exist near the free edge but doesn't due to the coarseness of the grid). Similar arguments can be advanced to explain the two envelopes of the τ_{yz} distribution (Fig. 16) involving the σ_y stresses.

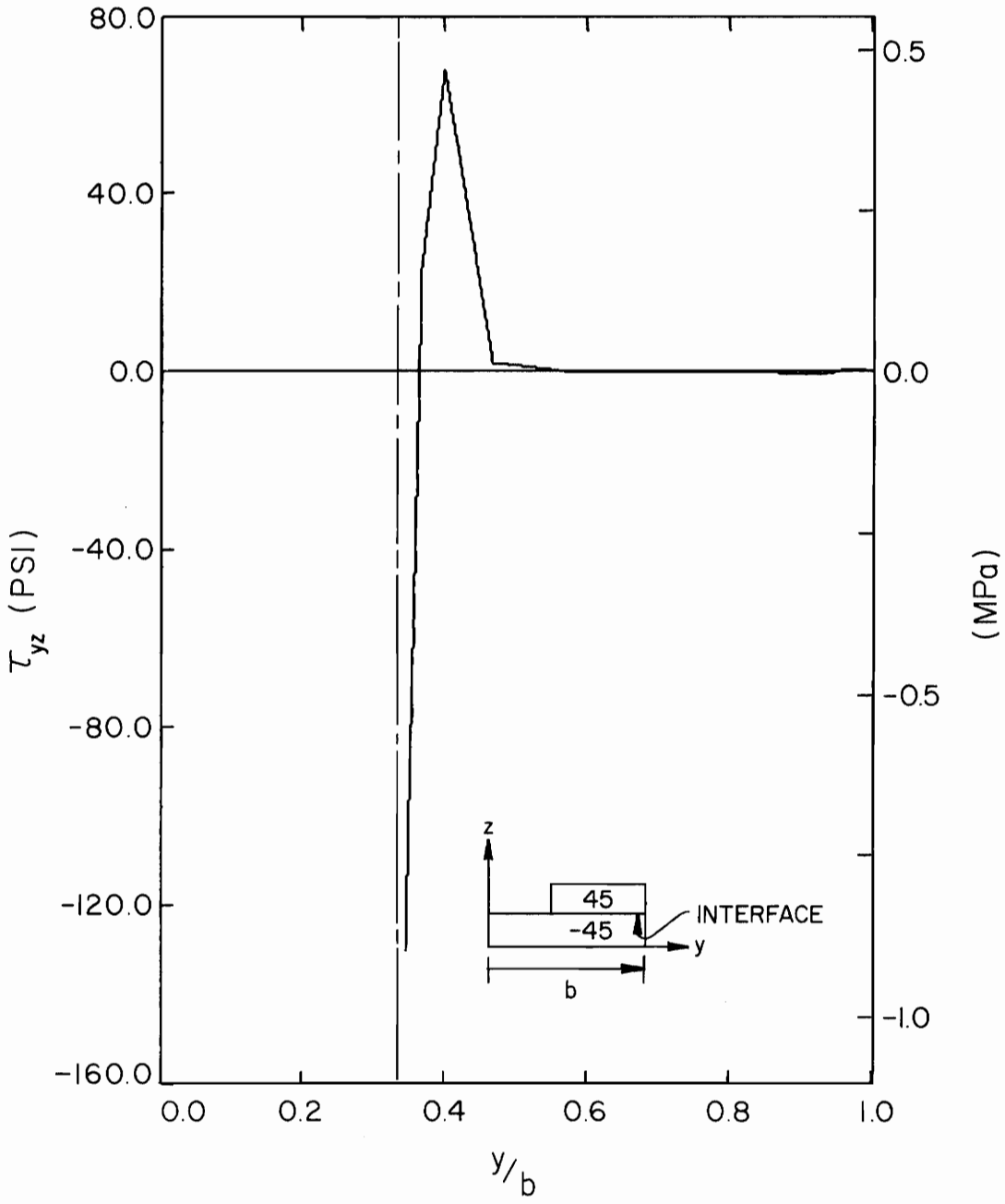

Figure 16. τ_{yz} along Interface of $[\pm 45]_s$ Laminate (ε_x=-0.1%)

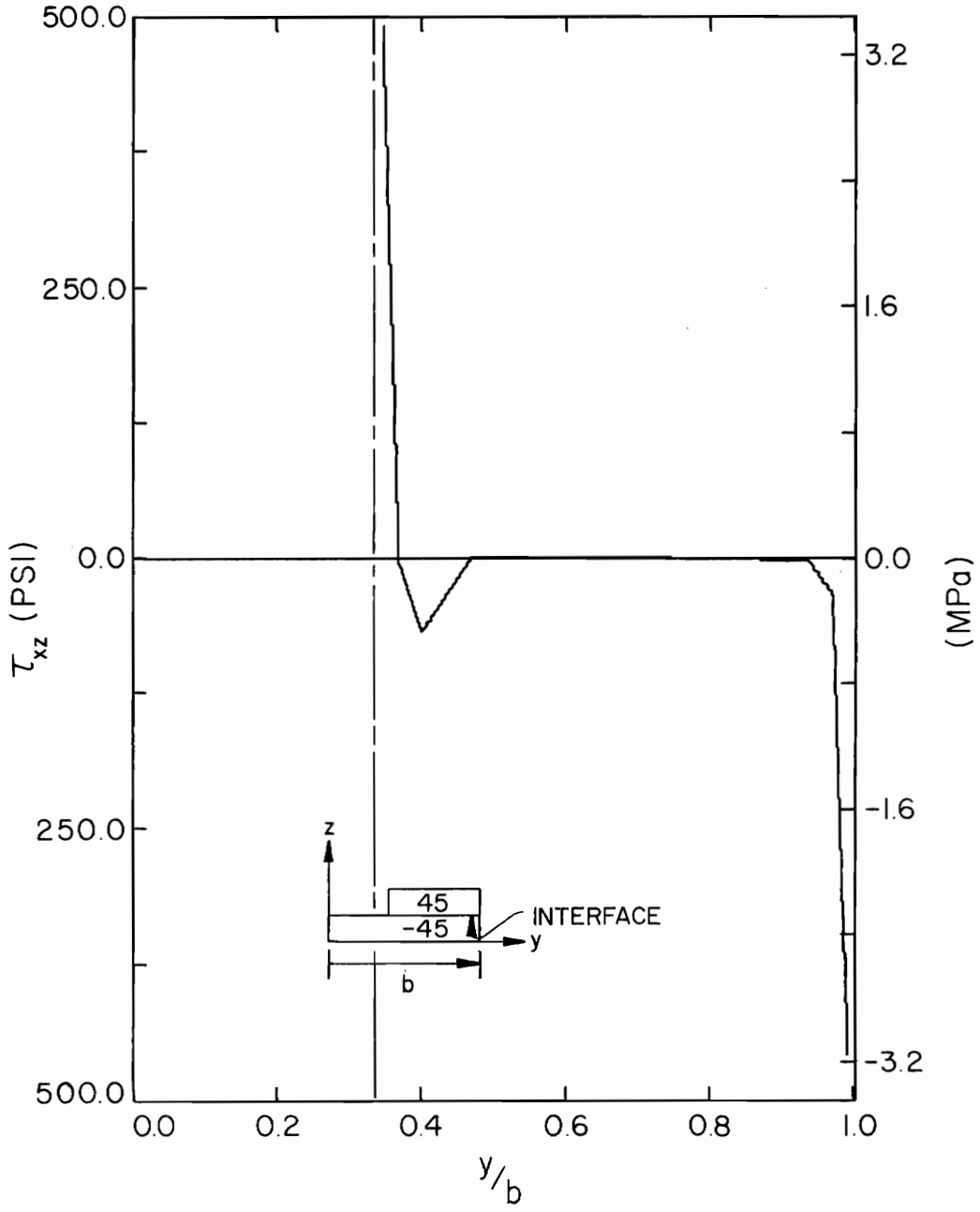

Figure 17. τ_{xz} along Interface of $[\pm 45]_s$ Laminate (ε_x=-0.1%)

The Tsai-Wu function along the interface (Fig. 18) indicates the largest value occurs in the interior of the -45° layer near y/b = 0.4. The through-the-thickness variation near this point (Fig. 19) shows the largest value occurring not at the ±45 interface but near the midplane (z/h_o = 0.0). The through-the-thickness variation of stresses indicates that the σ_z stress (Fig. 20) is the principal cause of the maximum Tsai-Wu value occurring at the midplane. The σ_z stress rises to a maximum at the midplane in order to balance the moment produced by the σ_y stress (Fig. 21) along the plane y/b = 0.4. Thus, failure may initiate at the midplane and a small distance in from the cutout.

5.3.3 Eight Layer Laminates

Partial free body diagrams of the quarter section of eight layer laminates with cutouts are shown in Figs. 22 and 23. There are three interfaces, referred to in the following manner: the upper interface from point A to B, the middle interface from point C to D, and the lower interface from point E to F. Also, the interior region refers to the section away from the free and cutout edges where the line KK is shown. In the interior region, the laminate solution for a $[\theta_1/\theta_2/\theta_3/\theta_4]_s$ laminate holds. The laminate solution also holds near the centerline (y=0), but for a $[\theta_2/\theta_3/\theta_4]_s$ or $[\theta_3/\theta_4]_s$ laminate, depending on whether one or two layers is removed.

5.3.3.1 The $[0_2/\pm45]_s$ Laminate

The σ_y stress distributions for a one layer cutout and for a two layer cutout are presented in Figs. 24 and 25 respectively. Each shows the value of σ_y changing from the centerline laminate value to the

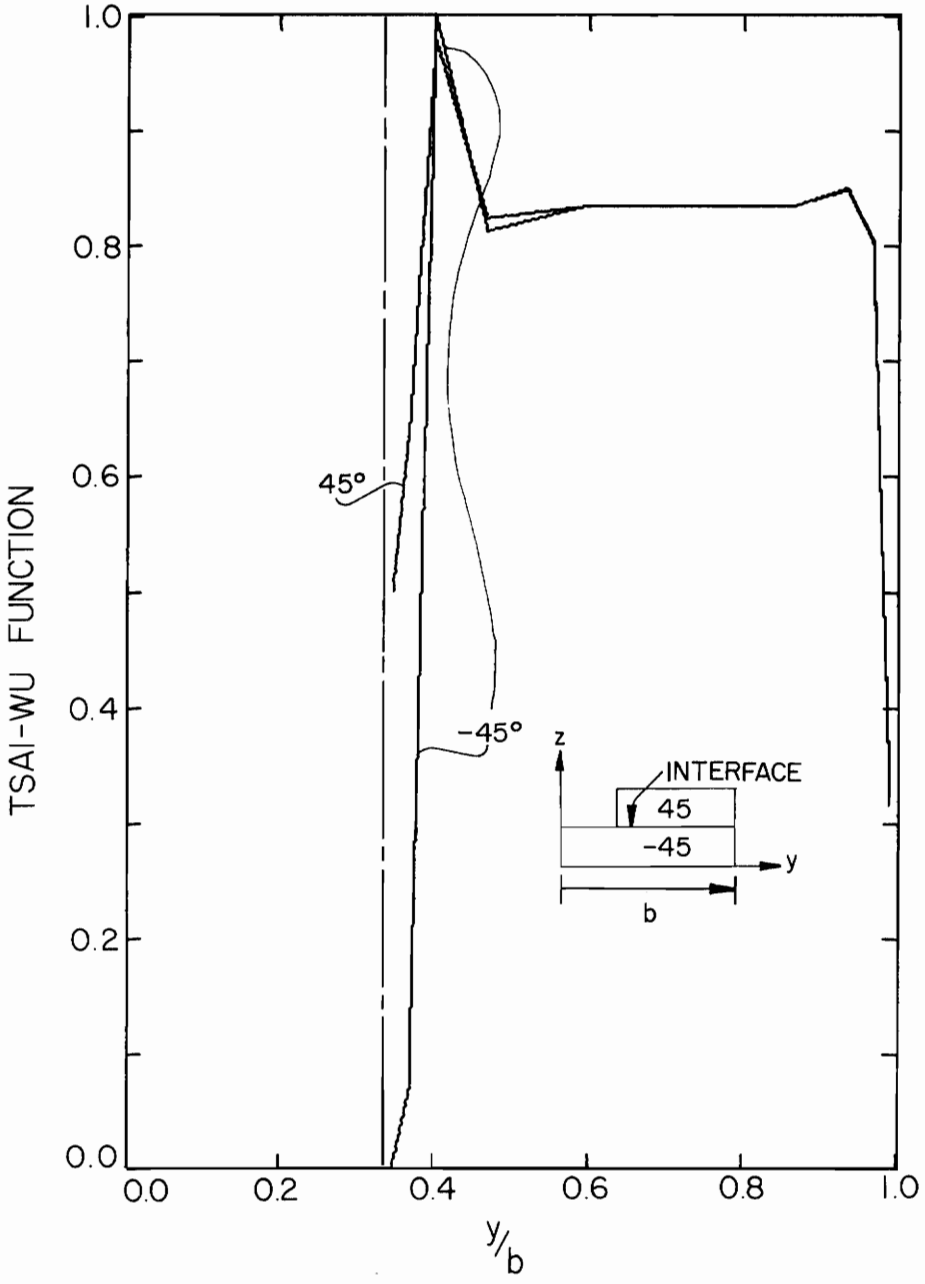

Figure 18. Distribution of Tsai-Wu Function along Interface of $[\pm 45]_s$ Laminate (ε_x=-0.1%)

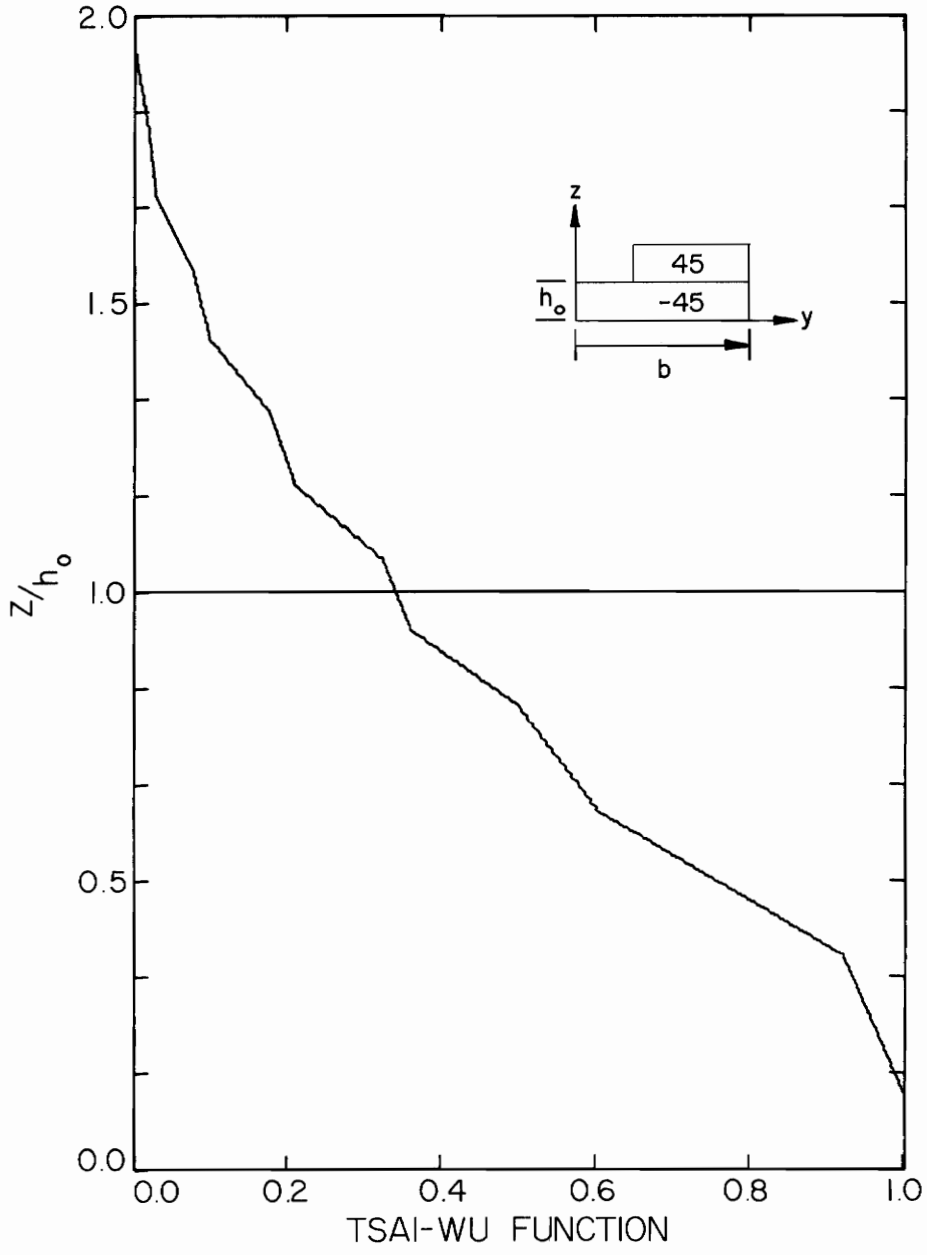

Figure 19. Through-Thickness Distribution of Tsai-Wu Function for $[\pm 45]_s$ Laminate (ε_x=-0.1%, y/b=0.40)

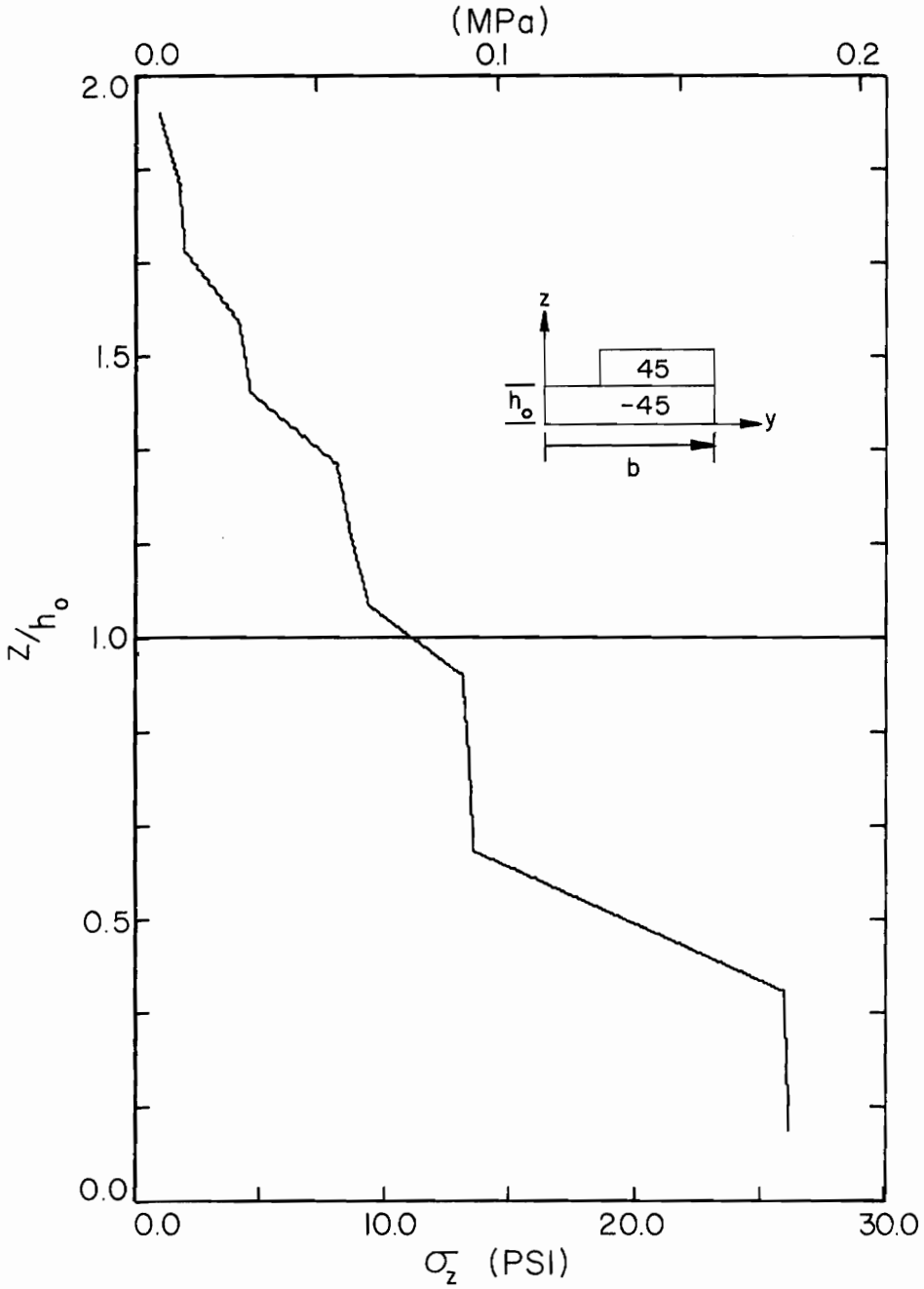

Figure 20. Through-Thickness Distribution of σ_z for a $[\pm 45]_s$ Laminate (ξ_x=-0.1%, y/b=0.40)

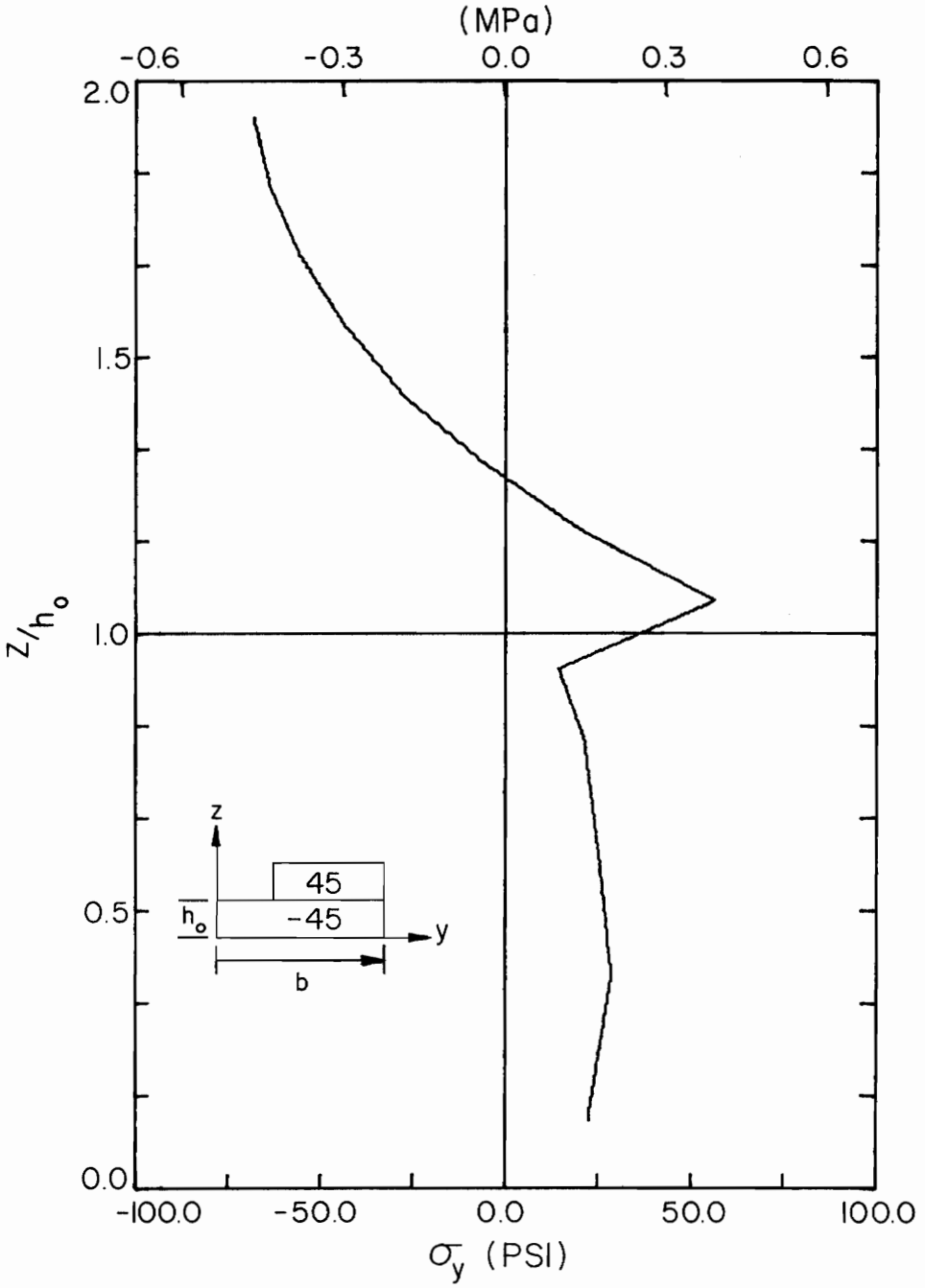

Figure 21. Through-Thickness Distribution of σ_y for $[\pm 45]_s$ Laminate (ε_x=-0.1%, y/b=0.40)

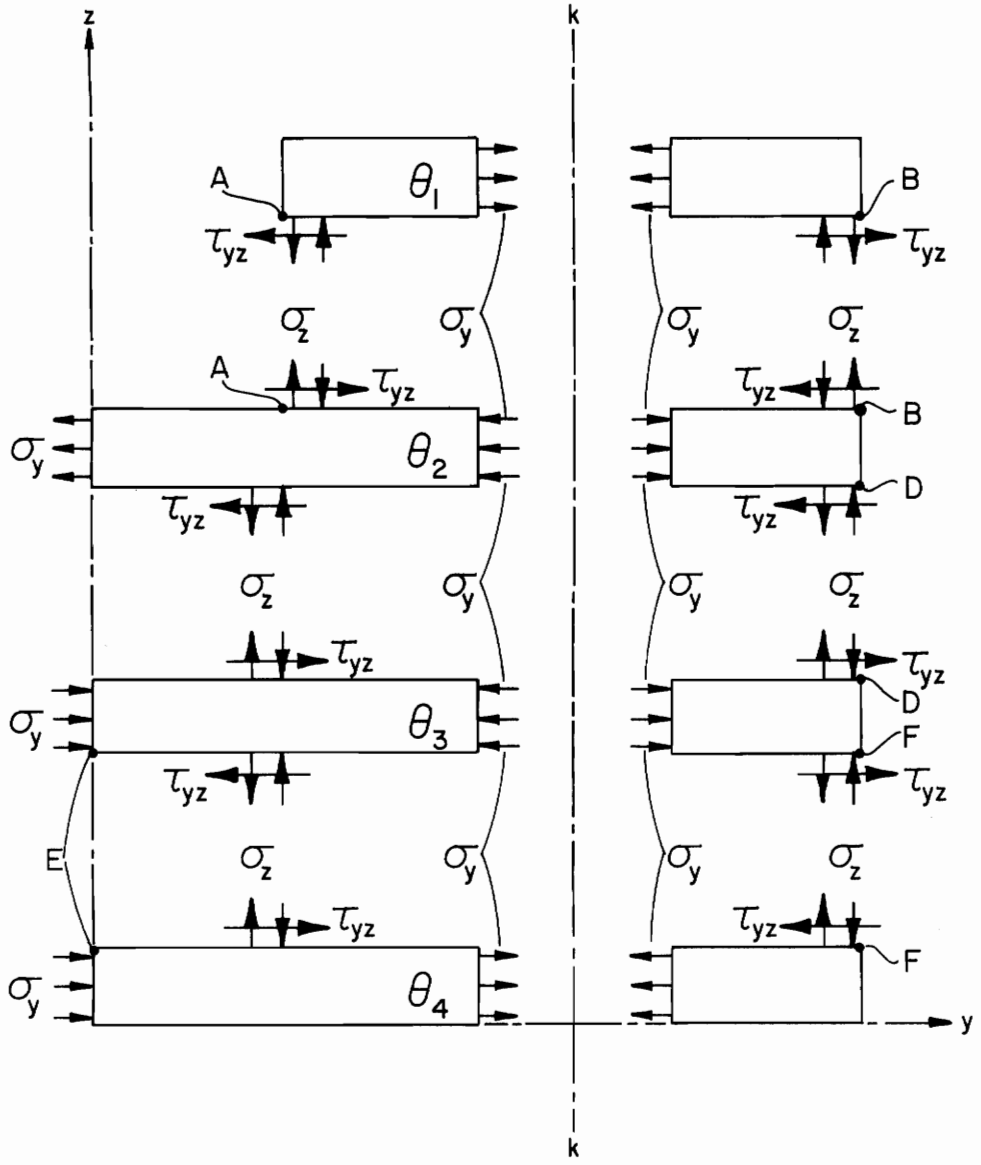

Figure 22. Partial Free Body Diagram of Quarter Cross-Section of Damaged Eight Layer Symmetric Lamiante (One Layer Cutout)

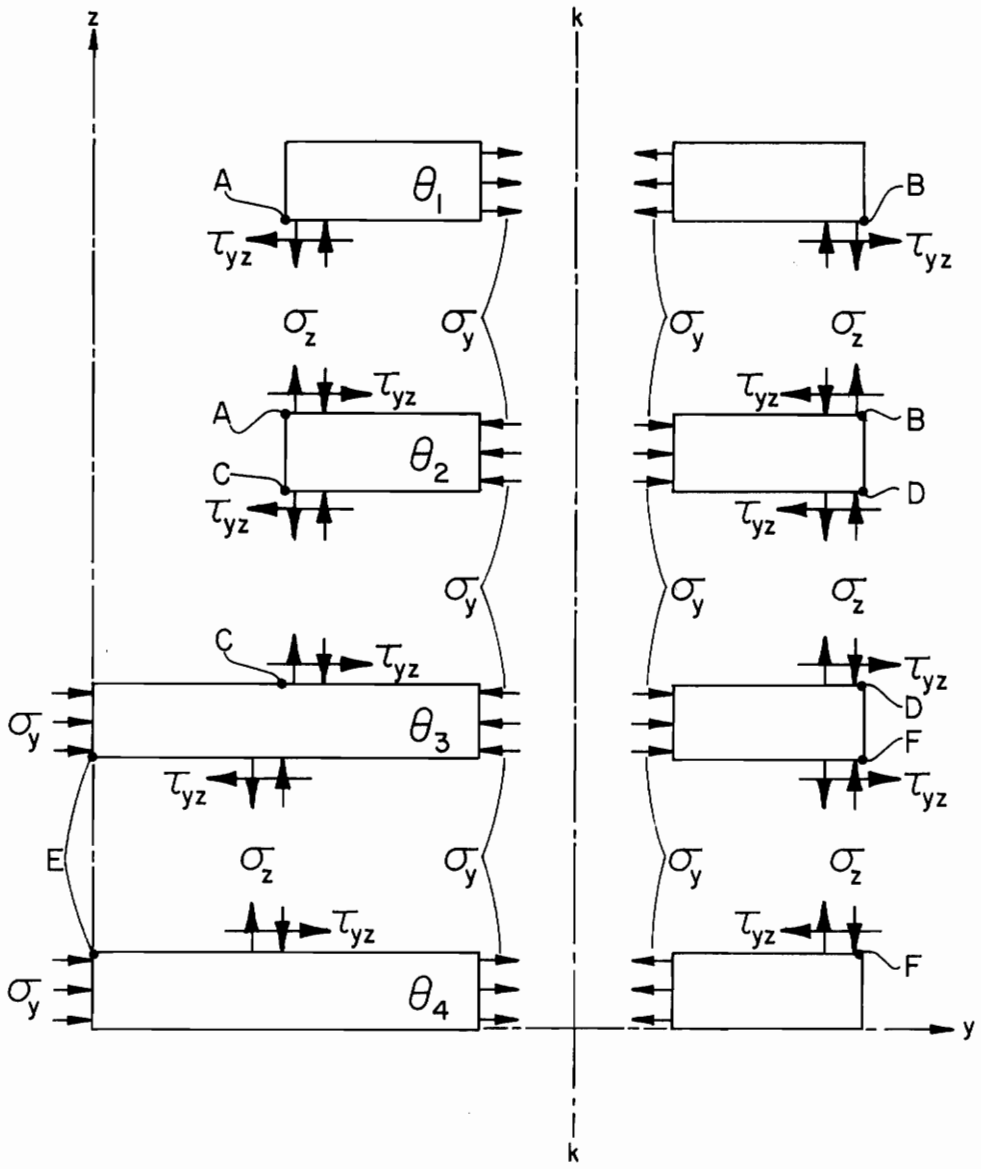

Figure 23. Partial Free Body Diagram of Quarter Cross-Section of Damaged Eight Layer Symmetric Lamiante (Two Layer Cutout)

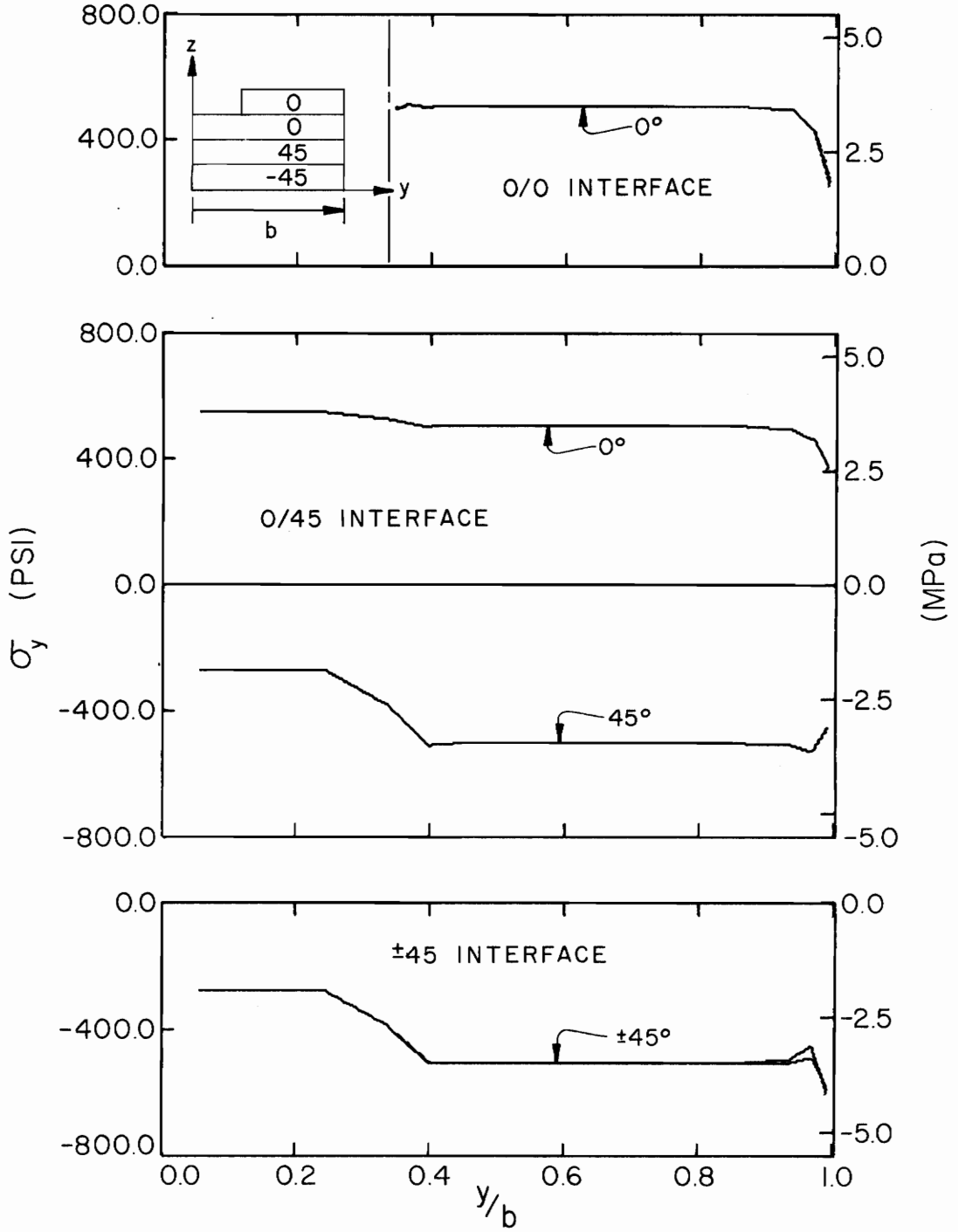

Figure 24. σ_y along the Interfaces of $[0_2/\pm 45]_s$ Laminate with One Layer Cutout (ε_x=-0.1%)

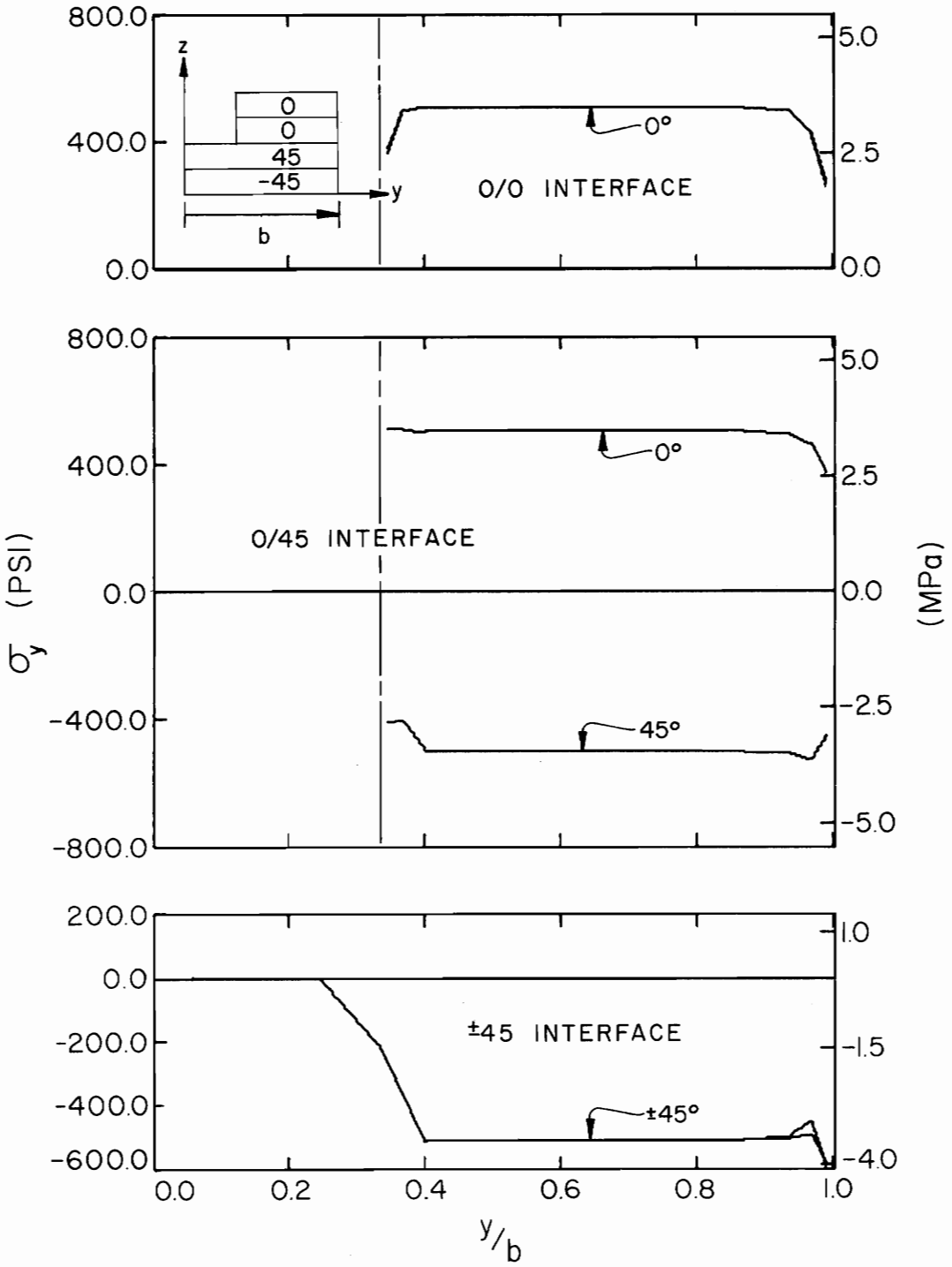

Figure 25. σ_y along the Interfaces of $[0_2/\pm45]_s$ Laminate with Two Layer Cutout (ε_x=-0.1%)

interior region laminate value. The finite element results in those regions for σ_x and τ_{xy}, as well as σ_y, are exactly equal to the laminate values. The presence of the cutout, whether one or two layers, does not significantly increase the magnitude of those stress components at the cutout edge. Further, all stress components at the free edge have the same variation with or without a cutout.

The cutout does have an unusual effect on the σ_z distributions as shown in Fig. 26, which gives the results for a laminate with a two layer cutout. Along the lower interface a couple is produced to balance the moment produced by the σ_y stresses in the interior region (line KK, Fig. 23). Though not as high as the stresses produced at the free edge, this resultant σ_z couple in the material just below the cutout edge (y/b = 0.33) could initiate failure if a flaw existed in this region.

Typical τ_{yz} and τ_{xz} distributions are shown in Figs. 27 and 28, respectively, for a laminate with a one layer cutout. The distribution for a two layer cutout are similar except that (as expected) the middle interface distribution resembles the upper interface distribution. For the τ_{yz} distributions (Fig. 27), the envelopes near y/b = 0.33 on the middle and lower interfaces are necessary for force equilibrium (εF_y = 0). For τ_{xz} (Fig. 28), the double envelopes near the free edge on both the upper and middle interface are caused by a slight rise in τ_{xy} near the free edge (by reasoning similar to Section 5.3.2.2).

5.3.3.2 The $[\pm 45/0_2]_s$ Laminate

The σ_z stresses, shown in Figs. 29 and 30 for one and two layer

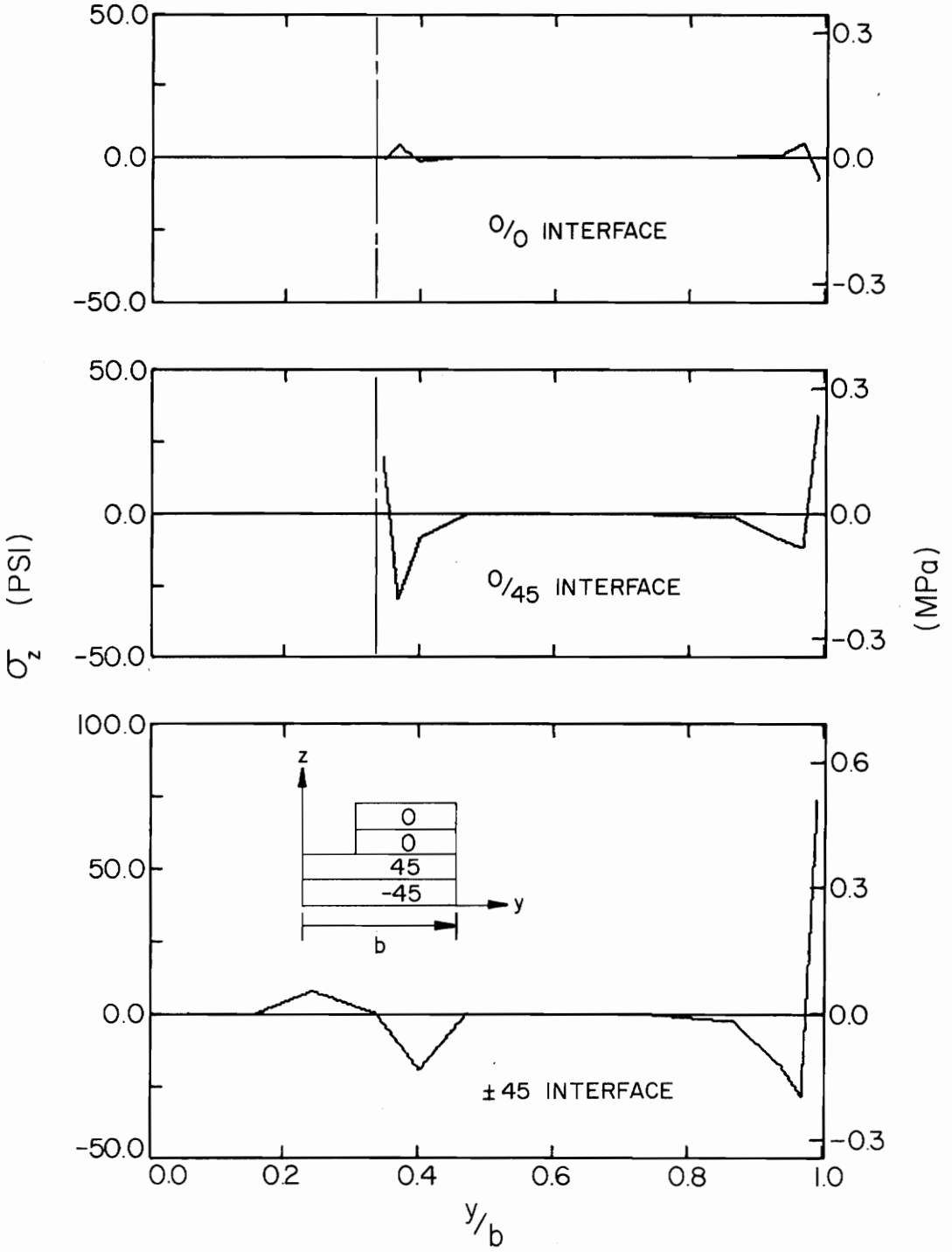

Figure 26. σ_z along the Interfaces of $[0_2/\pm 45]_s$ Laminate with Two Layer Cutout (ε_x=-0.1%).

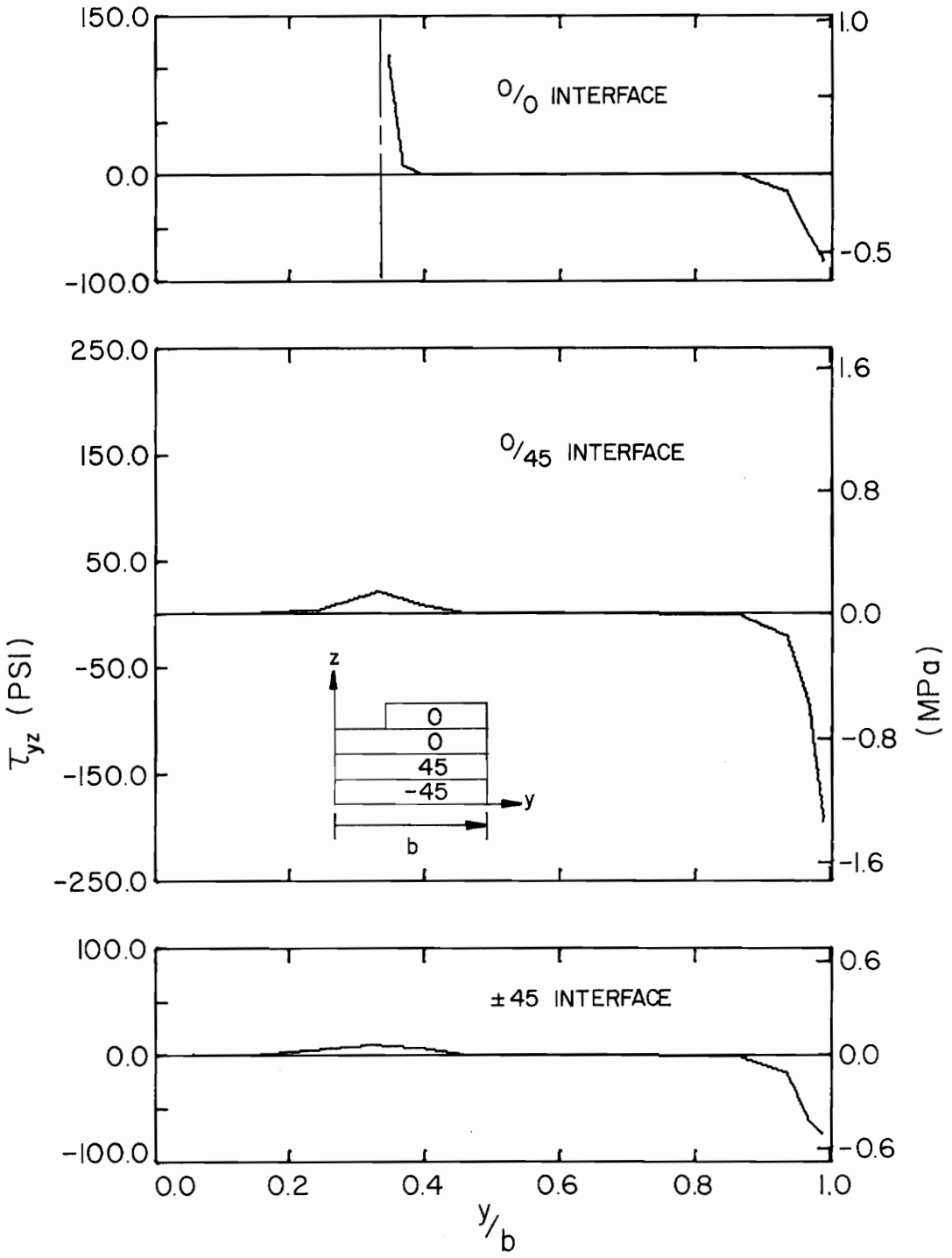

Figure 27. τ_{yz} along the Interfaces of $[0_2/\pm45]_s$ Laminate with One Layer Cutout (ε_x=-0.1%).

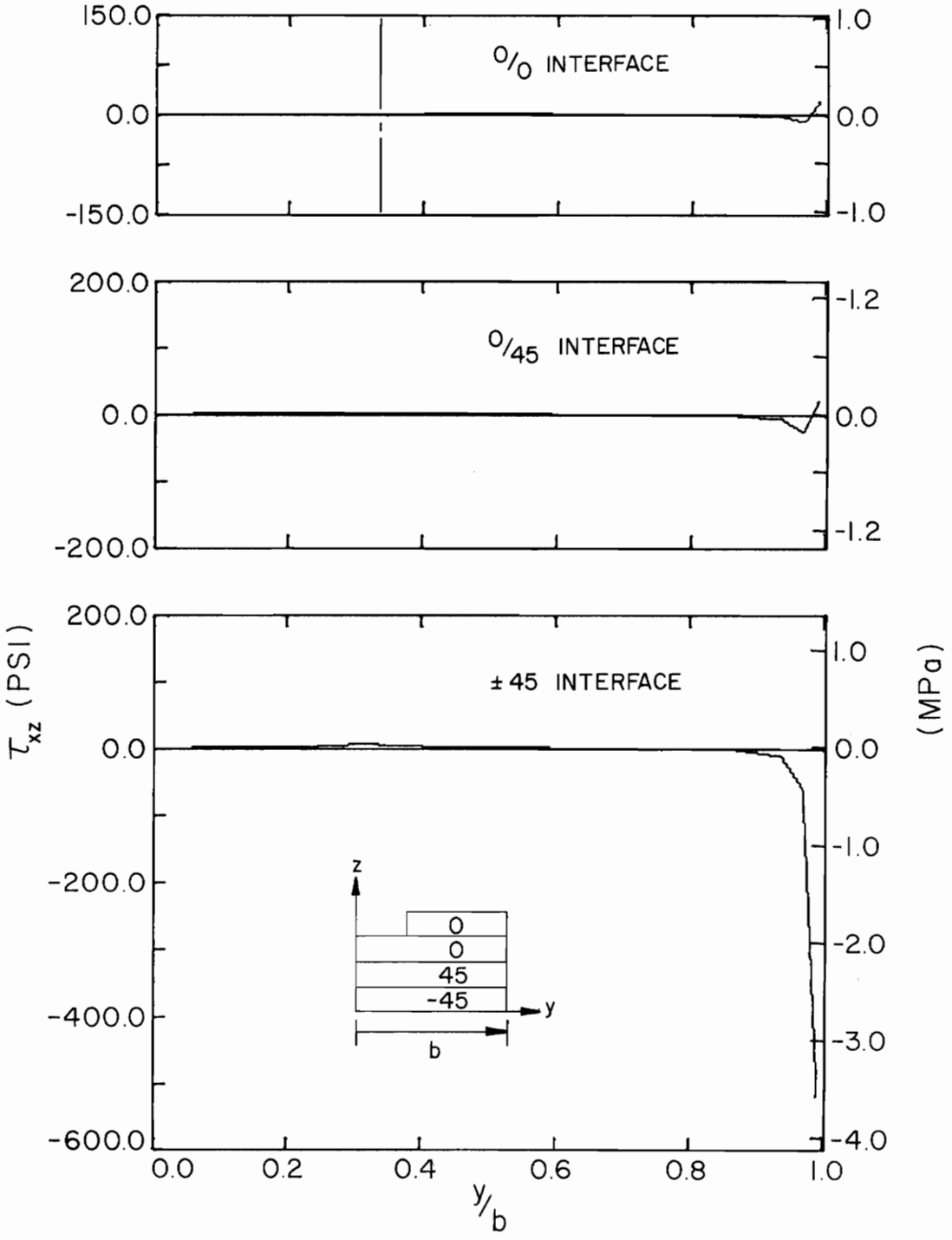

Figure 28. τ_{xz} along the Interfaces of $[0_2/\pm 45]_s$ Laminate with One Layer Cutout (ξ_x=-0.1%).

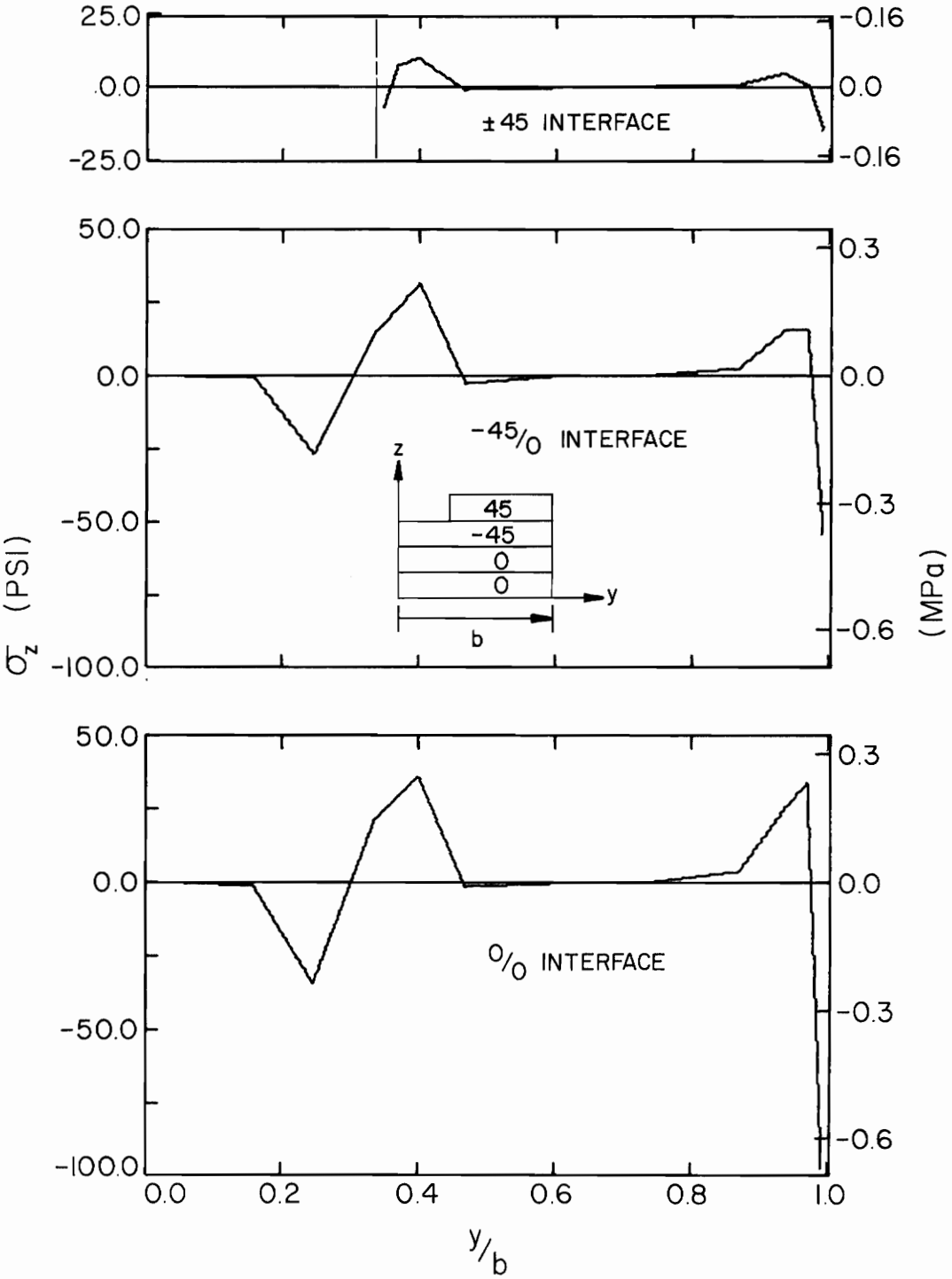

Figure 29. σ_z along the Interfaces of $[\pm 45/0_2]_s$ Laminate with One Layer Cutout (ξ_x=-0.1%).

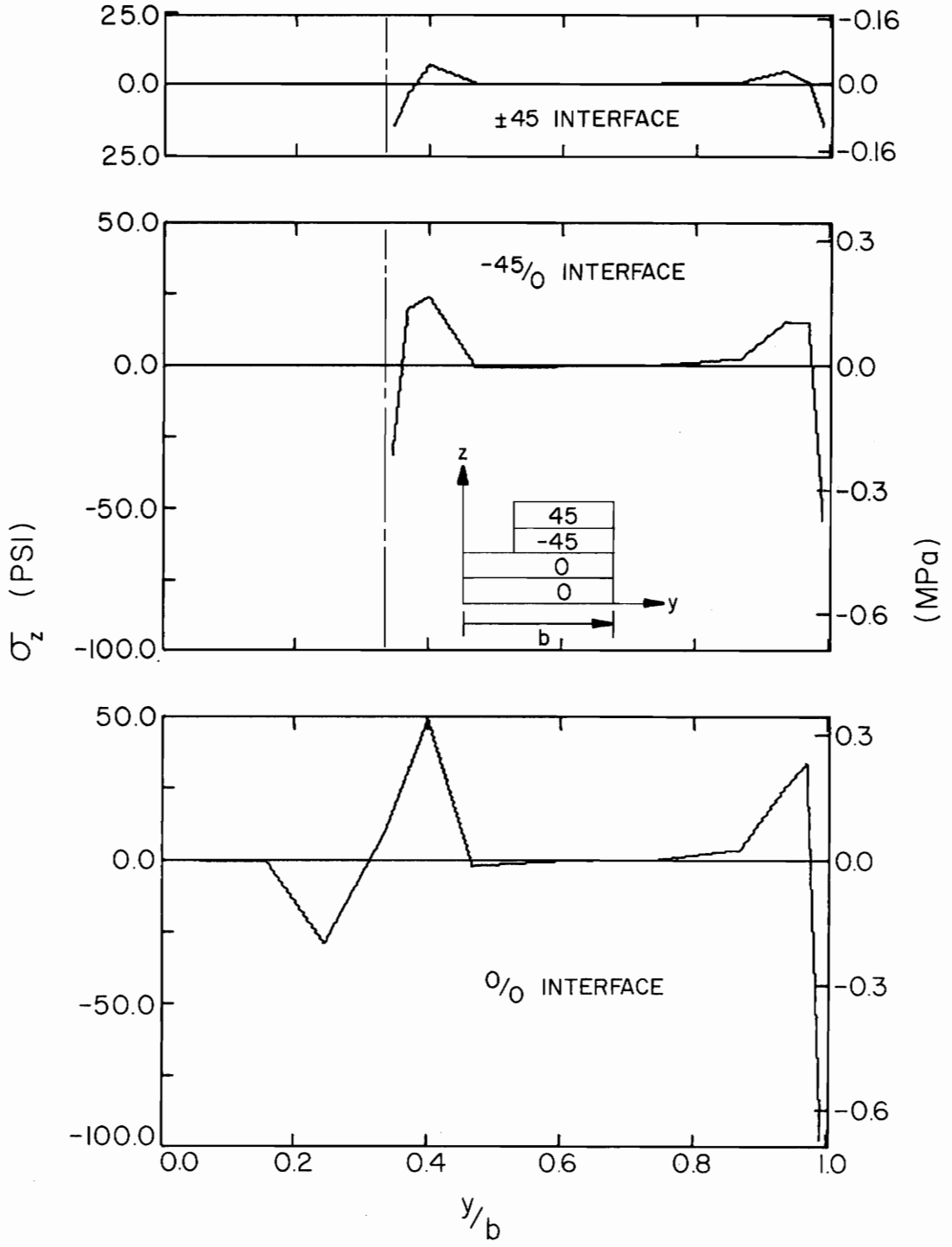

Figure 30. σ_z along the Interfaces of $[\pm 45/0_2]_s$ Laminate with Two Layer Cutout (ε_x=-0.1%).

cutouts are the most important stresses for this laminate. As can be seen from both figures, the tensile σ_z stresses along the interfaces below the cutout are the highest tensile stress encountered. In fact, the tensile σ_z stress on the lower interface of the $[\pm 45/0_2]_s$ laminate with a two layer cutout (Fig. 30) is the largest tensile σ_z stress near the cutout for either a $[\pm 45/0_2]_s$ or $[0_2/\pm 45]_s$ laminate with or without a cutout. As before, this suggests failure may occur along this interface, particularly if it is a flawed or damaged region.

The τ_{xz} stress distributions along the interfaces for one and two layer cutouts (Figs. 31 and 32, respectively) have several interesting differences. Along the lower interface, the τ_{xz} envelope just below the cutout peaks at a higher value in the one layer cutout than in the two layer cutout. Further, the negative envelope near the cutout along the upper interface of the one layer cutout is not present in the distribution along the same interface in the two layer cutout. A similar pattern occurs in the τ_{yz} distribution (Fig. 33) along the upper interface where the two envelopes near one layer cutout do not occur in the two layer cutout. Again, arguments similar to those presented in Section 5.3.2.2 can explains these patterns, particularly since τ_{xy} and σ_y near the cutout in the +45° layer rise to values 142 percent and 275 percent, respectively, above the interior region values for a laminate with a one layer cutout.

The Tsai-Wu function for this laminate attains its maximum value in the zero degree layer near y/b = 0.4 for both one and two layer cutouts as shown in Figs. 34 and 35. This point concides with the point of

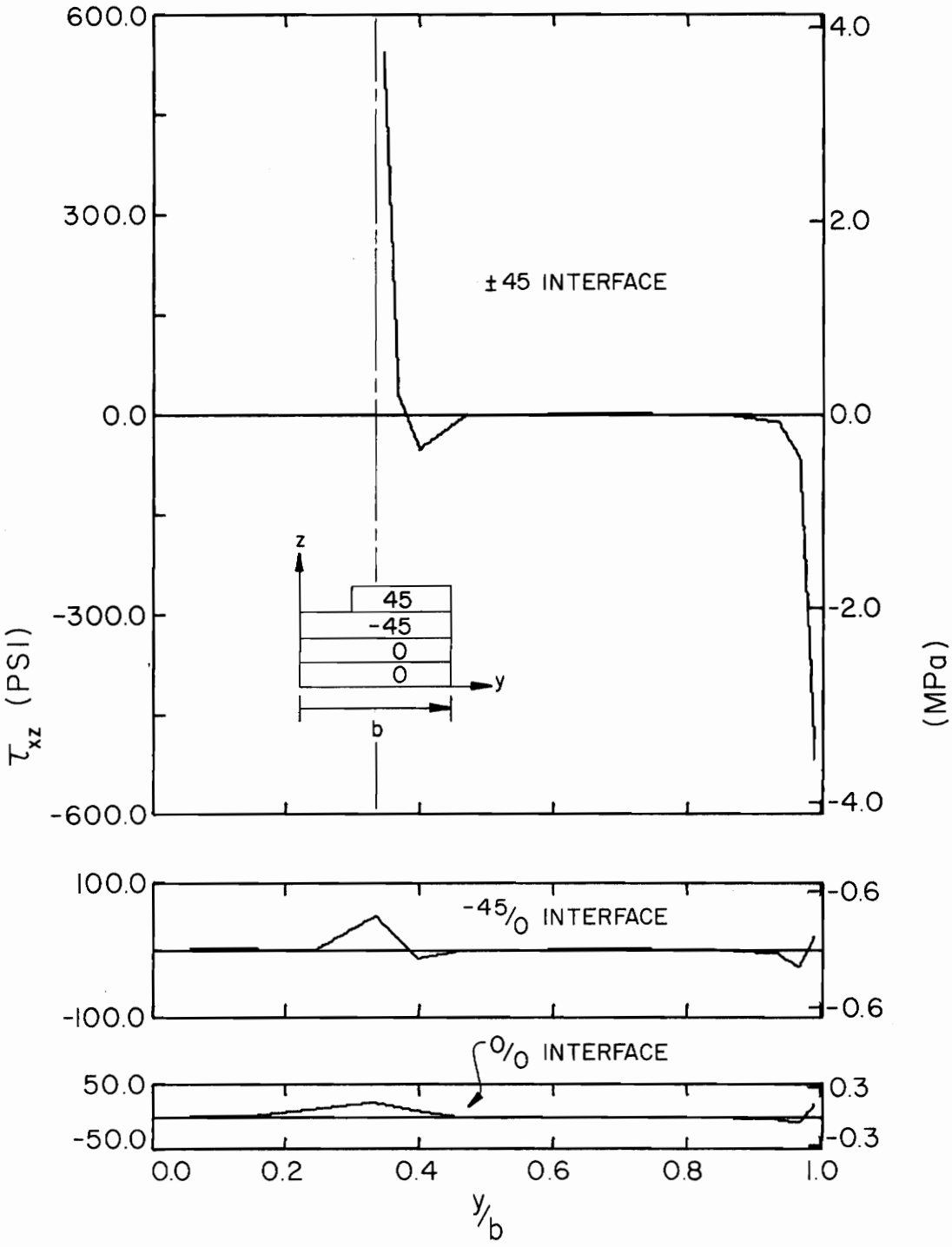

Figure 31. τ_{xz} along the Interfaces of $[\pm 45/0_2]_s$ Laminate with One Layer Cutout (ξ_x=-0.1%).

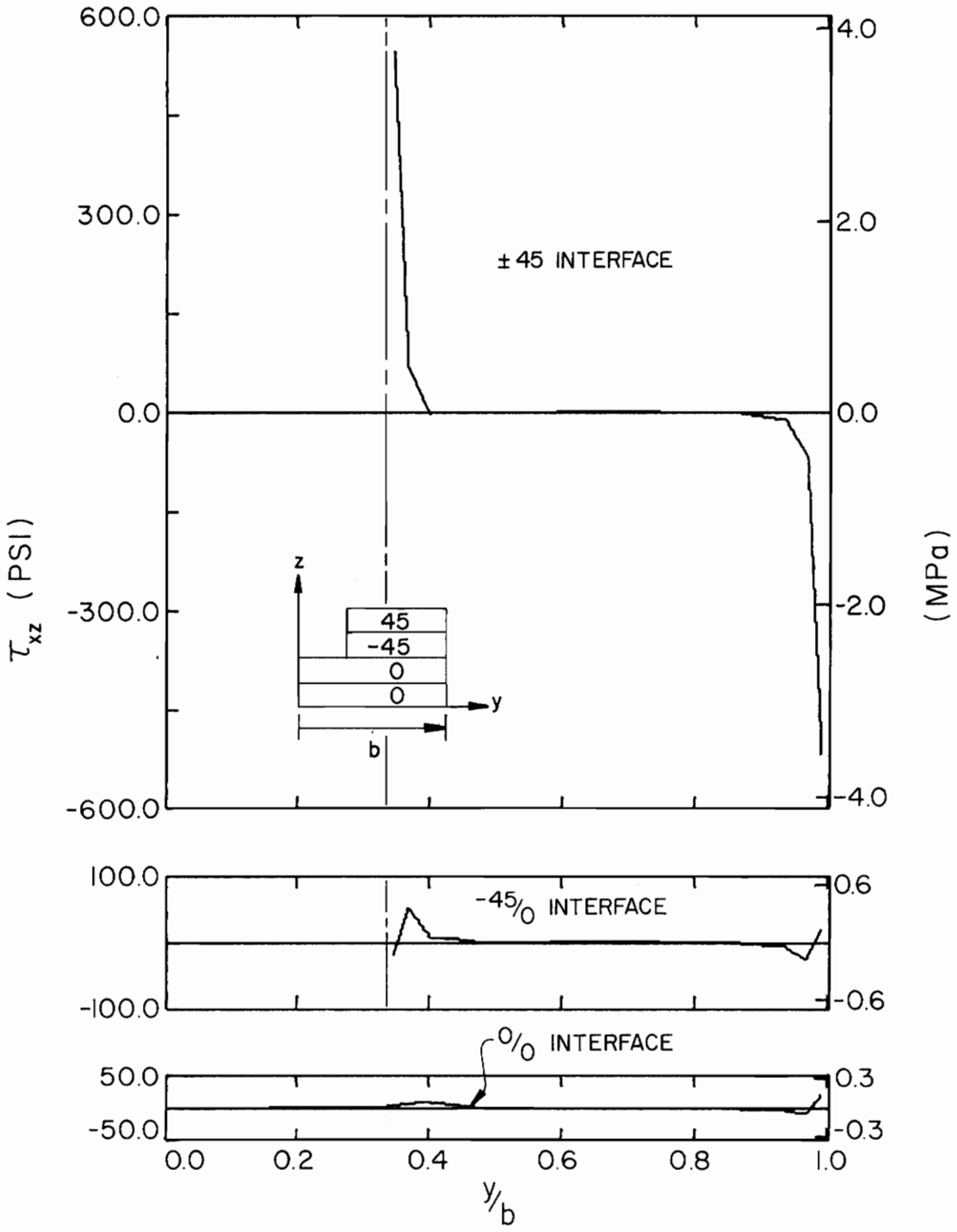

Figure 32. τ_{xz} along the Interfaces of $[\pm 45/0_2]_s$ Laminate with Two Layer Cutout (ε_x=-0.1%).

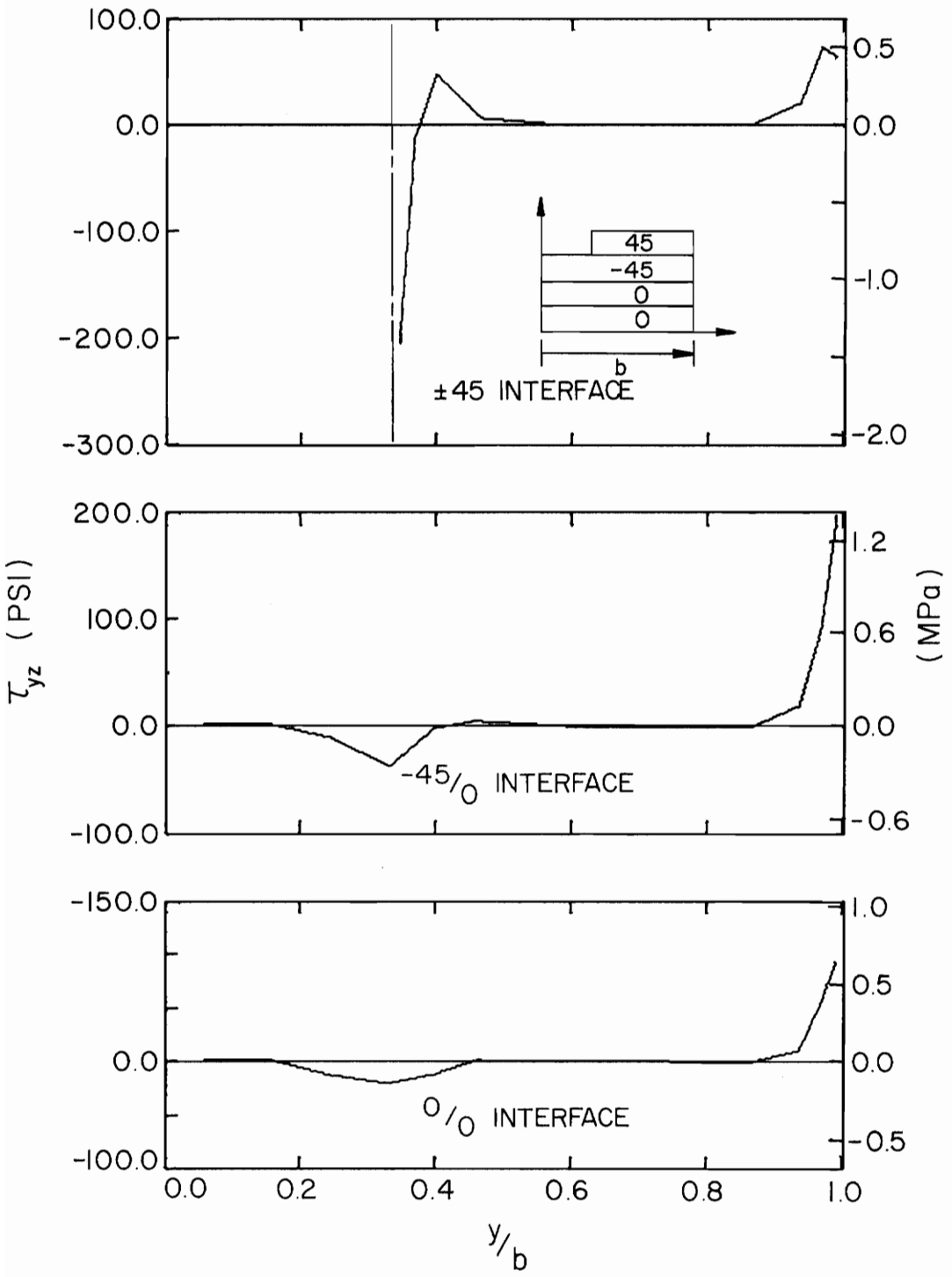

Figure 33. τ_{yz} along the Interfaces of $[\pm 45/0_2]_s$ Laminate with One Layer Cutout (ε_x=-0.1%).

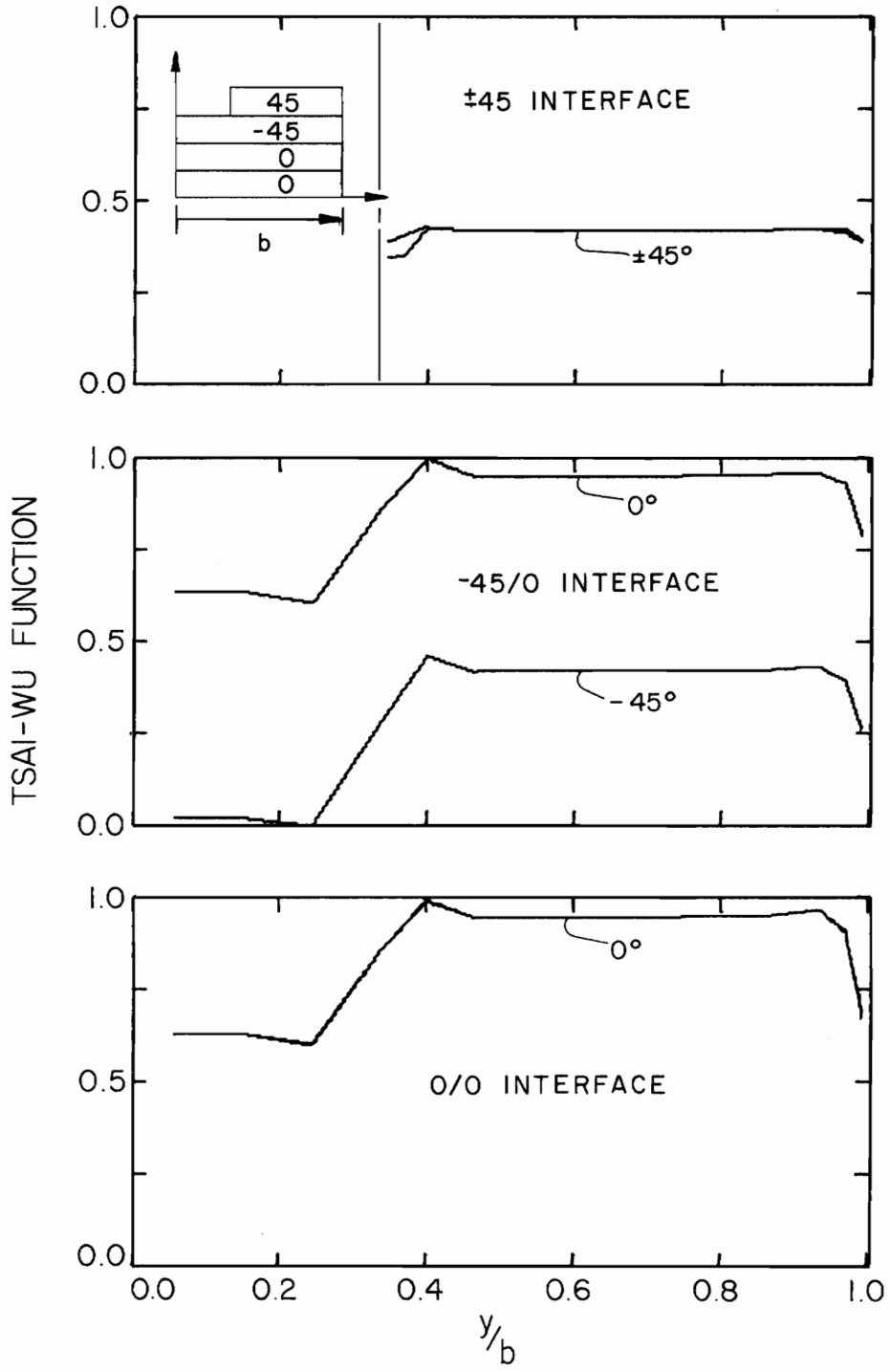

Figure 34. Distribution of Tsai-Wu Function along the Interfaces of $[\pm 45/0_2]_s$ Laminate with One Layer Cutout (ε_x=-0.1%).

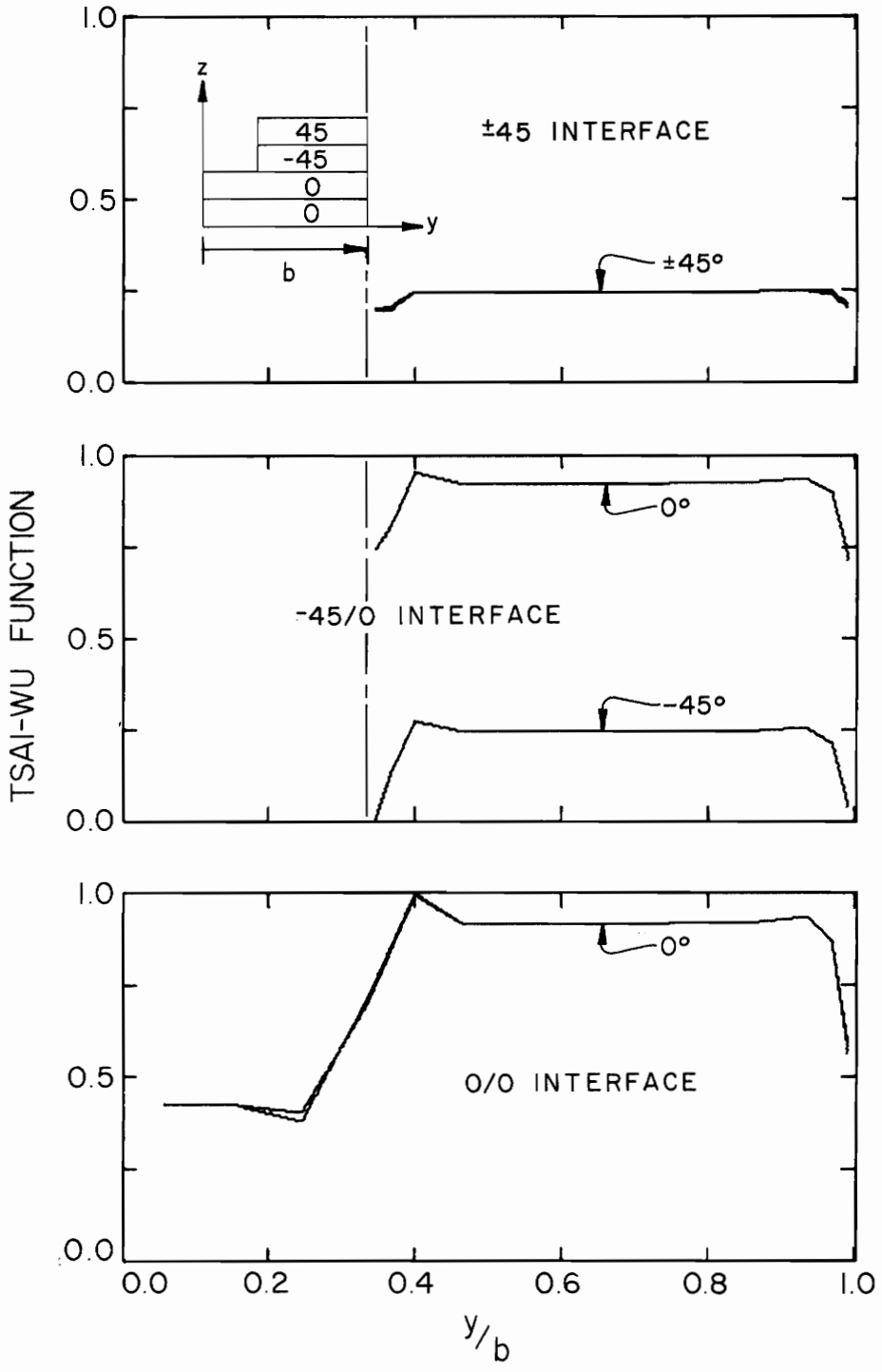

Figure 35. Distribution of Tsai-Wu Function along the Interfaces of $[\pm 45/0_2]_s$ Laminate with Two Layer Cutout (ε_x=-0.1%).

maximum σ_z stress (Figs. 30 and 31) and, when the terms of the Tsai-Wu function are examined, it is found that the σ_z stresses are the major contributing factor. Thus, failure may initiate at an internal point below the cutout and away from the free and cutout edges.

5.3.4 Quasi-Isotropic Laminates

The quasi-isotropic laminates studied were $[0/\pm45/90]_s$, $[90/\pm45/0]_s$ and $[\pm45/0/90]_s$, all eight layer laminates. The comments pertaining to interfaces and interior regions made in the introduction to Section 5.3.3 are, of course, valid for these special cases of eight layer cutouts (Figs. 22 and 23) were examined for all three laminates.

5.3.4.1 The $[0/\pm45/90]_s$ Laminate

The σ_x (Fig. 36), σ_y (Fig. 37) and τ_{xy} (Fig. 38) stress distributions for a laminate with a two layer cutout indicate that the cutout produces more severe stress concentrations when it is along the ±45 interface. In the +45 layer, and near the cutout, stress concentrations of 1.2 for σ_x, 1.34 for σ_y and 1.31 for τ_{xy} are present. As before, the interior region values are the lamination theory values for a $[0/\pm45/90]_s$ laminate. It should also be noted that the trends for σ_y and τ_{xy} at the free and cutout edges are consistent with the boundary conditions, as both stresses tend to zero near the edges. The dashed lines in the figures indicate the differences for a one layer cutout.

The σ_z, τ_{yz} and τ_{xz} interlaminar stress distributions for the two layer cutout are shown in Figs. 39, 40 and 41, respectively. The maximum positive σ_z occurs along the lower interface near the free

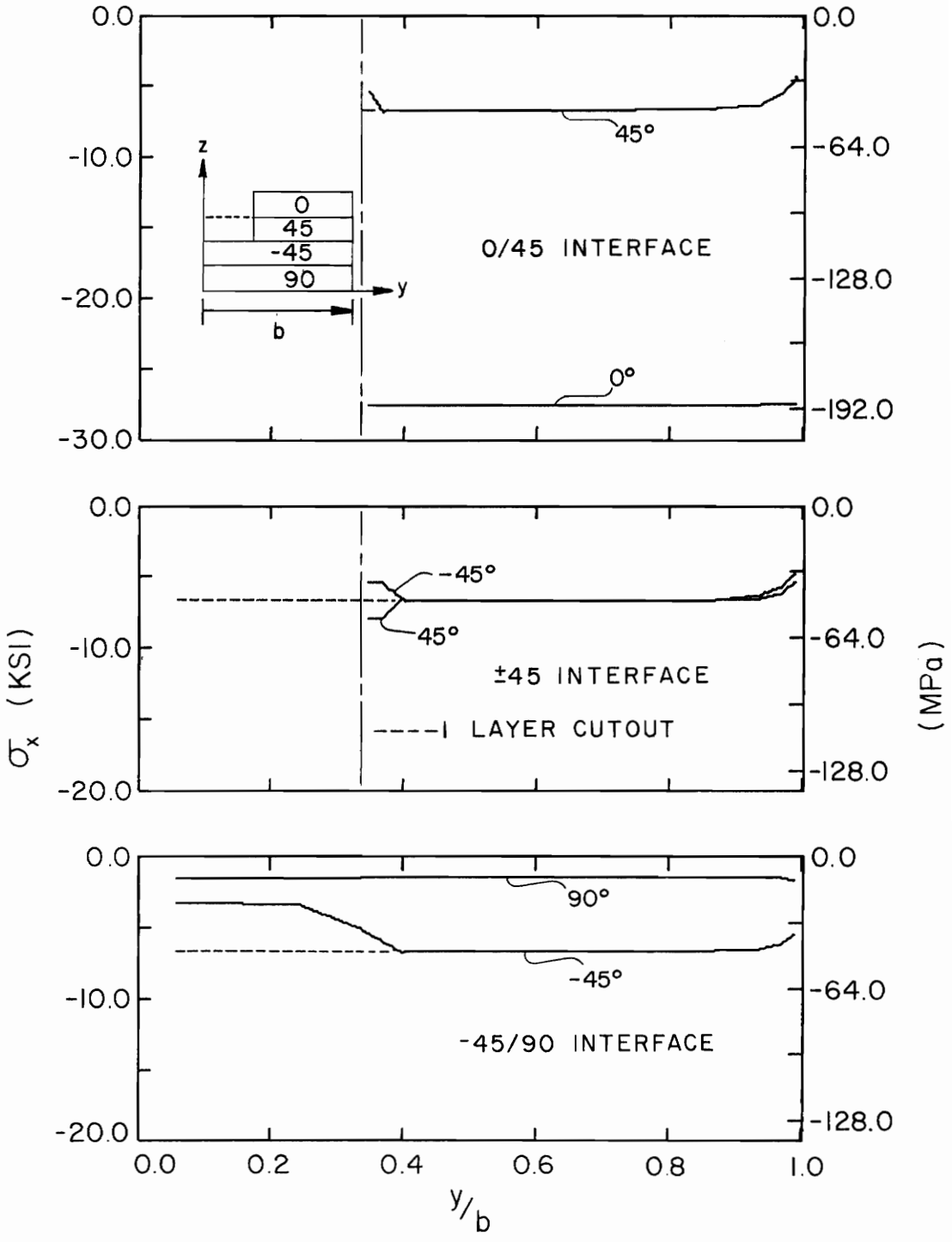

Figure 36. σ_x along the Interfaces of $[0/\pm45/90]_s$ Laminate with Two Layer Cutout (ε_x=-0.1%).

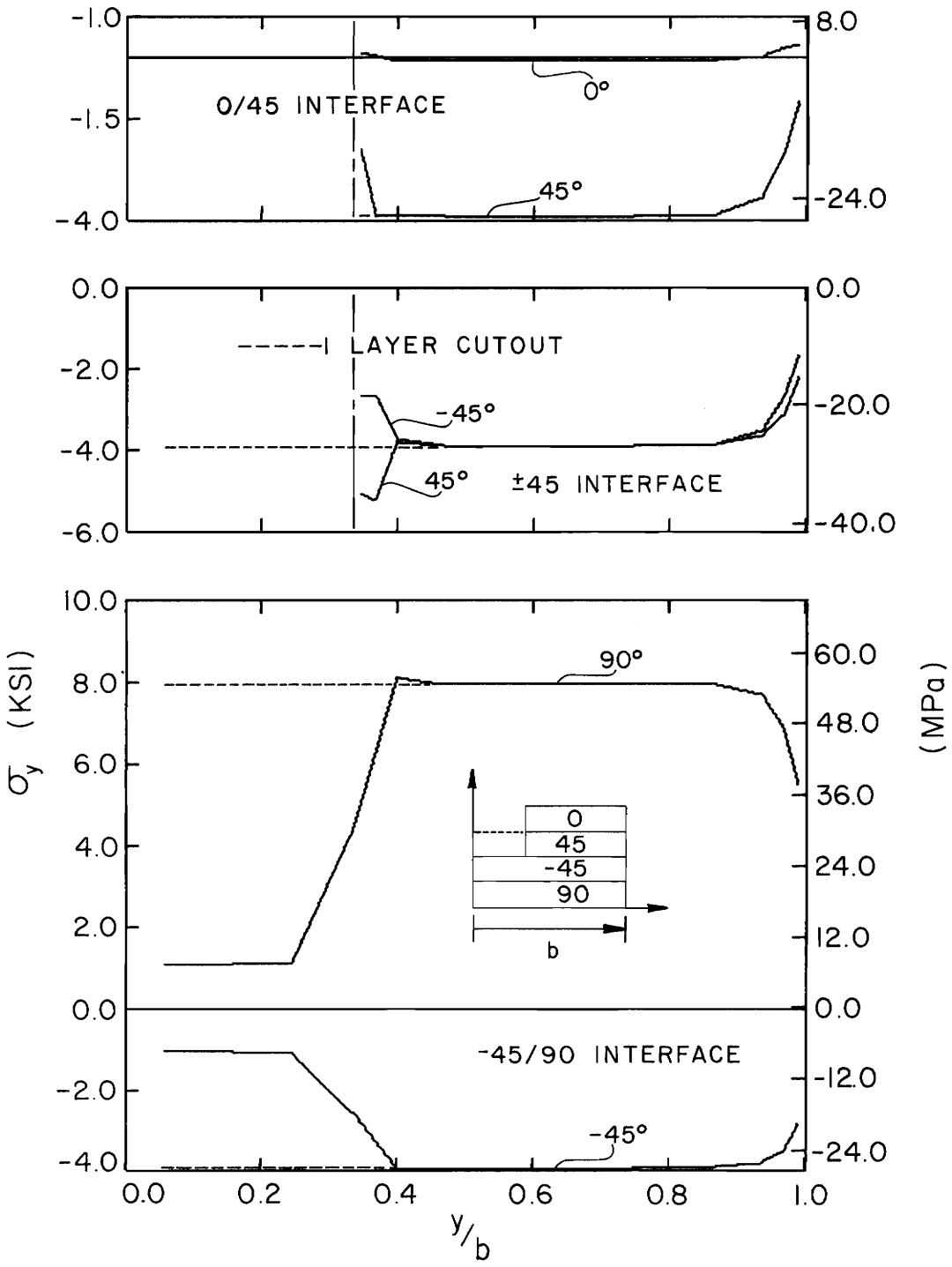

Figure 37. σ_y along the Interfaces of $[0/\pm45/90]_s$ Laminate with Two Layer Cutout (ε_x=-0.1%).

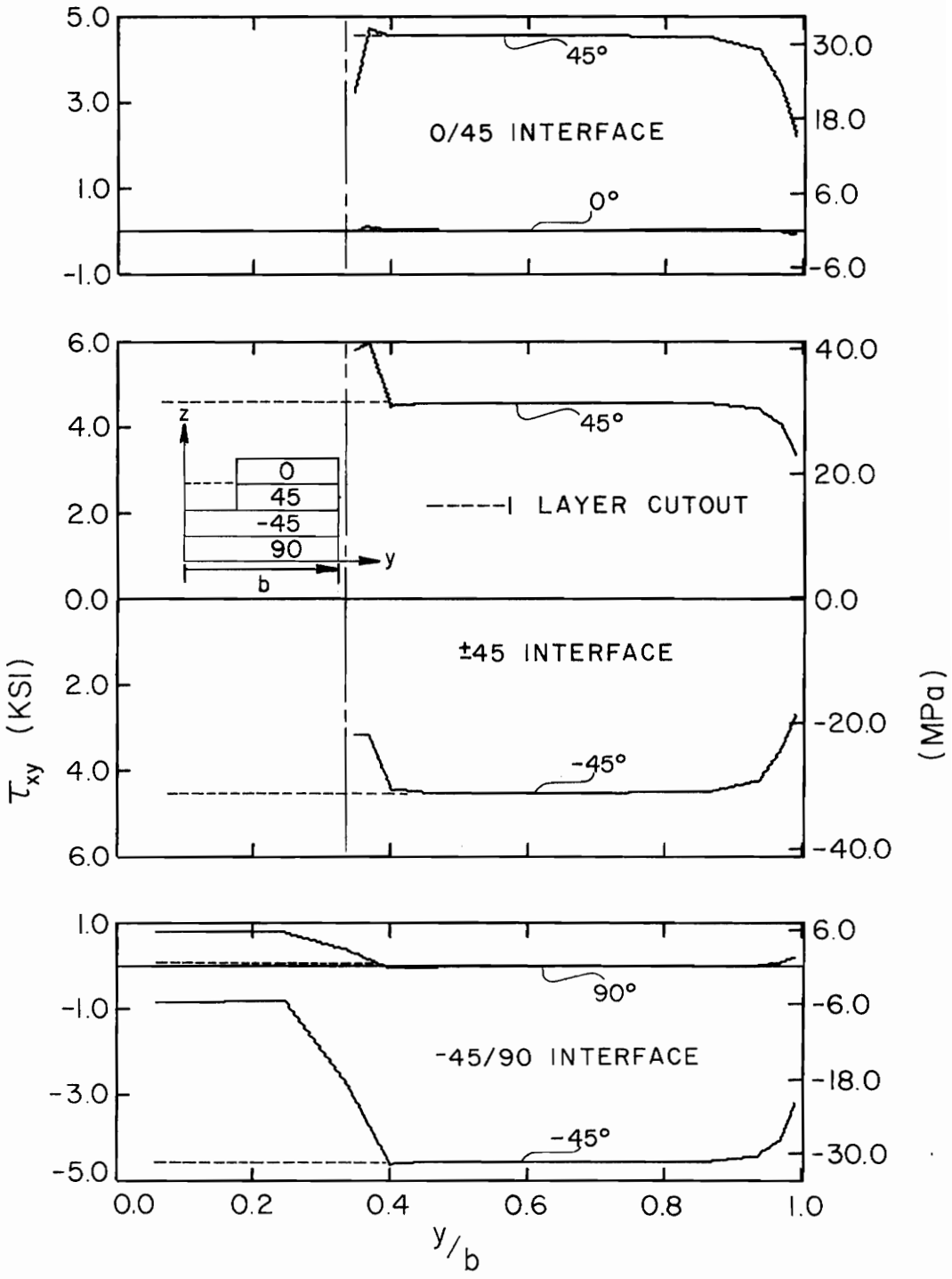

Figure 38. τ_{xy} along the Interfaces of $[0/\pm45/90]_s$ Laminate with Two Layer Cutout (ε_x=-0.1%).

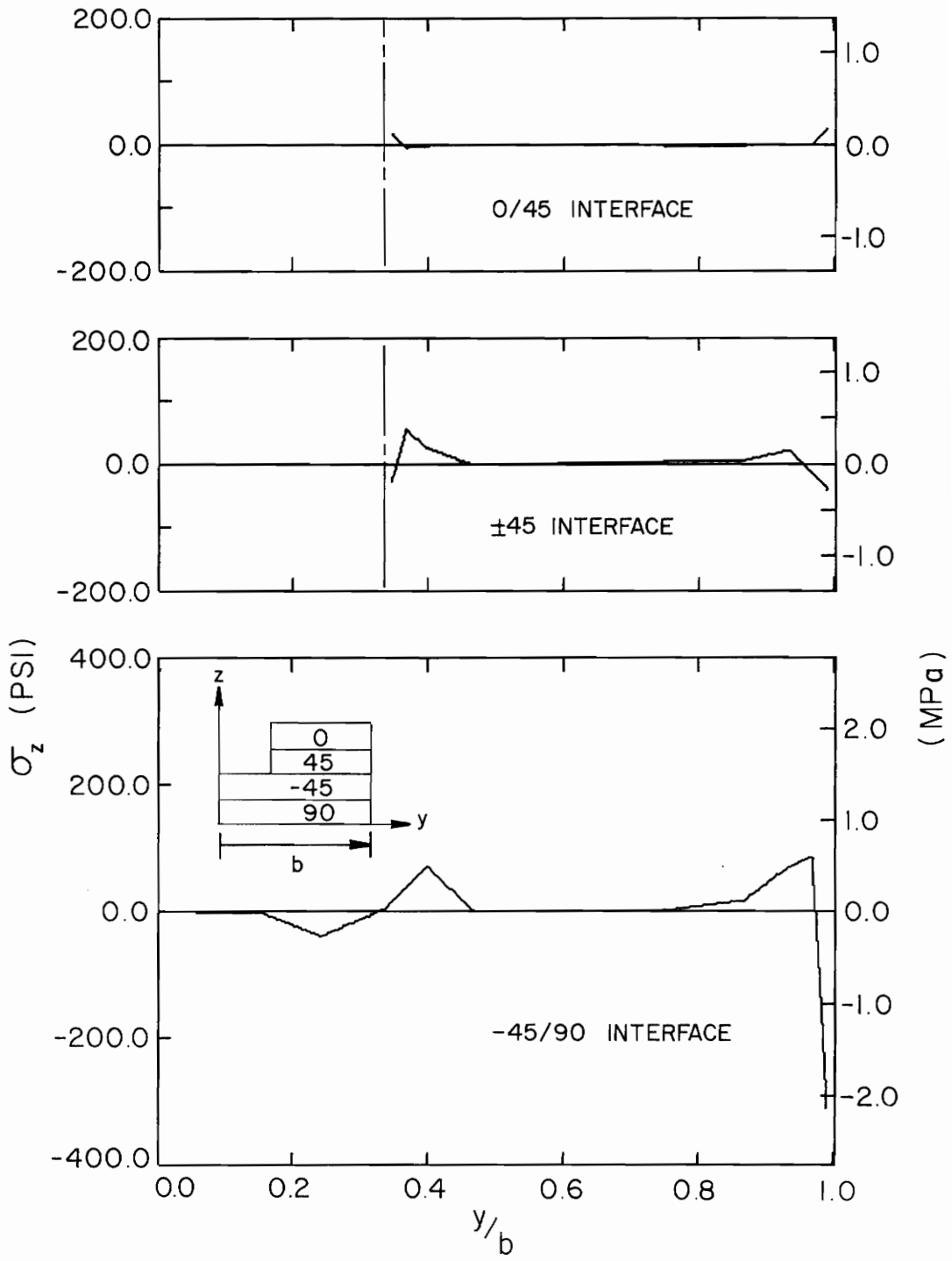

Figure 39. σ_z along the Interfaces of $[0/\pm45/90]_s$ Laminate with Two Layer Cutout (ε_x=-0.1%).

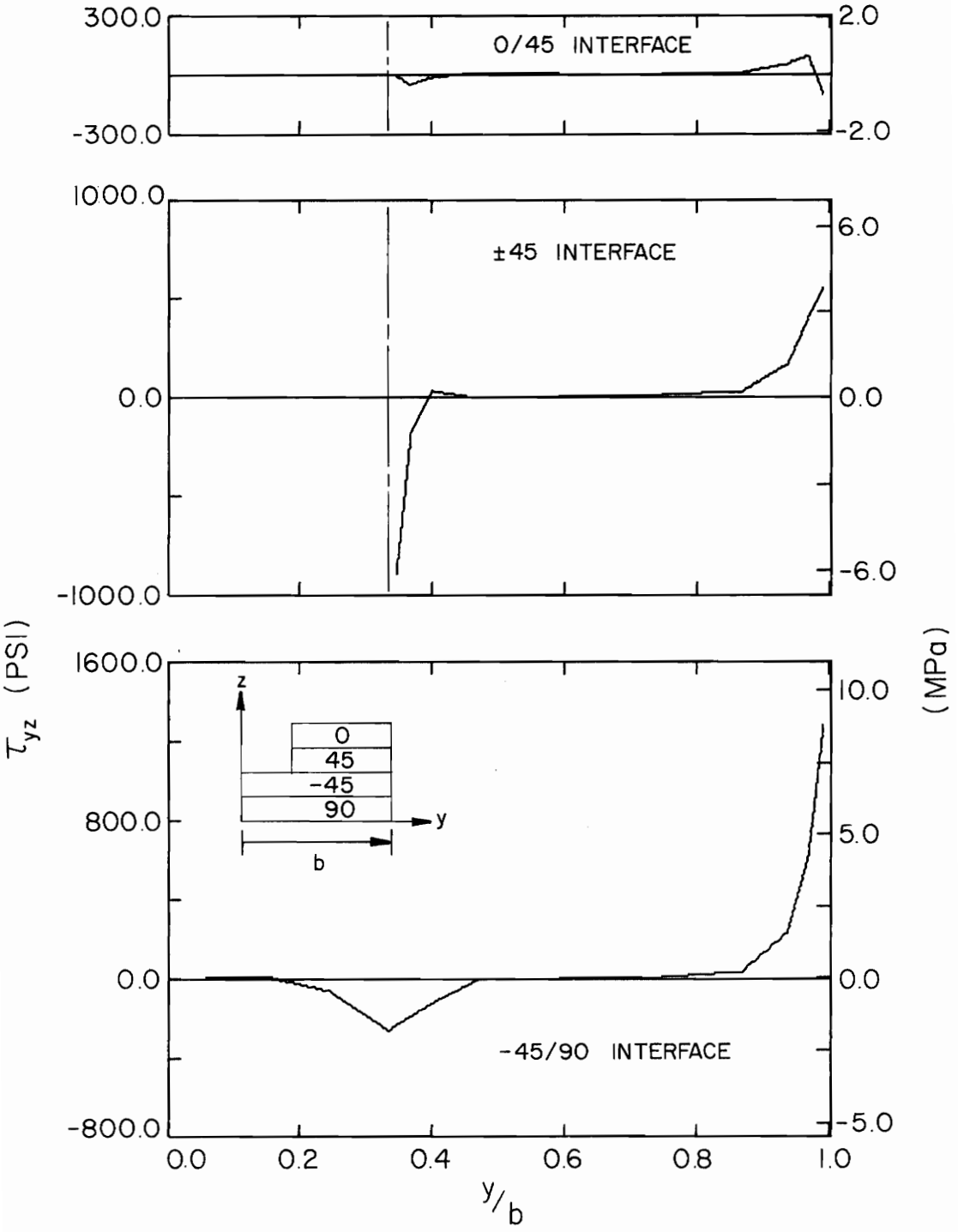

Figure 40. τ_{yz} along the Interfaces of $[0/\pm45/90]_s$ Laminate with Two Layer Cutout (ε_x=-0.1%).

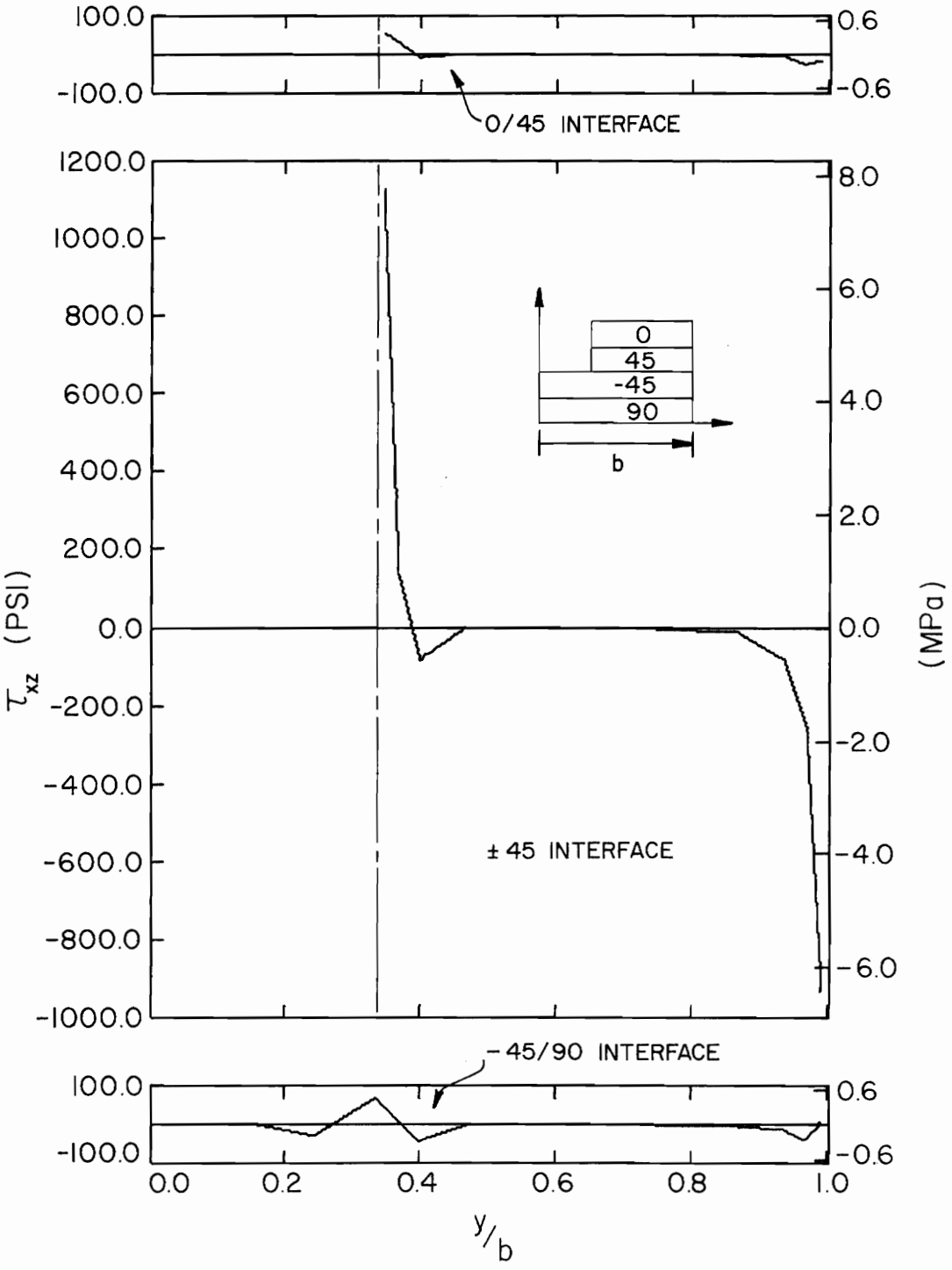

Figure 41. τ_{xz} along the Interfaces of $[0/\pm45/90]_s$ Laminate with Two Layer Cutout (ε_x=-0.1%).

edge, but the value below the cutout edge is nearly equal to this maximum value (Fig. 39). Equilibrium considerations can explain the double envelopes of the τ_{yz} and τ_{xz} distributions (Figs. 40 and 41) near the cutout as in the $[\pm 45]_s$ laminate (Section 5.3.2.2). For one layer cutout gradient distributions are not present near the cutout due to the coarseness of the mesh (see Section 5.2). Free edge stress distributions are the same, though, for one and two layer cutouts.

The distributions of the Tsai-Wu function along the interface of a laminate with a two layer cutout (Fig. 42) indicate that failure is predicted to occur in the 0° layer just above the 0/45 interface near the free edge. (The distributions for a one layer cutout are shown by the dashed lines.) Examination of the individual terms of the Tsai-Wu function indicates that no one stress component is the critical term. With the exception of σ_x, all stresses exhibit free edge values which contribute to the maximum Tsai-Wu value occurring in the 0° layer near the free edge.

5.3.4.2 The $[90/\pm 45/0]_s$ Laminate

The major difference in stress distributions between this stacking sequence and the $[0/\pm 45/90]_s$ laminate is shown by the σ_y distributions (Fig. 43) for a two layer cutout. Fig. 43, which is for the cutout along the ±45 interface, shows σ_y in the +45° layer tending to zero near the cutout. In contrast, Fig. 37 exhibits an increase in the magnitude of σ_y in the +45° layer near the cutout for the $[0/\pm 45/90]_s$ laminate. The interlaminar shear stress τ_{yz} is also affected by the stacking sequence, as evidenced by a comparison of the middle interface stress

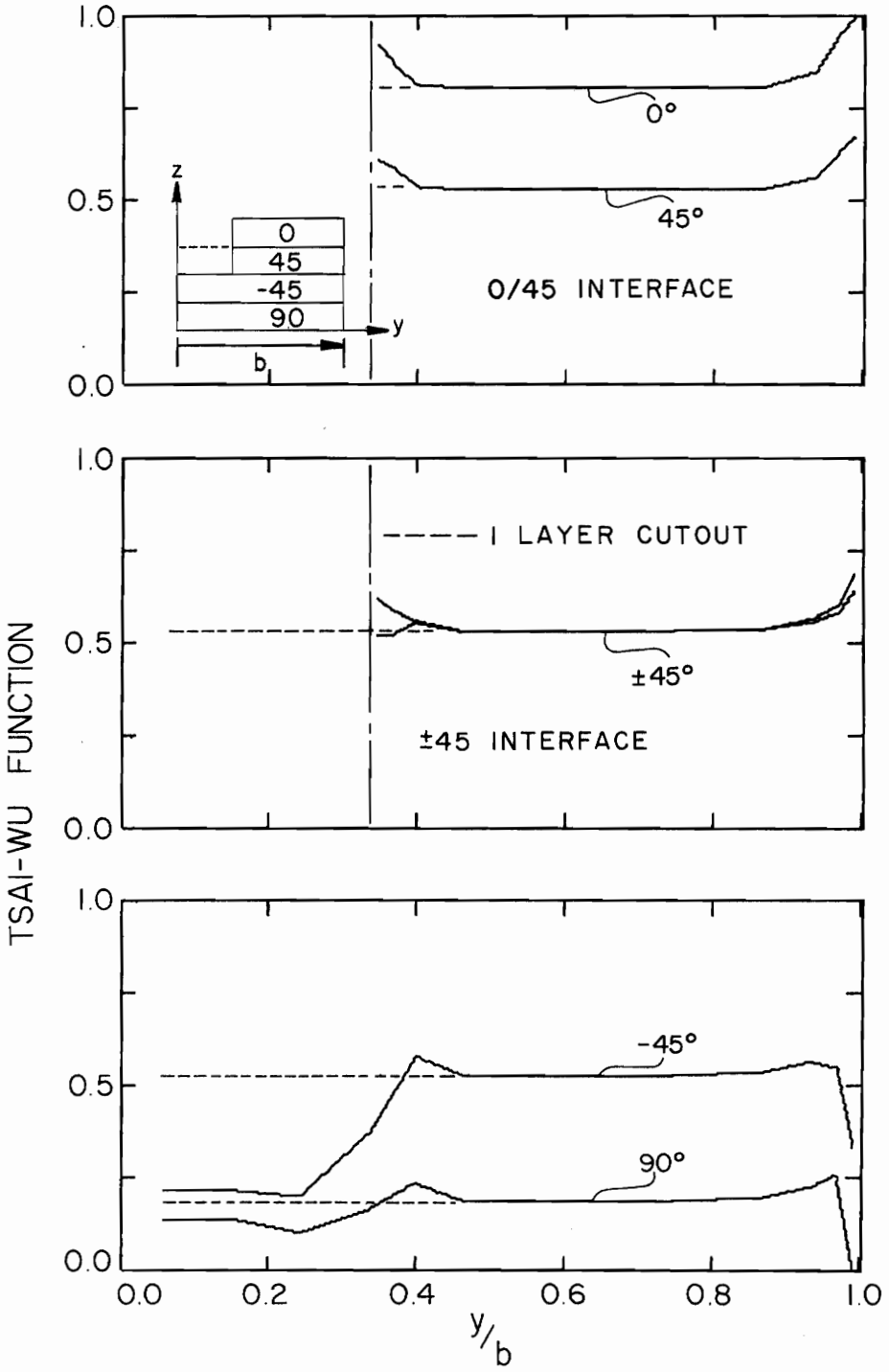

Figure 42. Distribution of Tsai-Wu Function along the Interfaces of $[0/\pm45/90]_s$ Laminate with Two Layer Cutout (ε_x=-0.1%).

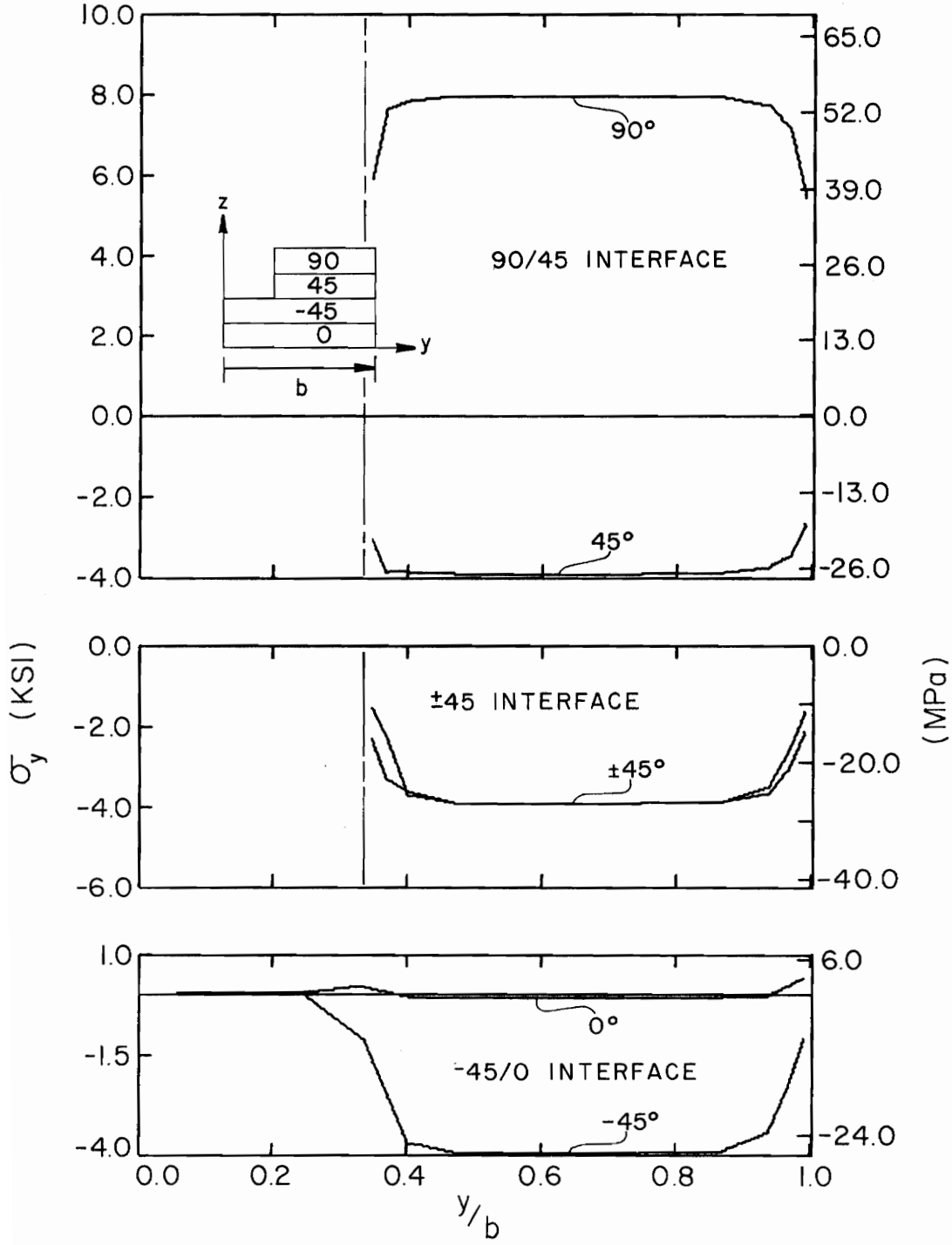

Figure 43. σ_y along the Interfaces of $[90/\pm45/0]_s$ Laminate with Two Layer Cutout (ε_x=-0.1%).

distributions of Figs. 40 and 44.

The σ_y stress distribution for a one layer cutout (Fig. 45) also shows a difference between this stacking sequence and the previous one. As indicated in Fig. 45, σ_y in the top (90°) layer increases 120 percent above the interior region value. This is in contrast to Fig. 37, which does not show this large increase for the $[0/\pm45/90]_s$ laminate. However, the corresponding interlaminar stress τ_{yz} (not shown) for a $[90/\pm45/0]_s$ laminate is not affected significantly by this increase. The τ_{yz} distribution for the upper interface does not exhibit a double envelope near the cutout edge, but rather a distribution similar to that near the free edge.

Although not shown in the figures, the τ_{xy} stress distributions for a [90/±45/0] laminate with a one or two layer cutout follow the same pattern as the σ_y distribution shown in Fig. 44. The interlaminar shear component τ_{xz} (Fig. 46) is affected in the same manner as was the τ_{yz} component. The double envelope near the cutout, seen in Fig. 41 along the middle interface, is not present in Fig. 46. Thus, the cutout does not act as a stress concentration for τ_{xy} and produces no unusual effects in the τ_{xz} distribution.

Fig. 47 presents results for the interlaminar normal stress σ_z for a laminate with a two layer cutout. In contrast to the results for a $[0/\pm45/90]_s$ laminate (Fig. 39), the σ_z stresses along the upper interface are large for the $[90/\pm45/0]_s$ laminate. Also, the σ_z stresses near the edges are positive for the $[90/\pm45/0]_s$ laminate and negative for the $[0/\pm45/90]_s$ laminate. Thus, the $[90/\pm45/0]_s$ laminate

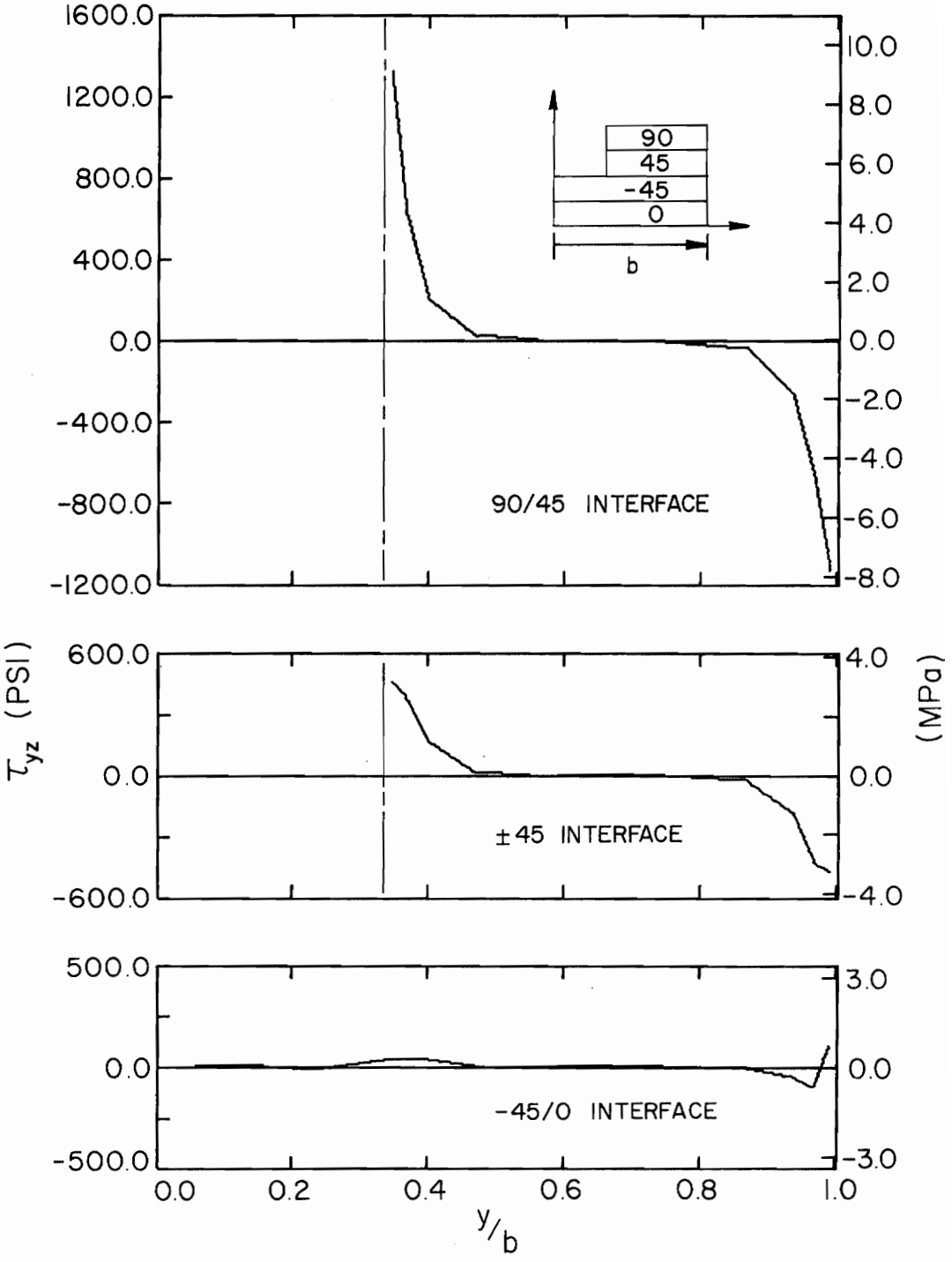

Figure 44. τ_{yz} along the Interfaces of $[90/\pm45/0]_s$ Laminate with Two Layer Cutout (ε_x=-0.1%).

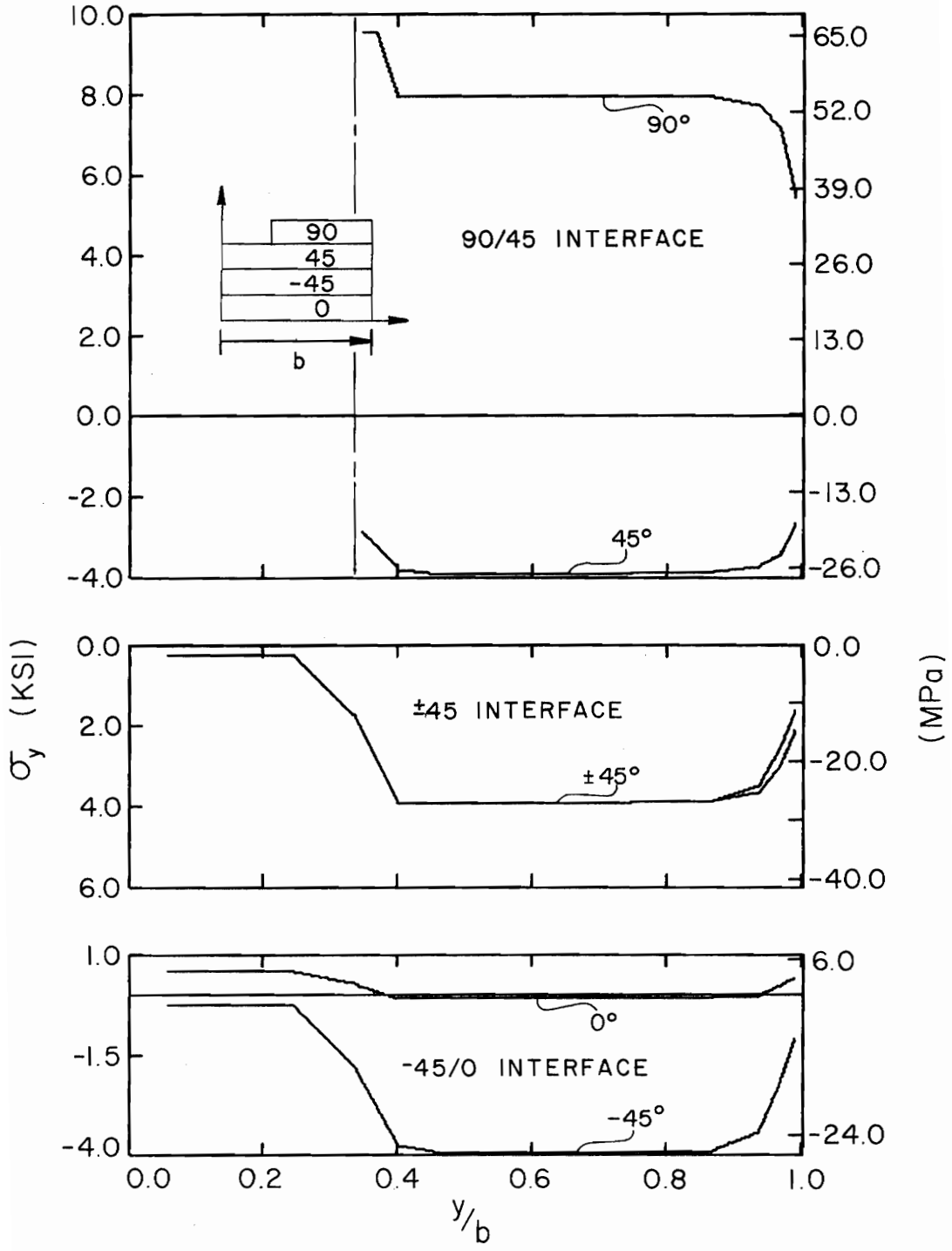

Figure 45. σ_y along the Interfaces of $[90/\pm45/0]_s$ Laminate with One Layer Cutout (ε_x=-0.1%).

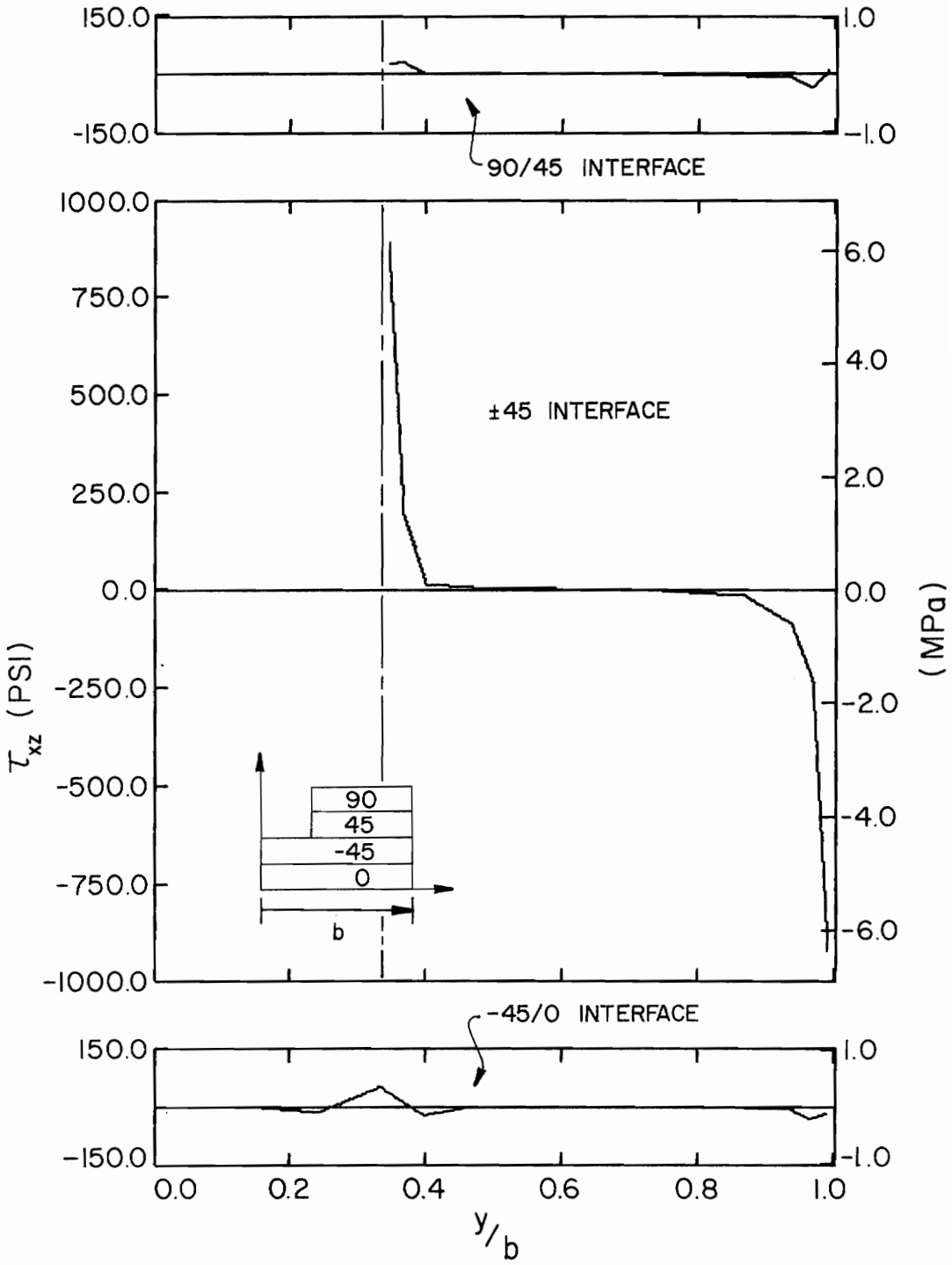

Figure 46. τ_{xz} along the Interfaces of $[90/\pm45/0]_s$ Laminate with Two Layer Cutout (ε_x=-0.1%).

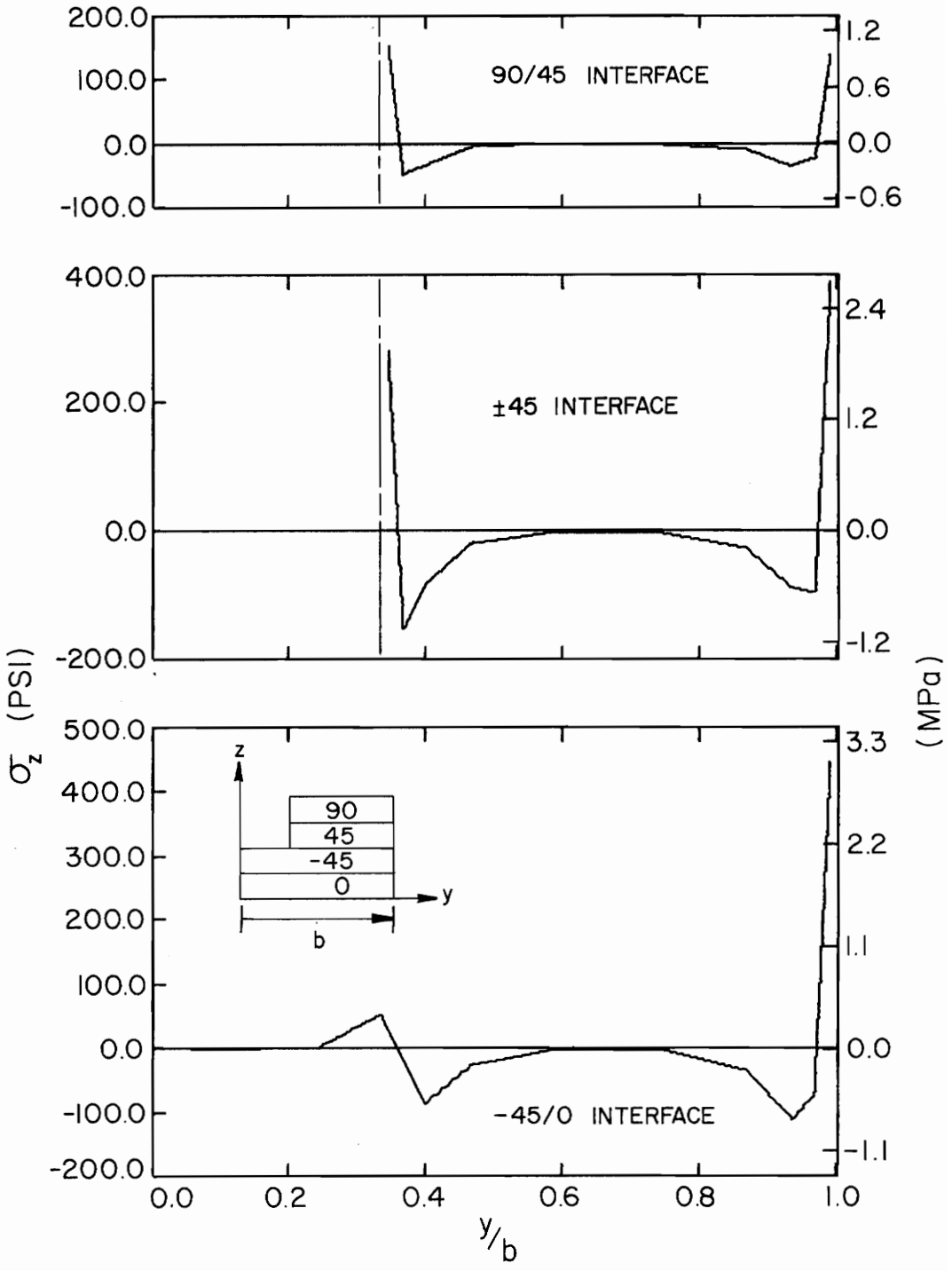

Figure 47. σ_z along the Interfaces of $[90/\pm45/0]_s$ Laminate with Two Layer Cutout (ε_x=-0.1%).

is more susceptible to the delamination mode of failure at the edges.

The distributions of the Tsai-Wu function for the $[90/\pm45/0]_s$ laminate with one and two layer cutouts (Figs. 48 and 49, respectively) indicate that failure is predicted to initiate near the free edge in the 0° layer. However, it should be noted that high values of the Tsai-Wu function are also present below the cutout in the 0° layer of the laminate with a one layer cutout (Fig. 48) and near the cutout in the +45° layer for the two layer cutout (Fig. 49). Thus failure could initiate at the free edge in the 0° layer and, at a higher strain level, in either of the two regions near the cutout where high values of the Tsai-Wu function occur. The nonlinear results to be discussed in Section 5.4.2 show this behavior.

5.3.4.3 The $[\pm45/0/90]_s$ Laminate

The $[\pm45/0/90]_s$ laminate provides little new insight. Like the other two quasi-isotropic laminates, the σ_y distributions for a two layer cutout (Fig. 50) show σ_y approaching the zero boundary value rapidly near an edge. Although not shown, a similar trend occurs in the τ_{xy} distribution. However, when the bottom of the cutout is along the ±45 interface (a one layer cutout) σ_y and τ_{xy} exhibit stress concentration factors of 1.27 and 1.26, respectively, near the cutout and in the +45° layer. As before, these stresses induce a double envelope near the cutout for the τ_{yz} and τ_{xz} distributions along the upper interface (also not shown).

5.4 Inelastic Results

The $[90/\pm45/0]_s$ laminate, with and without cutouts, was studied for

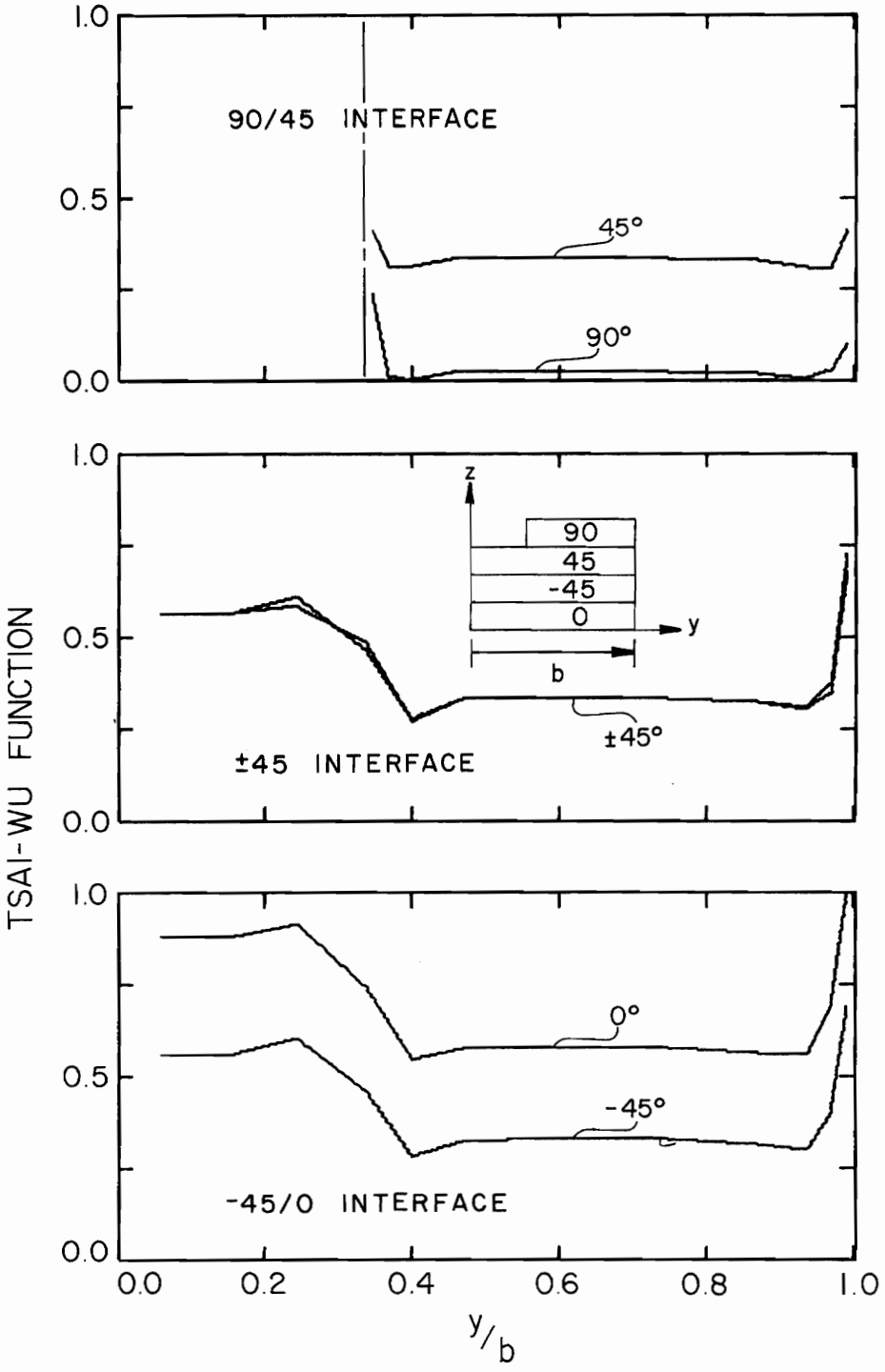

Figure 48. Distribution of Tsai-Wu Function along the Interfaces of $[90/\pm45/0]_s$ Laminate with One Layer Cutout (ε_x=-0.1%).

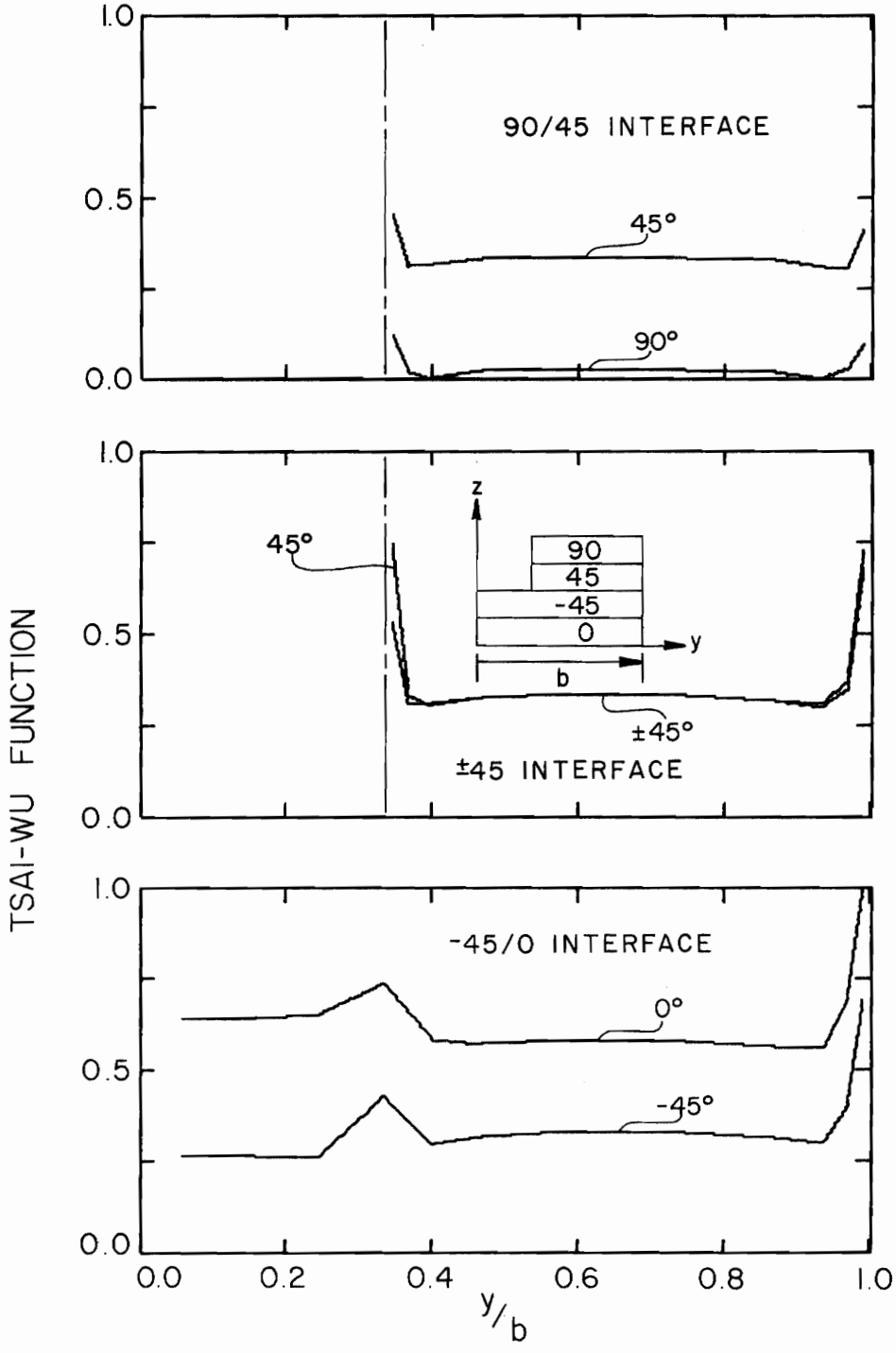

Figure 49. Distribution of Tsai-Wu Function along the Interfaces of $[90/\pm45/0]_s$ Laminate with Two Layer Cutout (ε_x=-0.1%).

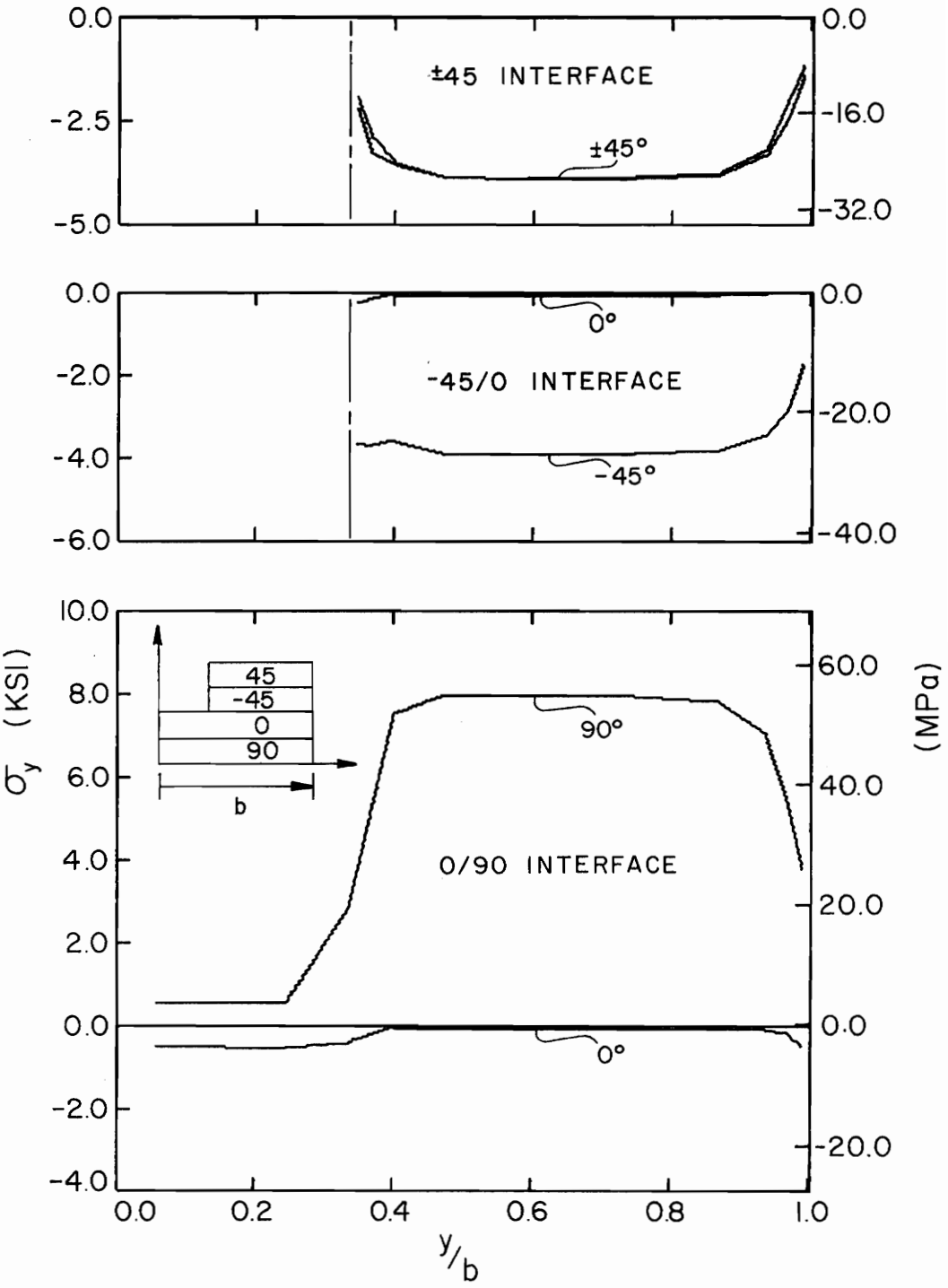

Figure 50. σ_y along the Interfaces of $[\pm 45/0/90]_s$ Laminate with Two Layer Cutout (ε_x=-0.1%).

inelastic behavior. The axial compressive strain was applied incrementally to failure in increments $\Delta \bar{\varepsilon}_x$ = -0.05 percent strain. Failure for the laminate was defined as the failure of all elements using the Tsai-Wu criterion for individual elements (Section 3.3.2). In the case of the one layer cutout, the stiffness matrix became unstable and the solution procedure failed. However, since the load had already dropped appreciably, this was taken as an indication of total failure.

5.4.1 Average Stress-Strain Results

The stress-strain behavior up to the first large decrease in stress is shown for all three laminate configurations in Fig. 51, where $\bar{\sigma}_x$ is the average compressive stress over the entire cross-section. As Fig. 51 indicates, the laminate modulus $\bar{E}_{11}$ is approximately the same for the one layer cutout and the complete laminate, but is higher for the two layer cutout. This is due to the higher volume fraction of 0° material in the laminate with the two layer cutout. Prior to failure, the modulus of each curve falls off slightly. In each case, this reduction in modulus corresponds to the failure of one or more large elements in the 0° layer in the interior of the laminate away from the edges.

The total stress-strain curves are shown in Fig. 52. Though the maximum $\bar{\sigma}_x$ stress differs the maximum load (in units of force) for both one and two layer cutouts is 60 percent of the maximum load for the complete laminate. Also, for $\bar{\varepsilon}_x$ between 0 and -1.4 percent, the various reductions in $\bar{\sigma}_x$ correspond mainly to failure of elements in the 0° layer. In all cases the 0° layer failed before the other layers failed.

In the case of the one layer cutout, the elements with nodes along

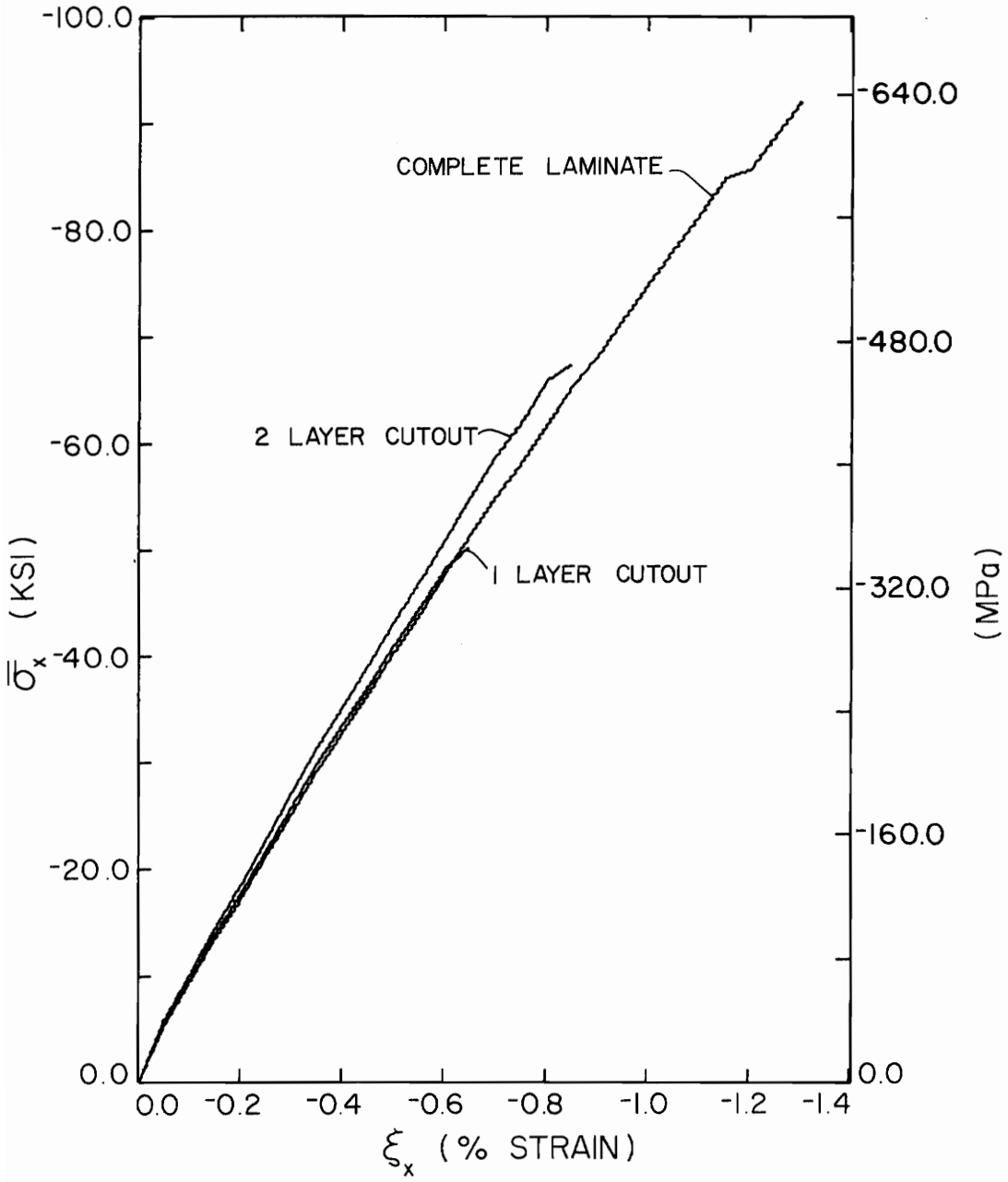

Figure 51. Partial Stress-Strain Curves for $[90/\pm45/0]_s$ Laminate.

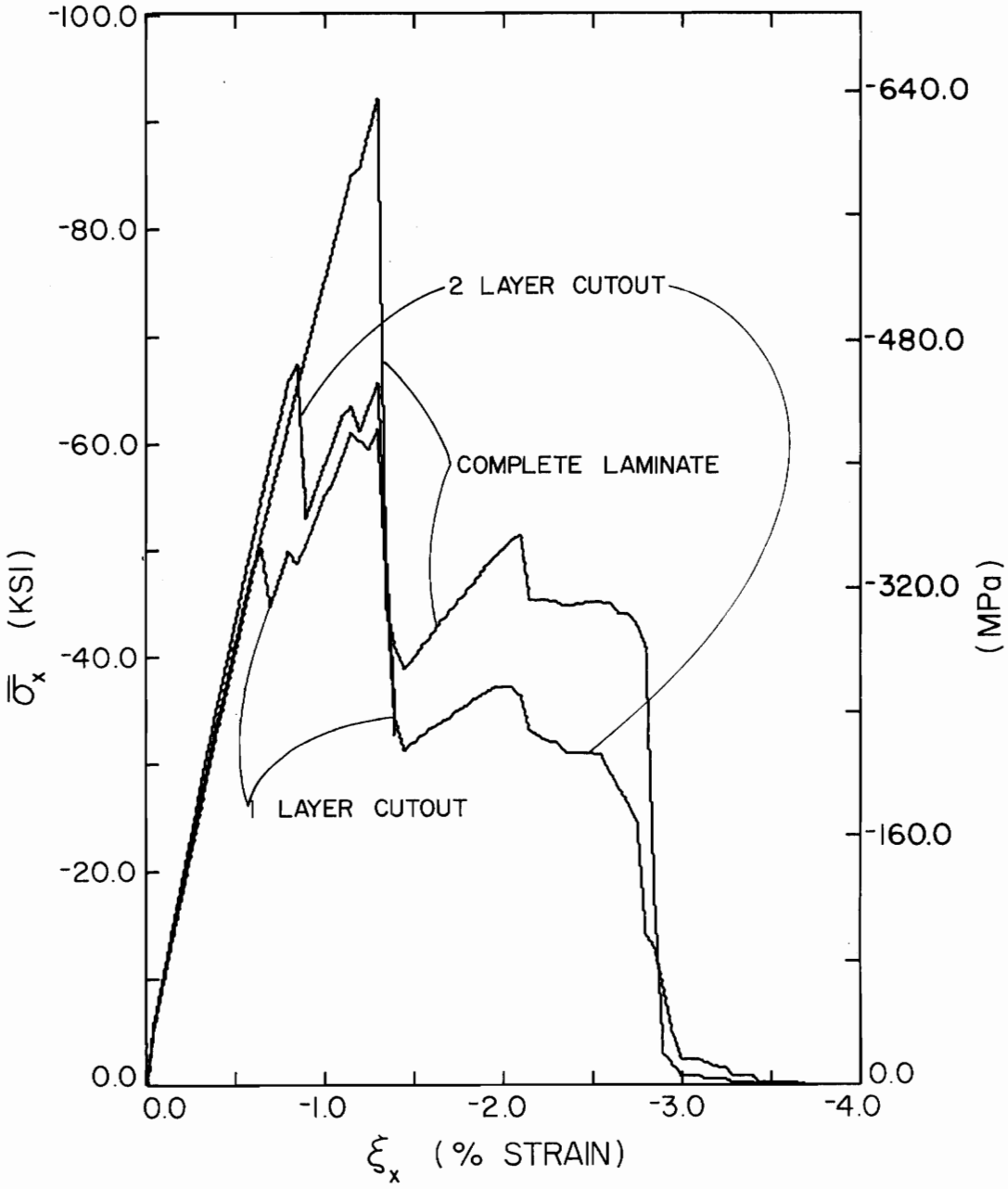

Figure 52. Total Stress-Strain Curves for $[90/\pm45/0]_S$ Laminate.

the centerline failed at ε_x = -1.4 percent. Since boundary conditions are applied along the centerline and midplane, this results in an unstable stiffness matrix. In the cases of the two layer cutout and the complete laminate, the elements with nodes along the centerline failed at ε_x between -1.4 and -4.0 percent when only a few isolated elements remained. Thus, no unstable matrix resulted.

5.4.2 Failure Progression

In all three cases, the free edge in the 0° layer was the first region to fail. As the strain level was increased, elements in the ±45° layers near the free edge failed. At the strain level ε_x = -0.4 percent, several elements in the 0° layer near the centerline failed and, as the strain level was increased further, elements between the free edge and centerline in the 0° layer failed. Finally, with the 0° layer failed and elements at the edges in other layers failed, the laminates were essentially failed.

In the region near the cutout there was a significant difference in the order in which elements failed, depending on whether the cutout was one or two layers. For the two layer cutout, elements failed along the cutout edge in the +45° layer and then the 90° layer. The pattern was similar for the one layer cutout but progressive failure also occurred in the +45° layer around the cutout. First, elements near the cutout failed and then, as the strain level increased, more and more elements around the cutout failed.

5.4.3 Failure Prediction

The first failure of the laminate with a two layer cutout occurred at ξ_x = -0.4 percent. The distributions of the Tsai-Wu function for ξ_x = -0.35 percent for both one and two layer cutouts are shown in Figs. 53 and 54. These distributions are similar to the elastic results presented in Figs. 48 and 49, where ξ_x = -0.1 percent. Thus, the elastic results for a single increment give excellent predictions of where failure will occur. Both Figs. 53 and 54 indicate fialure will initiate in the 0° layer near the free edge for all three laminate configurations. This is as expected since the free edge stress distributions are the same with or without cutouts. Initial failure actually occurred in this region on the next increment (ξ_x = -0.4 percent).

Results for a one layer cutout (Fig. 53) show high values of the Tsai-Wu function below the cutout in the 0°, +45° and -45° layers while the results for the two layer cutout (Fig. 54) show high Tsai-Wu values near the cutout in the +45 layer only. In both cases, subsequent failure occurs in these regions at higher strain levels.

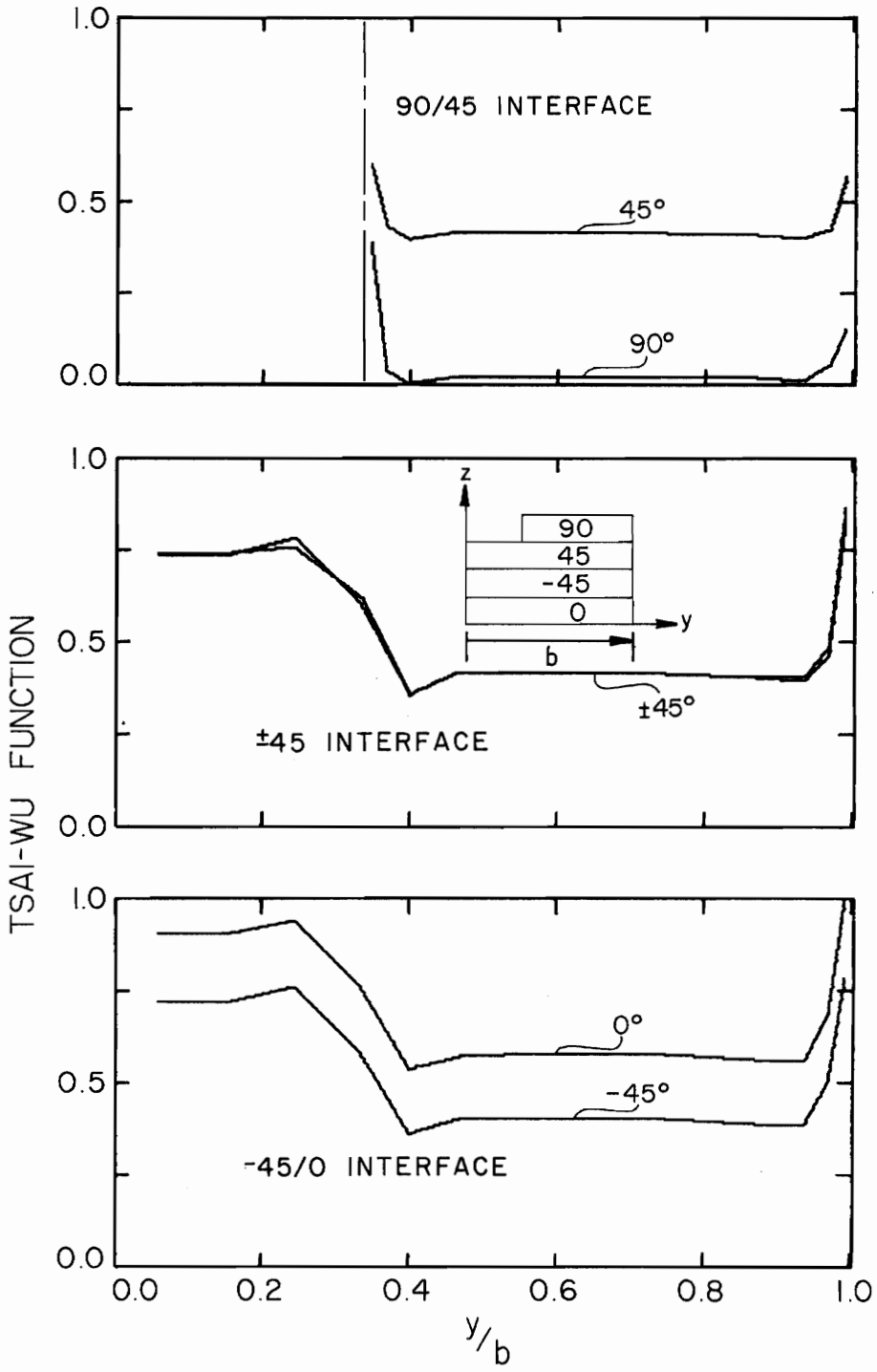

Figure 53. Distribution of Tsai-Wu Function along the Interfaces of $[90/\pm45/0]_s$ Laminate with One Layer Cutout (ε_x=-0.35%).

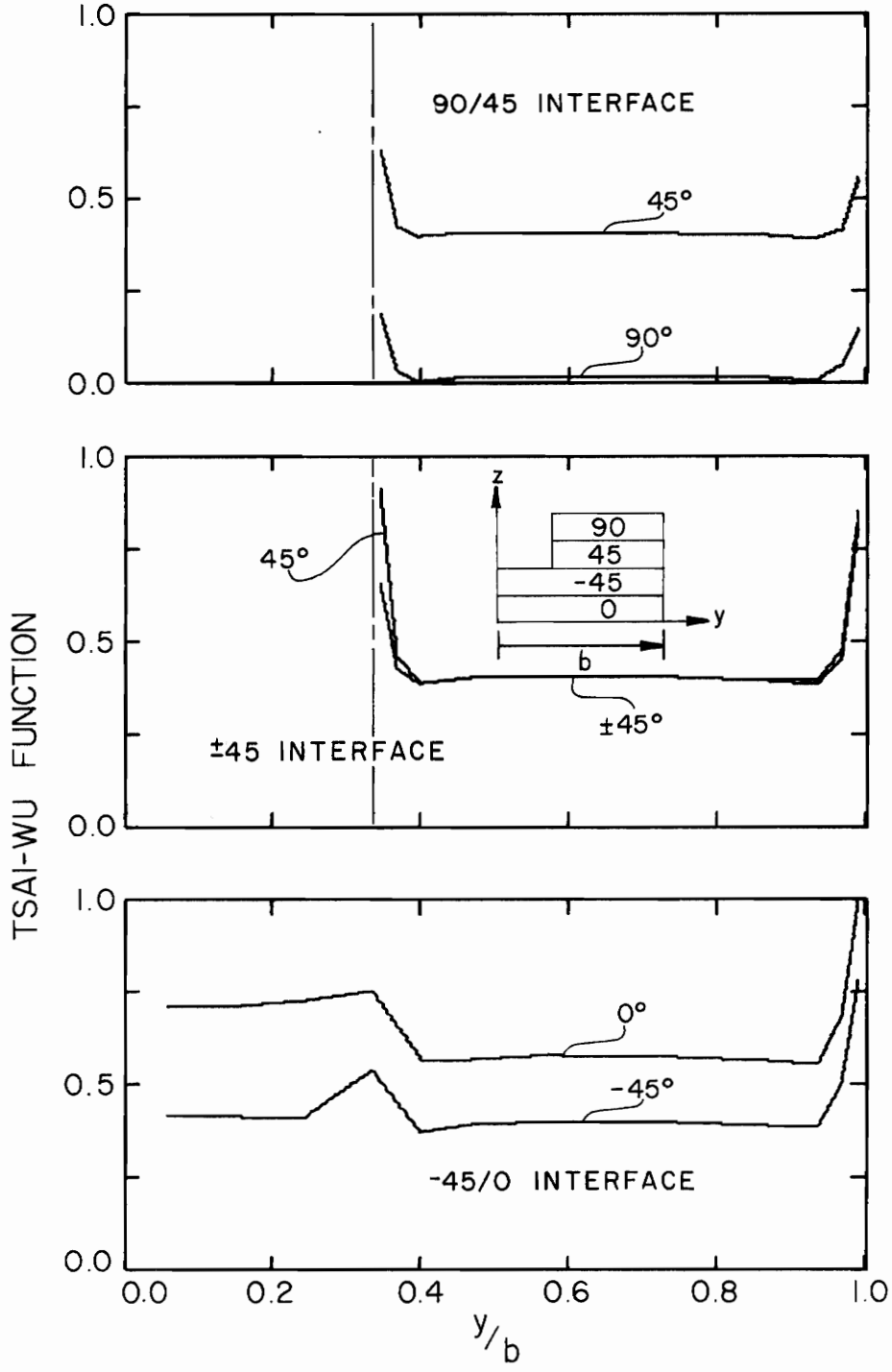

Figure 54. Distribution of Tsai-Wu Function along the Interfaces of $[90/\pm45/0]_s$ Laminate with Two Layer Cutout (ε_x=-0.35%).

Chapter 6

CONCLUSIONS

This study was concerned with linear and nonlinear stress and failure analysis of an idealized damage zone in a laminated composite under compressive loading. The following conclusions can be made from results of the analysis.

1. A boundary layer exists around the damage zone; it is similar to the boundary layer along the free edges.
2. Interlaminar stresses in the boundary layer around the damage zone are similar to those produced at the free edge.
3. The interlaminar stresses around the damage zone may be as large or larger than those at the free edge depending upon the fiber orientations and stacking sequence.
4. The boundary layer associated with the damage zone extends as far or farther into the interior of the laminate as does the free edge effect, depending on fiber orientation and stacking sequence.
5. Only laminated materials with more than one fiber orientation are affected by the damage zone.
6. Lamination theory is valid in interior regions away from free edges and the damage zone.
7. The presence of a damaged zone induces interlaminar stresses in an interior region away from free edges and the damage zone.

8. Due to interlaminar stresses produced in an interior region, failure, defined by a Tsai-Wu failure criterion, may initiate in the interior away from free edges and the damage zone.
9. The cutout extending down to a ±45 interface may produce large stress concentrations near the edge of the damage zone, depending upon the fiber orientations and stacking sequence.
10. Elastic results adequately predict where failure initiates for the laminate considered.
11. A damaged $[90/\pm45/0]_s$ laminate fails at approximately 60 percent of the load carried by an undamaged laminate.
12. For a $[90/\pm45/0]_s$ laminate, initial failure occurs at the free edge in the 0° layer. Subsequent failure in the interior of the 0° layer as well as at the free and cutout edges of the other layers leads to total failure.

This investigation indicates that future areas of study should include:

1. Linear and nonlinear analysis of hygrothermal effects in laminates with idealized damage zones.
2. A three layer damage zone (cutout) in an eight layer laminate.
3. The effects of varying geometric parameters such as cutout width and layer thickness.

4. More detailed nonlinear analysis.
5. An improved method for modeling failure and unloading of an element.
6. Experimental study of specimens with idealized damage zones to compare with theoretical analysis.
7. Analysis capability for bending of unsymmetric laminates.

BIBLIOGRAPHY

1. Renieri, G. D., Herakovich, C. T., "Nonlinear Analysis of Laminated Fibrous Composites," VPI&SU Report VPI-E-76-10, June, 1976.

2. Herakovich, C. T., Renieri, G. D., Brinson, H. F., "Finite Element Analysis of Mechanical and Thermal Edge Effects in Composite Laminates," Composite Materials: The Influence of Mechanics of Failure on Design, Army Symposium on Solid Mechanics, Cape Cod, MA., Sept. 1976.

3. Humphreys, E. A., Herakovich, C. T., "Nonlinear Analysis of Bonded Joints with Thermal Effects," VPI&SU Report VPI-E-77-19, June, 1977.

4. Timoshenko, S. P., Woinowsky-Krieger, S., Theory of Plates and Shells, McGraw-Hill Book Co., Inc., New York, N.Y., 1959.

5. Timoshenko, S. P., Goodier, J. N., Theory of Elasticity, McGraw-Hill, Inc., New York, N.Y., 1970.

6. Roark, R. J., Young, W. C., Formulas for Stress and Strain, McGraw-Hill, Inc., New York, N.Y., 1975.

7. Peterson, R. E., Stress Concentration Factors, John Wiley and Sons, New York, N.Y., 1974.

8. Savin, G. N., Stress Concentrations around Holes, NASA Report TTF-607, 1970.

9. Rowlands, R. E., Daniel, I. M., Whiteside, J. B., "Geometric and Loading Effects on Strength of Composite Plates with Cutouts," Composite Materials: Testing and Design (Third Conference), ASTM STP 546, American Society for Testing and Materials, 1974, pp. 361-375.

10. Ashton, J. E., Burdorf, M. L., Olson, F., "Design, Analysis and Testing of an Advanced Composite F-111 Fuselage," Composite Materials: Testing and Design (Second Conference), ASTM STP 497, American Society for Testing and Materials, 1972, pp. 3-27.

11. Barker, R. M., Dana, J. R., Pryor, C. W., "Stress Concentrations near Holes in Laminates," Presented at the November 13-14, 1972 ASCE Specialty Conference on Composite Materials at Pittsburgh, Pa.

12. Hsu, P. W., Herakovich, C. T., "Interlaminar Stresses in Composite Laminates -- A Perturbation Analysis," VPI-E-76-1, January, 1976.

13. Pipes, R. B., Daniel, I. M., "Moire Analysis of the Interlaminar Shear Edge Effect in Laminated Composites," J. Comp. Mat., Vol. 5, 1971, pp. 225-259.

14. Pipes, R. B., Pagano, N. J., "Interlaminar Stresses in Composite Laminates under Uniform Axial Extension," J. Comp. Mat., Vol. 4, 1970, pp. 538-548.

15. Bergner, H. W., Davis, J. G., Herakovich, C. T., "Analysis of Shear Test Method for Composite Laminates," VPI-E-77-14, April, 1977.

16. Tsai, S. W., Wu, E. M., "A General Theory of Strength for Anisotropic Materials," J. Comp. Mat., Vol. 5, 1971, pp. 58-80.

17. Wu, E. M., "Optimal Experimental Measurements of Anisotropic Failure Tensors," J. Comp. Mat., Vol. 6, 1972, pp. 472-489.

18. Pipes, R. B., Cole, B. W., "On the Off-Axis Strength Test for Anisotropic Materials," J. Comp. Mat., Vol. 7, 1973, pp. 246.

19. Sandhu, R. S., "Nonlinear Behavior of Unidirectional and Angle-ply Laminates," J. Aircraft, Vol. 13, No. 2, 1976.

20. Wilson, E. L., Bathe, K., Doherty, W. P., "Direct Solution of Large Systems of Linear Equations," Computers and Structures, Vol. 4, 1974, pp. 363-372.

21. Bathe, K., Wilson, E. L., Numerical Methods in Finite Element Analysis, Prentice-Hall, Inc., Englewood Cliffs, N.J., 1976.

22. Hofer, K. E., Larsen, D., Humphreys, V. E., "Development of Engineering Data on the Mechanical and Physical Properties of Advanced Composite Materials," AFML-TR-74-266, IIT Research Institute, Chicago, Ill., 1975.

23. Kibler, K. G., Proceedings of "The Effects of Relative Humidity and Elevated Temperature on Composite Structures," pp. 190-211, Center for Composite Materials, Univ. of Del., March 30-31, 1976.

24. Ramberg, W., Osgood, W. B., "Description of Stress-Strain Curves by Three Parameters," NASA TN 902, 1943.

25. Herakovich, C. T., "On Thermal Edge Effects in Composite Laminates," Int. J. Mech. Sci., Vol. 18, pp. 129-134, 1976.

APPENDIX A

APPENDIX A

CONSTITUTIVE RELATIONS

The constitutive relationship for an orthotropic material in the principal material directions is

$$\{\sigma\}_1 = [C](\{\varepsilon\}_1 - \{\alpha\}_1 \Delta T - \{\beta\}_1 \Delta M)$$

where

$$[C] = \begin{bmatrix} C_{11} & C_{12} & C_{13} & 0 & 0 & 0 \\ & C_{22} & C_{23} & 0 & 0 & 0 \\ & & C_{33} & 0 & 0 & 0 \\ & & & C_{44} & 0 & 0 \\ \text{Symmetric} & & & & C_{55} & 0 \\ & & & & & C_{66} \end{bmatrix}$$

$$\{\sigma\}_1 = \begin{Bmatrix} \sigma_1 \\ \sigma_2 \\ \sigma_3 \\ \tau_{23} \\ \tau_{13} \\ \tau_{12} \end{Bmatrix} \qquad \{\varepsilon\}_1 = \begin{Bmatrix} \varepsilon_1 \\ \varepsilon_2 \\ \varepsilon_3 \\ \gamma_{23} \\ \gamma_{13} \\ \gamma_{12} \end{Bmatrix}$$

$$\{\alpha\}_1 = \begin{Bmatrix} \alpha_1 \\ \alpha_2 \\ \alpha_3 \\ 0 \\ 0 \\ 0 \end{Bmatrix} \qquad \{\beta\}_1 = \begin{Bmatrix} \beta_1 \\ \beta_2 \\ \beta_3 \\ 0 \\ 0 \\ 0 \end{Bmatrix}$$

For a θ rotation about the 3 (z) axis (Fig. 1), the constitutive relationship becomes

$$\{\sigma\} = [\bar{C}](\{\varepsilon\}-\{\alpha\}\Delta T-\{\beta\}\Delta M)$$

where

$$[\bar{C}] = \begin{bmatrix} \bar{C}_{11} & \bar{C}_{12} & \bar{C}_{13} & 0 & 0 & \bar{C}_{16} \\ & \bar{C}_{22} & \bar{C}_{23} & 0 & 0 & \bar{C}_{26} \\ & & \bar{C}_{33} & 0 & 0 & \bar{C}_{36} \\ & & & \bar{C}_{44} & \bar{C}_{45} & 0 \\ \text{Symmetric} & & & & \bar{C}_{55} & 0 \\ & & & & & \bar{C}_{66} \end{bmatrix}$$

$$\{\sigma\} = \begin{Bmatrix} \sigma_x \\ \sigma_y \\ \sigma_z \\ \tau_{yz} \\ \tau_{xz} \\ \tau_{xy} \end{Bmatrix} \qquad \{\varepsilon\} = \begin{Bmatrix} \varepsilon_x \\ \varepsilon_y \\ \varepsilon_z \\ \gamma_{yz} \\ \gamma_{xz} \\ \gamma_{xy} \end{Bmatrix}$$

$$\{\alpha\} = \begin{Bmatrix} \alpha_x \\ \alpha_y \\ \alpha_z \\ 0 \\ 0 \\ \alpha_{xy} \end{Bmatrix} \qquad \{\beta\} = \begin{Bmatrix} \beta_x \\ \beta_y \\ \beta_z \\ 0 \\ 0 \\ \beta_{xy} \end{Bmatrix}$$

and the various matrix and vector terms as functions of the principal material properties are given below ($m=\cos\theta$, $n=\sin\theta$).

$$\bar{C}_{11} = m^4C_{11}+2m^2n^2(C_{12}+2C_{66})+n^4C_{22}$$

$$\bar{C}_{12} = m^2n^2(C_{11}+C_{22}-4C_{66})+(m^4+n^4)C_{12}$$

$$\bar{C}_{13} = m^2C_{13}+n^2C_{23}$$

$$\bar{C}_{16} = -mn[m^2C_{11}-n^2C_{22}-(m^2-n^2)(C_{12}+2C_{66})]$$

$$\bar{C}_{22} = n^4C_{11}+2m^2n^2(C_{12}+2C_{66})+m^4C_{22}$$

$$\bar{C}_{23} = n^2C_{13}+m^2C_{23}$$

$$\bar{C}_{33} = C_{33}$$

$$\bar{C}_{36} = mn(C_{23}-C_{13})$$

$$\bar{C}_{44} = m^2C_{44}+n^2C_{55}$$

$$\bar{C}_{45} = mn(C_{44}-C_{55})$$

$$\bar{C}_{55} = n^2C_{44}+m^2C_{55}$$

$$\bar{C}_{66} = m^2n^2(C_{11}+C_{22}-2C_{12})+(m^2-n^2)^2C_{66}$$

$$\alpha_x = m^2\alpha_1+n^2\alpha_2$$

$$\alpha_y = n^2\alpha_1+m^2\alpha_2$$

$$\alpha_z = \alpha_3$$

$$\alpha_{xy} = -2mn(\alpha_1-\alpha_2)$$

$$\beta_x = m^2\beta_1+n^2\beta_2$$

$$\beta_y = n^2\beta_1+m^2\beta_2$$

$$\beta_z = \beta_3$$

$$\beta_{xy} = -2mn(\beta_1-\beta_2)$$

APPENDIX B

APPENDIX B

FINITE ELEMENT MESHES

The following are the various finite element meshes used in this study. Each models the quarter plane of symmetry (Fig. 1b). Thus, a two layer mesh models a four layer symmetric laminate and a four layer mesh models an eight layer symmetric laminate. Similarily, a one layer cutout means one layer removed on both top and bottom of the laminate (2 layers total removed).

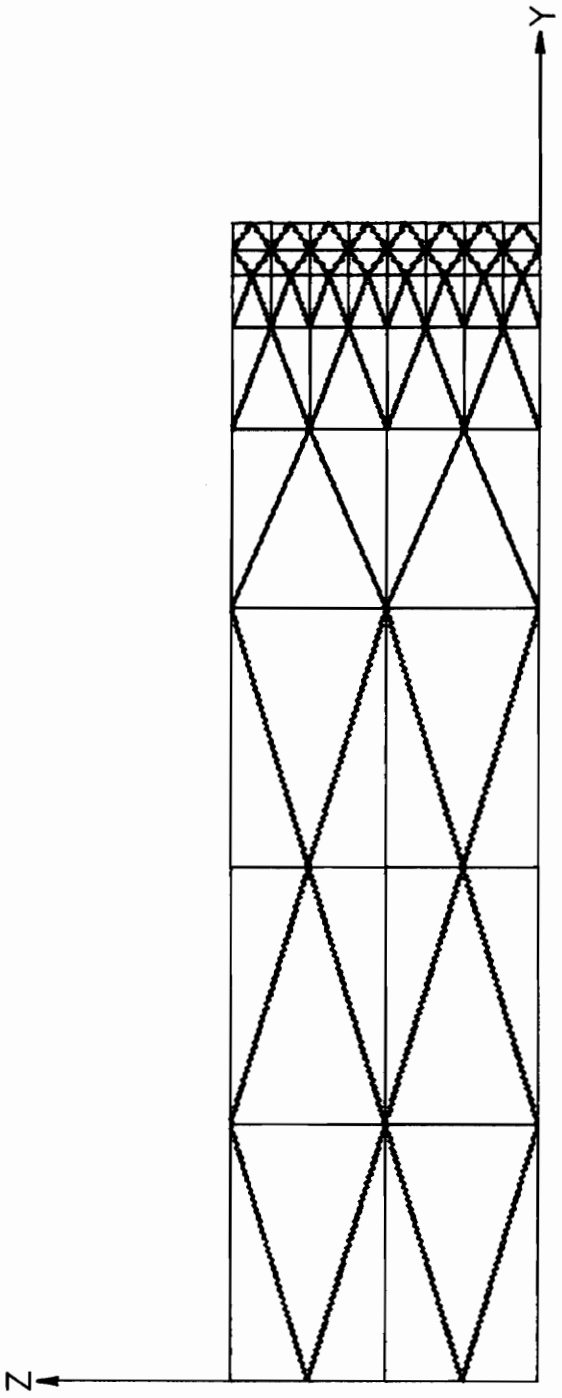

Figure B.1. Two Layer Finite Element Mesh for Quarter Cross-Section of Four Layer Symmetric Laminate.

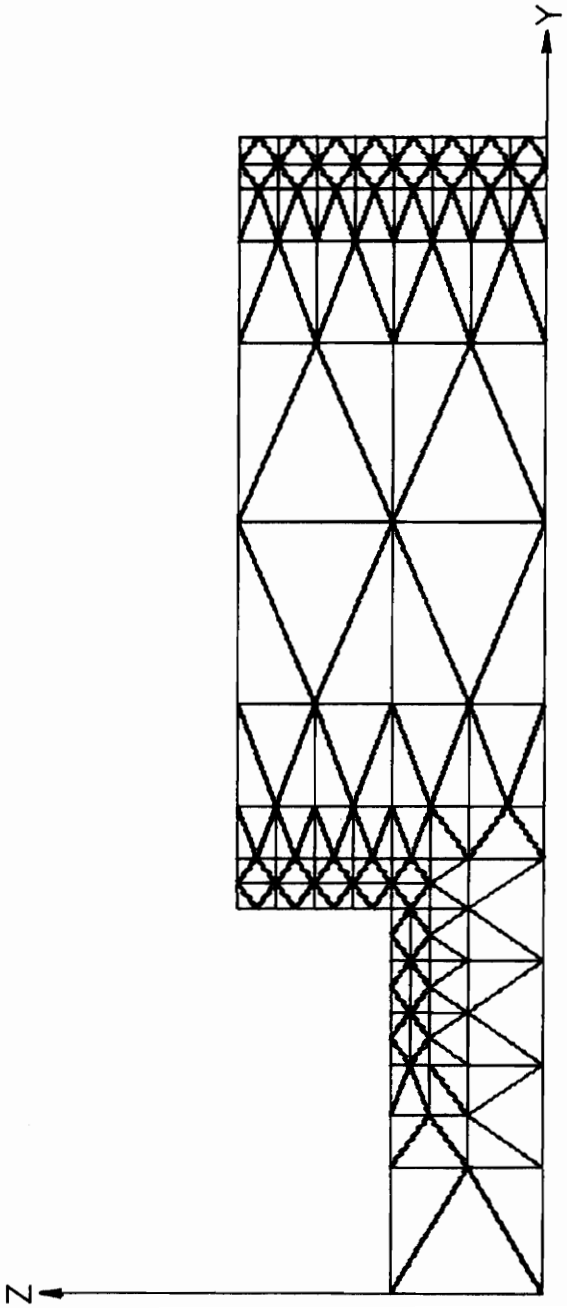

Figure B.2. Two Layer Finite Element Mesh for Quarter Cross-Section of Four Layer Symmetric Laminate with One Layer Cutout.

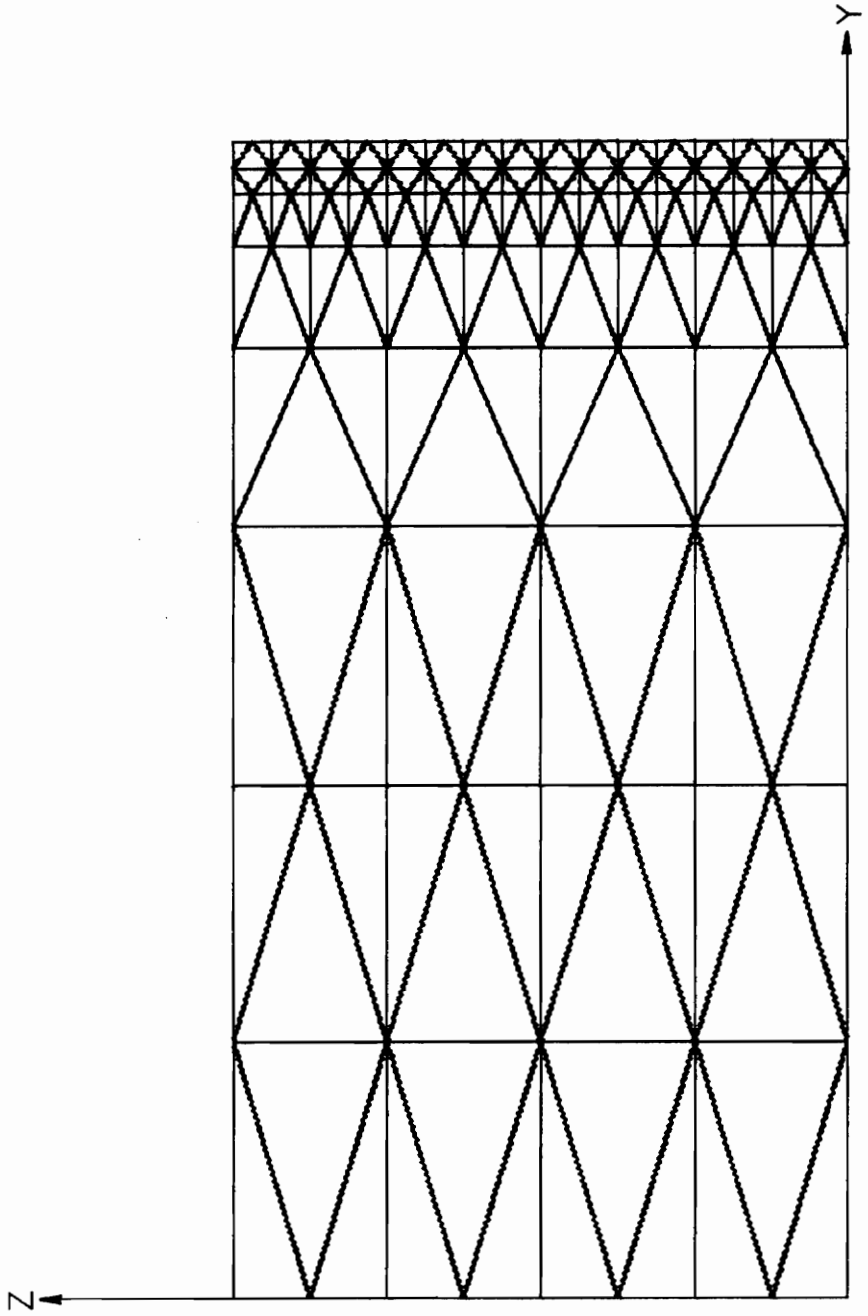

Figure B.3. Four Layer Finite Element Mesh for Quarter Cross-Section of Eight Layer Symmetric Laminate.

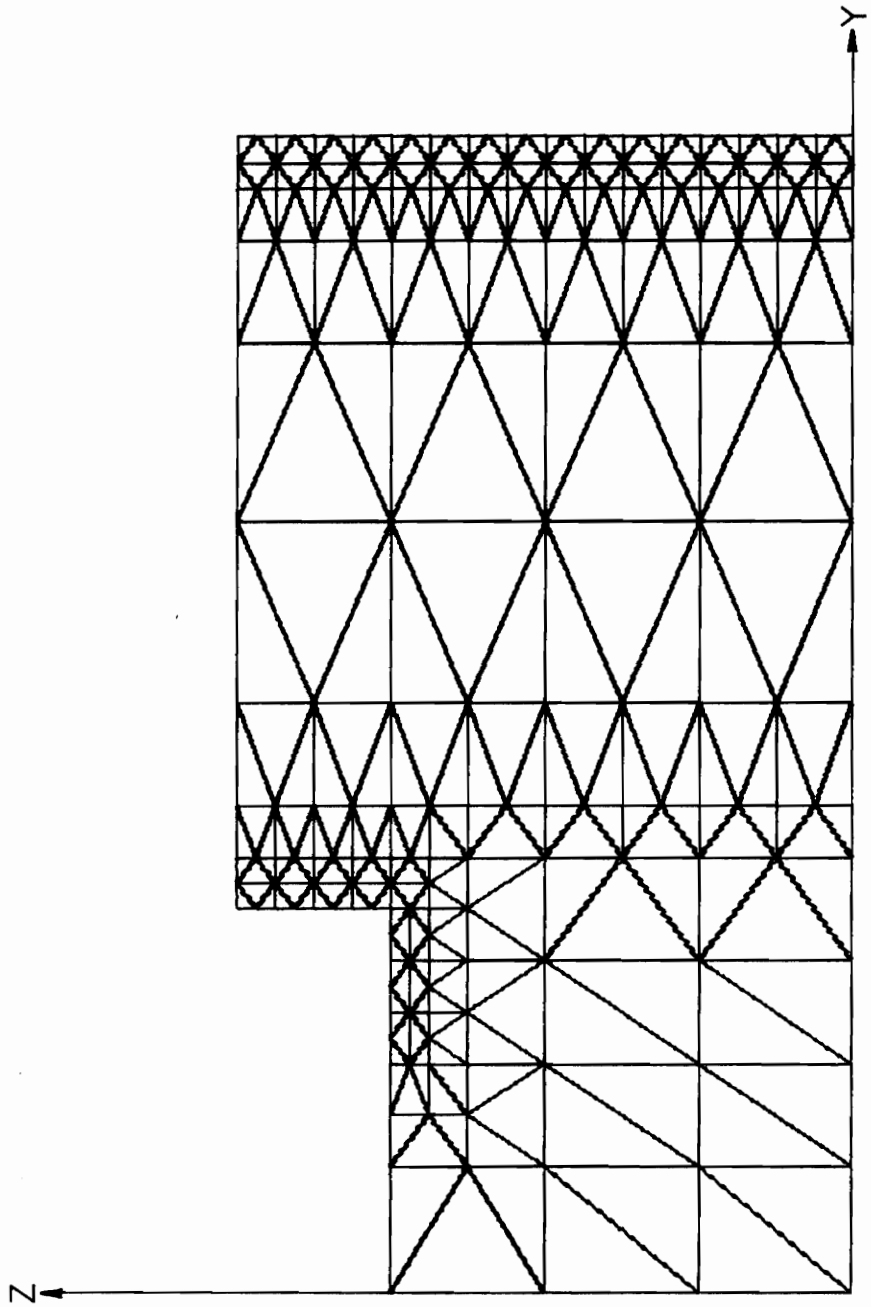

Figure B.4. Four Layer Finite Element Mesh for Quarter Cross-Section of Eight Layer Symmetric Laminate with One Layer Cutout.

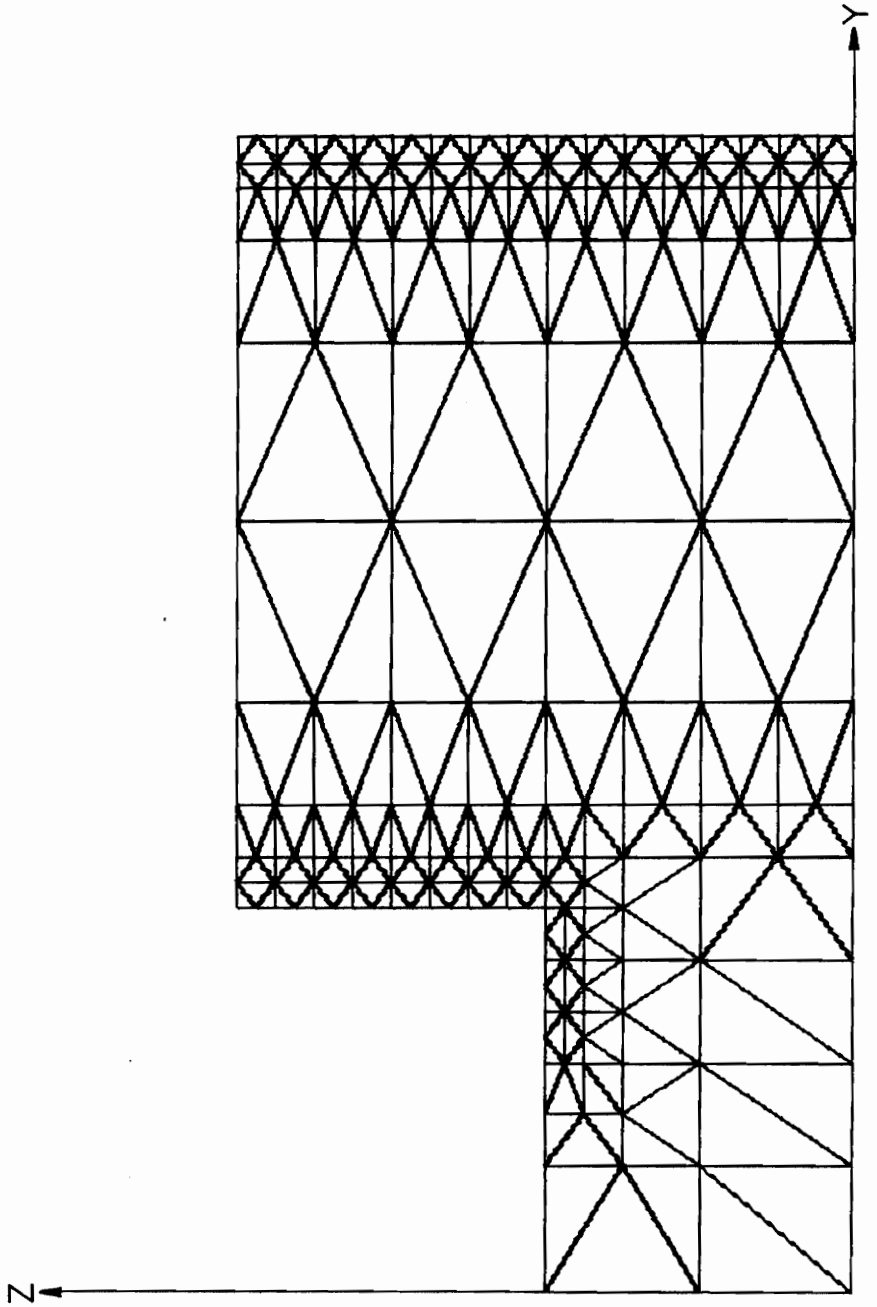

Figure B.5. Four Layer Finite Element Mesh for Quarter Cross-Section of Eight Layer Symmetric Laminate with Two Layer Cutout.

APPENDIX C

APPENDIX C

TSAI-WU FAILURE CRITERIA

The Tsai-Wu failure criteria has the tensorial form (for an orthotropic material in the principal material directions) of

$$\begin{aligned} &F_1\sigma_1+F_2\sigma_2+F_3\sigma_3+F_{11}\sigma_1^2+F_{22}\sigma_2^2 \\ &+F_{33}\sigma_3^2+F_{44}\tau_{23}^2+F_{55}\tau_{13}^2+F_{66}\tau_{12}^2 \\ &+2F_{12}\sigma_1\sigma_2+2F_{13}\sigma_1\sigma_3+2F_{23}\sigma_2\sigma_3 = 1 \end{aligned} \tag{C.1}$$

where the F_i and F_{ij} terms are as previously defined in Chapter 3. For a θ transformation about the z (3) axis (Fig. 1), the Tsai-Wu criteria takes the form

$$\begin{aligned} &F'_1\sigma_x+F'_2\sigma_y+F'_5\sigma_z+F'_6\sigma_{xy}+F'_{11}\sigma_x^2 \\ &+F'_{22}\sigma_y^2+F'_{33}\sigma_z^2+F'_{44}\tau_{yz}^2+F'_{55}\tau_{xz}^2 \\ &+F'_{66}\tau_{xy}^2+2F'_{16}\sigma_x\tau_{xy}+2F'_{26}\sigma_y\tau_{xy} \\ &+2F'_{36}\sigma_z\tau_{xy}+2F'_{45}\tau_{yz}\tau_{xz}+2F'_{12}\sigma_x\sigma_y \\ &+2F'_{13}\sigma_x\sigma_y+2F'_{23}\sigma_y\sigma_z = 1 \end{aligned} \tag{C.2}$$

where the F' terms, as functions of the unprimed F's and θ, are as follows ($m = \cos\theta$, $n = \sin\theta$)

$$F'_1 = m^2F_1+n^2F_2$$

$$F'_2 = n^2F_1+m^2F_2$$

$$F'_3 = F_3$$

$$F'_6 = -2mn(F_1-F_2)$$

$$F'_{11} = m^4F_{11}+m^2n^2(F_{66}+2F_{12})+n^4F_{22}$$

$$F'_{22} = n^4F_{11}+m^2n^2(F_{66}+2F_{12})+m^4F_{22}$$

$$F'_{33} = F_{33}$$

$$F'_{44} = m^2F_{44}+n^2F_{55}$$

$$F'_{55} = n^2F_{44}+m^2F_{55}$$

$$F'_{66} = 4m^2n^2(F_{11}+F_{22}-2F_{12})+(m^2-n^2)^2F_{66}$$

$$F'_{16} = mn[2m^2(F_{11}-F_{22})-(m^2-n^2)(2F_{12}-F_{66})]$$

$$F'_{26} = -mn[2n^2(F_{11}-F_{22})+(m^2-n^2)(2F_{12}-F_{66})]$$

$$F'_{36} = -2mn(F_{13}-F_{23})$$

$$F'_{45} = mn(F_{44}-F_{55})$$

$$F'_{12} = m^2n^2(F_{11}+F_{22}-F_{66})+(m^4+n^4)F_{12}$$

$$F'_{13} = m^2F_{13}+n^2F_{23}$$

$$F'_{23} = n^2F_{13}+m^2F_{23}$$

APPENDIX D

APPENDIX D

MATERIAL PROPERTIES

This appendix contains all the material values for Thornel 300 Graphite/Narmco 5208 used in this study. All data were presented in reference [22] except for the β values in Table D.2, which came from reference [23]. Fig. D.1 represents the stress-strain response for T300/5208. Table D.1 contains the Ramberg-Osgood coefficients and strength parameters used while Table D.2 contains the thermal/moisture properties of T300/5208.

In Table D.1, σ^* corresponds to the stress at which the Ramberg-Osgood coefficients n_2 and k_2 become applicable. The values of the Tsai-Wu interaction terms, F_{12}, F_{13} and F_{23}, are all equal to $-0.58 \times 10^{-10}/(PSI)^2$, the value given in reference [18]. No data was found showing the hygrothermal variation of the interaction terms.

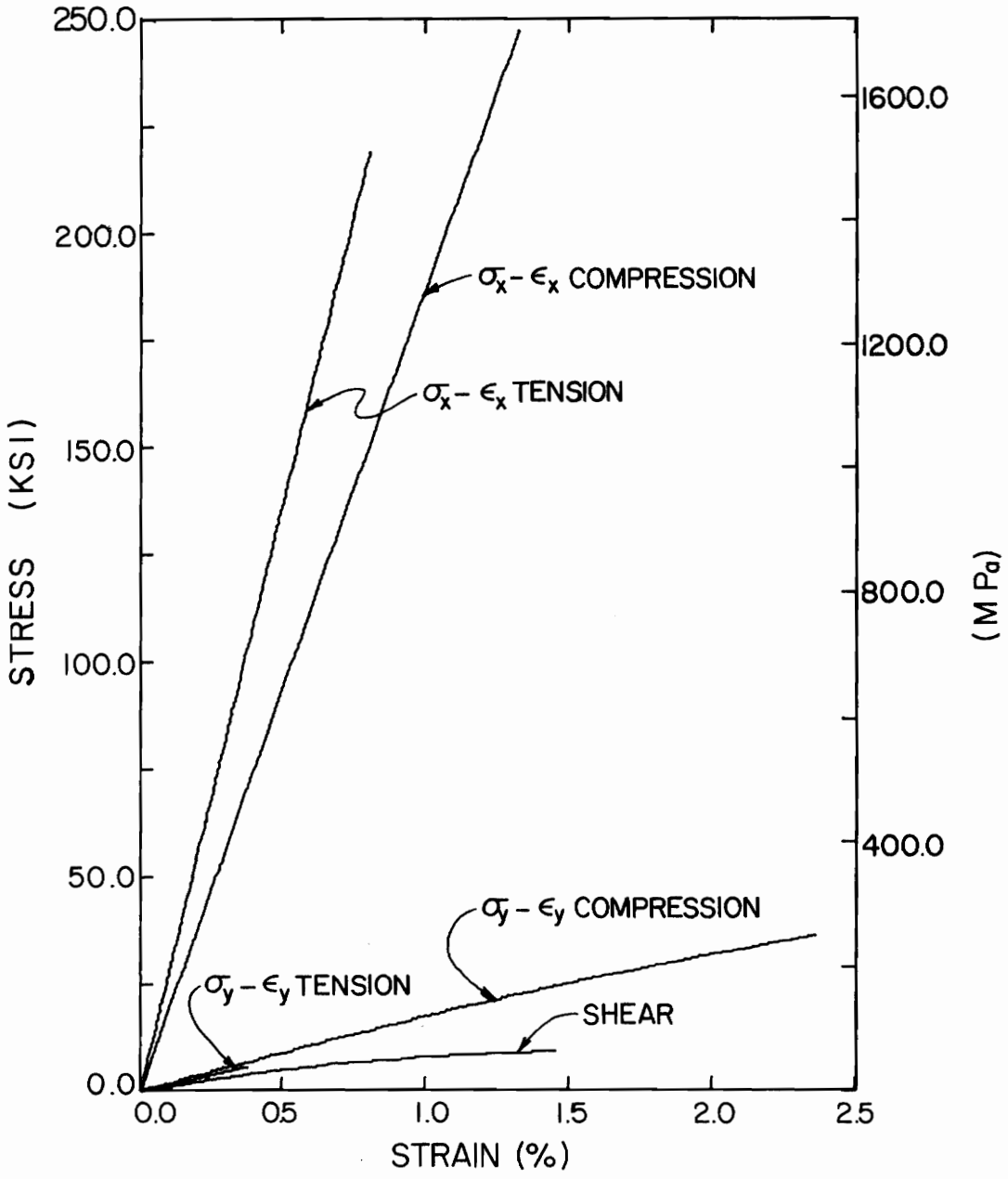

Figure D.1. Stress-Strain Curves for T300/5208 Graphite Epoxy.

TABLE D.1 Ramberg-Osgood Parameters for Graphite-Epoxy T300/5208

Curve	Elastic Modulus (MSI)	Elastic Limit (KSI)	n_1	$K_1(PSI^{-n_1})$	σ^* (KSI)	n_2	$K_2(PSI^{-n_2})$
E^t_{xx}	27.6	5.0	2.555	1.8074×10^{-18}	-	-	-
E^c_{xx}	18.9	6.0	2.357	3.0861×10^{-17}	-	-	-
E^t_{yy}	1.6	0.1	1.728	1.8405×10^{-11}	-	-	-
E^c_{yy}	1.8	1.5	3.487	3.9753×10^{-19}	-	-	-
E^t_{zz}	1.6	0.1	1.728	1.8405×10^{-11}	-	-	-
E^c_{zz}	1.8	1.5	3.487	3.9753×10^{-19}	-	-	-
G_{yz}	1.05	0.05	1.361	4.2901×10^{-10}	2.82	4.668	1.6842×10^{-21}
G_{xz}	1.05	0.05	1.361	4.2901×10^{-10}	2.82	4.668	1.6842×10^{-21}
G_{xy}	1.05	0.05	1.361	4.2901×10^{-10}	2.82	4.668	1.6842×10^{-21}

TABLE D.2 Hygrothermal Properties for Graphite-Epoxy T300/5208

Property	Room Temp. 0% Moisture -Elastic Modulus- (Msi)	Percent Retention of Room Temp., 0% Moisture Property								
		Temperature -70° F			Temperature -260° F			Temperature -350° F		
		Percent Weight Gain			Percent Weight Gain			Percent Weight Gain		
		0.00	0.83	1.13	0.00	0.83	1.13	0.00	0.83	1.13
E^t_{xx}	27.6	100.0	84.1	84.1	107.3	-	85.4	112.2	-	91.0
E^c_{xx}	18.9	100.0	91.1	80.8	97.8	84.7	-	96.4	-	-
E^t_{yy}	1.6	100.0	88.2	92.1	93.4	-	100.0	79.3	-	-
E^c_{yy}	1.8	100.0	-	-	-	-	-	-	-	-
E^t_{zz}	1.6	100.0	88.2	92.1	93.4	-	100.0	79.3	-	94.9
E^c_{zz}	1.8	100.0	-	-	-	-	-	-	-	-
G_{yz}	1.05	100.0	93.9	89.0	96.2	-	75.1	85.4	-	81.1
G_{xz}	1.05	100.0	93.9	89.0	96.2	-	75.1	85.4	-	81.1
G_{xy}	1.05	100.0	93.9	89.0	96.2	-	75.1	85.4	-	81.1

TABLE D.2 continued

Property	Room Temp. 0% Moisture -Strength- (ksi)	Percent Retention of Room Temp., 0% Moisture Property								
		Temperature -70° F			Temperature -260° F			Temperature -350° F		
		Percent Weight Gain			Percent Weight Gain			Percent Weight Gain		
		0.00	0.83	1.13	0.00	0.83	1.13	0.00	0.83	1.13
X_t	218.0	100.0	95.5	86.6	96.8	81.0	88.4	93.8	67.6	77.8
X_c	-218.0	100.0	94.3	96.4	92.1	90.7	96.0	88.5	-	-
Y_t	5.9	100.0	79.3	97.9	69.1	44.8	47.3	48.9	24.5	46.3
Y_c	-36.3	100.0	-	-	78.3	75.5	-	74.7	57.3	80.9
Z_t	5.9	100.0	79.3	97.9	69.1	44.8	47.3	48.7	24.5	46.3
Z_c	-36.3	100.0	-	-	78.3	75.5	-	74.7	57.3	80.9
S_{23}	9.8	100.0	132.0	132.0	76.1	81.2	90.6	64.6	75.2	87.2
S_{13}	9.8	100.0	132.0	132.0	76.1	81.2	90.6	64.6	75.2	87.2
S_{12}	9.8	100.0	132.0	132.0	76.1	81.2	90.6	64.6	75.2	87.2

TABLE D.2 continued

Property	Room Temp. 0% Moisture -ν-	Percent Retention of Room Temp., 0% Moisture Property								
		Temperature -70° F			Temperature -260° F			Temperature -350° F		
		Percent Weight Gain			Percent Weight Gain			Percent Weight Gain		
		0.00	0.83	1.13	0.00	0.83	1.13	0.00	0.83	1.13
ν_{yz}^{t}	0.38	100.0	-	89.5	81.6	-	-	68.4	-	-
ν_{yz}^{c}	0.38	100.0	-	-	78.9	-	-	81.6	-	-
ν_{xz}^{t}	0.38	100.0	-	89.5	81.6	-	-	68.4	-	-
ν_{xz}^{c}	0.38	100.0	-	-	78.9	-	-	81.6	-	-
ν_{xy}^{t}	0.38	100.0	-	89.5	81.6	-	-	68.4	-	-
ν_{xy}^{c}	0.38	100.0	-	-	78.9	-	-	81.6	-	-

TABLE D.2 continued

Property	Room Temp. 0% Moisture -Temperature Coefficient- (μin/in/°F)	Temperature Coefficient (μin/in/°F)								
		Temperature -70° F			Temperature -260° F			Temperature -350° F		
		Percent Weight Gain			Percent Weight Gain			Percent Weight Gain		
		0.00	0.83	1.13	0.00	0.83	1.13	0.00	0.83	1.13
α_x	0.01	0.01	-	-	0.14	-	-	0.40	-	-
α_y	11.0	11.0	-	-	17.8	-	-	21.0	-	-
α_z	11.0	11.0	-	-	17.8	-	-	21.0	-	-

TABLE D.2 continued

Property	Room Temp. 0% Moisture -Moisture Coefficient- (in/in/%Wt)	Moisture Coefficient (in/in/%Wt Gain)								
		Temperature -70° F			Temperature -260° F			Temperature -350° F		
		Percent Weight Gain			Percent Weight Gain			Percent Weight Gain		
		0.00	0.83	1.13	0.00	0.83	1.13	0.00	0.83	1.13
β_x	0.0	0.0	0.0	0.0	-	-	-	-	-	-
β_y	0.0	0.0	0.0049	0.0061	-	-	-	-	-	-
β_z	0.0	0.0	0.0049	0.0061	-	-	-	-	-	-

APPENDIX E

APPENDIX E

INPUT MODIFICATIONS FOR NONCOM2

The modifications to NONCOM1 require two changes to the users guide given in reference [3]. One is the input of the Tsai-Wu interaction terms F_{23}, F_{13} and F_{12} along with the uniaxial strengths. The other change is the simultaneous input of the thermal and hygroscopic properties rather than separately as before.

E.1 The following replaces card 27 of reference [3].

Card 27 (6E12.6)

Column		Contents
1-12	SL23(K)	= Ultimate stress for τ_{23} - γ_{23}
13-24	SL13(K)	= Ultimate stress for τ_{13} - γ_{13}
25-36	SL12(K)	= Ultimate stress for τ_{12} - γ_{12}
37-48	XF23(K)	= F_{23} interaction term
49-60	XF13(K)	= F_{13} interaction term
61-72	XF12(K)	= F_{12} interaction term

E.2 The following cards replace cards 29 to 50 of reference [3] and, when hygrothermal analysis is required, are inserted between cards 28 and 51 as given in reference [3].

The following cards are repeated NDIFM time (for each different material).

K=1, NDIFM

Card 29 (16I5)

Column		Contents
1-5	NTE11(K,1)	= Number of linear segmented temperature points for E_{11} tensile modulus percent retention curve
6-10	NME11(K,I,1)	= Number of linear segmented moisture points for E_{11} tensile modulus percent retention curve at Ith temperature
etc.	I=1,NTE11(K,1)	

The following two cards are repeated NTE11(K,1) time (I=1, NTE11(k,1)).

Card 30 (1E10.3)

Column		Contents
1-10	TMPE11(K,I,1)	= Temperature at Ith temperature

Card 31 (8E10.3)

Column		Contents
1-10	PME11(K,I,J,1)	= Moisture content at Ith temperature
11-20	PRDE11(K,I,J,1)	= Percent retention of E_{11} tensile modulus at Ith temperature and Jth moisture content
etc.	repeated J=1,NME11(K,I,1)	

Card 32 (16I5)

Column		Contents
1-5	NTE11(K,2) =	
6-10	NME11(KI,2) =	

Card 33 (1E10.3)

Column		Contents
1-10	TMPE11(K,I,2) =	Same as cards 29 to 31 but for E_{11} compressive modulus

Card 34 (8E10.3)

Column		
1-10	PME11(K,I,J,2) =	
11-20	PRDE11(K,I,J,2) =	

Card 35 (16I5)

Column		Contents
1-5	NTE22(K,1) =	
6-10	NME22(K,I,1) =	

Card 36 (1E10.3)

Column		Contents
1-10	TMPE22(K,I,1) =	Same as cards 29 to 31 but for E_{22} tensile modulus

Card 37

Column		
1-10	PME22(K,I,J,1) =	
11-20	PRDE22(K,I,J,1) =	

Card 38 (16I5)

Column		Contents
1-5	NTE22(K,2) =	
6-10	NME22(K,I,2) =	

Card 39 (1E10.3)

Column		
1-10	TMPE22(K,I,2) =	Same as cards 29 to 31 but for E_{22} compressive modulus

Card 40 (8E10.3)

Column		
1-10	PME22(K,I,J,2) =	
11-20	PRDE22(K,I,J,2) =	

Card 41 (16I5)

Column		Contents
1-5	NTE33(K,1) =	
6-10	NME33(K,I,1) =	

Card 42 (1E10.3)

Column		
1-10	TMPE33(K,I,1) =	Same as cards 29 to 31 but for E_{33} tensile modulus

Card 43 (8E10.3)

Column		
1-10	PME33(K.I,J,1) =	
11-20	PRDE33(K,I,J,1) =	

Card 44 (16I5)

Column			Contents
1-5	NTE33(K,2)	=	
6-10	NME33(K,I,2)	=	

Card 45 (1E10.3)

Column			
1-10	TMPE33(K,I,2)	=	Same as cards 29 to 31 but for E_{33} compressive modulus

Card 46 (8E10.3)

Column			
1-10	PME33(K,I,J,2)	=	
11-20	PRDE33(K,I,J,2)	=	

Card 47 (16I5)

Column			Contents
1-5	NTG23(K)	=	
6-10	NMG23(K,I)	=	

Card 48 (1E10.3)

Column			
1-10	TMPG23(K,I)	=	Same as cards 29 to 31 but for G_{23} shear modulus

Card 49 (8E10.3)

Column			
1-10	PMG23(K,I,J)	=	
11-20	PRDG23(K,I,J)	=	

Card 50 (16I5)

Column			Contents
1-5	NTG13(K)	=	
6-10	NMG12(K,I)	=	

Card 51 (1E10.3)

Column			
1-10	TMPG13(K,I)	=	Same as cards 29 to 31 but for G_{13} shear modulus

Card 52 (8E10.3)

Column			
1-10	PMG13(K,I,J)	=	
11-20	PRDG13(K,I,J)	=	

Card 53 (16I5)

Column			Contents
1-5	NTG12(K)	=	
6-10	NMG12(K,I)	=	

Card 54 (1E10.3)

Column			
1-10	TMPG12(K,I)	=	Same as cards 29 to 31 but for G_{12} shear modulus

Card 55 (8E10.3)

Column			
1-10	PMG12(K,I,J)	=	
11-20	PRDG12(K,I,J)	=	

Card 56 (16I5)

Column			Contents
1-5	NTU23(K,1)	=	
6-10	NMU23(K,I,1)	=	

Card 57 (1E10.3)

Column			
1-10		=	Same as cards 29 to 31 but for ν_{23} tensile Poisson's Ratio

Card 58 (8E10.3)

Column			
1-10	PMU23(K,I,J,1)	=	
11-20	PRDU23(K,I,J,1)	=	

Card 59 (16I5)

Column			Contents
1-5	NTU23(K,2)	=	
6-10	NMU23(K,I,2)	=	

Card 60 (1E10.3)

Column			
1-10	TMPU23(K,I,2)	=	Same as cards 29 to 31 but for ν_{23} compressive Poisson's Ratio

Card 61 (8E10.3)

Column			
1-10	PMR23(K,I,J,2)	=	
11-20	PRDU23(K,I,J,2)	=	

Card 62 (16I5)

Column			Contents
1-5	NTU13(K,1)	=	
6-10	NMU13(K,I,1)	=	

Card 63 (1E10.3)

Column			
1-10	TMPU13(K,I,1)	=	Same as cards 29 to 31 but for ν_{13} tensile Poisson's Ratio

Card 64 (8E10.3)

Column			Contents
1-10	PMU13(K,I,J,1)	=	
11-20	PRDU13(K,I,J,1)	=	

Card 65 (16I5)

Column			Contents
1-5	NTU13(K,2)	=	
6-10	NMU13(K,I,2)	=	

Card 66 (1E10.3)

Column			
1-10	TMPU13(K,I,2)	=	Same as cards 29 to 31 but for ν_{13} compressive Poisson's Ratio

Card 67 (8E10.3)

Column			
1-10	PMU13(K,I,J,2)	=	
11-20	PRDU13(K,I,J,2)	=	

Card 68 (16I5)

Column		Contents
1-5	NTU12(K,1) =	
6-10	NMU12(K,I,1) =	

Card 69 (1E10.3)

Column		
1-10	TMPU12(K,I,1) =	Same as cards 29 to 31 but for ν_{12} tensile Poisson's Ratio

Card 70 (8E10.3)

Column		Contents
1-10	PMU12(K,I,J,1) =	
11-20	PRDU12(K,I,J.1) =	

Card 71 (16I5)

Column		Contents
1-5	NTU12(K,2) =	
6-10	NMU12(K,I,2) =	

Card 72 (1E10.3)

Column		
1-10	TMPU12(K,I,2) =	Same as cards 29 to 31 but for ν_{12} compressive Poisson's Ratio

Card 73 (8E10.3)

Column		
1-10	PMU12(K,I,J,2) =	
11-20	PRDU12(K,I,J,2) =	

Card 74 (16I5)

Column			Contents
1-5	NTS11(K,1)	=	
6-10	NMS11(K,I,1)	=	

Card 75 (1E10.3)

Column			
1-10	TMPS11(K,I,1)	=	Same as cards 29 to 31 but for X_t tensile strength

Card 76 (8E10.3)

Column			
1-10	PMS11(K,I,J,1)	=	
11-20	PRDS11(K,I,J,1)	=	

Card 77 (16I5)

Column			Contents
1-5	NTS11(K,2)	=	
6-10	NMS11(K,I,2)	=	

Card 78 (1E10.3)

Column			
1-10	TMPS11(K,I,2)	=	Same as cards 29 to 31 but for X_c compressive strength

Card 79 (8E10.3)

Column			
1-10	PMS11(K,I,J,2)	=	
11-20	PRDS11(K,I,J,2)	=	

Card 80 (16I5)

Column			Contents
1-5	NTS22(K,1)	=	
6-10	NMS22(K,I,1)	=	

Card 81 (1E10.3)

Column			
1-10	TMPS22(K,I,1)	=	Same as cards 29 to 31 but for Y_t tensile strength

Card 82 (8E10.3)

Column			
1-10	PMS22(K,I,J,1)	=	
11-20	PRDS22(K,I,J,1)	=	

Card 83 (16I5)

Column			Contents
1-5	NTS22(K,2)	=	
6-10	NMS22(K,I,2)	=	

Card 84 (1E10.3)

Column			
1-10	TMPS22(K,I,2)	=	Same as cards 29 to 31 but for Y_c compressive strength

Card 85 (8E10.3)

Column			
1-10	PMS22(K,I,J,2)	=	
11-20	PRDS22(K,I,J,2)	=	

Card 86 (16I5)

Column			Contents
1-5	NTS33(K,1)	=	
6-10	NMS33(K,I,1)	=	

Card 87 (1E10.3)

Column			
1-10	TMPS33(K,I,1)	=	Same as cards 29 to 31 but for Z_t tensile strength

Card 88 (8E10.3)

1-10	PMS33(K,I,J,1)	=	
11-20	PRDS33(K,I,J,1)	=	

Card 89 (16I5)

Column			Contents
1-5	NTS33(K,2)	=	
6-10	NMS33(K,I,2)	=	

Card 90 (1E10.3)

Column			
1-10	TMPS33(K,I,2)	=	Same as cards 29 to 31 but for Z_c compressive strength

Card 91 (8E10.3)

1-10	PMS33(K,I,J,2)	=	
11-20	PRDS33(K,I,J,2)	=	

Card 92 (16I5)

Column			Contents
1-5	NTS23(K)	=	
6-10	NMS23(K,I)	=	

Card 93 (1E10.3)

Column			
1-10	TMPS23(K,I)	=	Same as cards 29 to 31 but for S_{23} shear strength

Card 94 (8E10.3)

Column			
1-10	PMS23(K,I,J)	=	
11-20	PRDS23(K,I,J)	=	

Card 95 (16I5)

Column			Contents
1-5	NTS13(K)	=	
6-10	NMS13(K,I)	=	

Card 96 1E10.3)

Column			
1-10	TMPS13(K,I)	=	Same as cards 29 to 31 but for S_{13} shear strength

Card 97 (8E10.3)

Column			
1-10	PMS13(K,I,J)	=	
11-20	PRDS13(K,I,J)	=	

edges of the other layers is shown to lead to total failure.

The material system studied is a graphite-epoxy, Thornel 300/ Narmco 5208, with nonlinear material behavior represented by Ramberg-Osgood approximations.